ulm university universität ulm

Institute of Electrochemistry

Overcoming the Obstacles in the Electrodeposition of Chromium and Iridium from Aqueous Solutions

Dissertation by
Yasser Samir Abdelmoaty Mostafa Sheasha
2019

Overcoming the Obstacles in the Electrodeposition of Chromium and Iridium from Aqueous Solutions

Dissertation

to obtain the academic degree
Doctor rerum naturalium (Dr. rer. nat.)

Submitted to the Faculty of Natural Sciences
of Ulm University

by

Yasser Samir Abdelmoaty Mostafa Sheasha
from GIZA, EGYPT

2019

The experimental part of this work has been carried out in the period extending between October 2014 and November 2018 in the Institute of Electrochemistry of the University of Ulm, under the supervision of Prof. Dr. Timo Jacob.

Defense Date: 29.04.2019

Dean of the Faculty of Natural Sciences: Prof. Dr. Peter Dürre

1. Reviewer: Prof. Dr. Timo Jacob
2. Reviewer: Prof. Dr. Carsten Streb
3. Reviewer: Prof. Dr. Herbert Over

For my parents

“And of knowledge, you (mankind) have been given only a little.”
— Qura’an (17:85)

Declaration of Authorship

I hereby declare that I have prepared the present dissertation independently and without unauthorized external help. I have not used any sources or resources other than those indicated, and any textually or literally taken from published or unpublished texts, and all statements based on oral information, have been identified as such. Likewise, all services provided by other persons are marked as such.

Ulm,

Table of Contents

1 Introduction **1**

2 Theoretical Background **5**

2.1 Electrochemical Deposition of Metals **5**

2.1.1 Growth modes 7

2.1.2 Glassy Carbon 8

2.1.3 Side reactions 9

2.2 Coordination Chemistry **10**

2.2.1 Overview 10

2.2.2 Octahedral Complexes 12

2.3 Chromium **13**

2.3.1 Overview 13

2.3.2 Complex chemistry of Trivalent Chromium 14

2.3.3 Electrodeposition of Chromium 16

2.3.4 Trivalent Chromium Bath Additives 18

2.4 Iridium **19**

2.4.1 Overview 19

2.4.2 Electrochemical Deposition of Iridium 20

2.4.3 Iridium Electrocatalysis 21

3 Experimental Methods **25**

3.1 Electrochemical Techniques **25**

3.1.1 Cyclic Voltammetry 25

3.1.2 Pulsing Methods 26

3.1.3 Galvanostatic Deposition 27

3.2 Ultraviolet-Visible Spectroscopy 27

3.3 Surface Characterization Techniques 28

3.3.1 Scanning Electron Microscopy (SEM) and Energy Dispersive X-ray Spectroscopy (EDX) 28

3.3.2 X-Ray Fluorescence (XRF) and Spectral Photometry 29

3.4 Preparation Techniques 31

3.4.1 Glassy Carbon 31

3.4.2 Brass sheets 32

3.4.3 Glassware 32

3.4.4 New Chromium (III) Solution 33

3.5 Chemicals and Materials 33

4 Results and Discussion 37

4.1 Electrochemical deposition of Iridium on GC Electrodes 37

4.1.1 The influence of the nucleation potential E_n 37

4.1.2 The influence of SWP duration on size 40

4.1.3 Probing the surface with CO adlayer oxidation 41

4.2 Electrochemical Behavior of Chromium and Chromium Solutions 44

4.2.1 Chromium Metal in 0.1 M H_2SO_4 44

4.2.2 Potentiodynamic deposition on GC 46

4.2.3 Mechanistic Insights 50

4.3 Development of a new electrolyte 51

4.3.1 Electrochemical measurements with aged solutions 52

4.3.2 Thermal acceleration and up-scaling 53

4.3.3 Designing the new solution 55

4.4 Electrochemical deposition from the monomeric complex 62

4.4.1 Electrodeposition on GC 62

4.4.2 Electrodeposition on Brass 64

4.4.3 Thickness and optical appearance 67

4.4.4 Mechanistic Insights 70

4.5 Use of other Complexing Agents 72

4.5.1 Formic Acid 72

4.5.2 Oxalic Acid 73

5 Conclusions and Outlook 77

5.1 Conclusions of the Iridium Study 77

5.2 Conclusions of the Chromium Study 78

5.3 Thesis Outlook 81

Bibliography 83

List of Figures 88

List of Tables 93

Nomenclature 94

Acknowledgements 95

Curriculum Vitae 96

1 Introduction

In 1772, G.B. Beccaria was the first to successfully deposit a metal from its salt, by using the spark produced upon discharging a Leyden bottle to decompose the metal salt. Following this discovery, Luigi Galvani discovered the physiological effects of electricity on frog legs when connected to two dissimilar metals in 1792, and shortly after, in 1796 his student, Volta discovered the pile, which could produce electricity from two dissimilar metals separated by a medium soaked in electrolyte. Then in 1805, Luigi Valentino Brugnatelli, who is believed to be the inventor of modern electrochemistry, used Volta's voltaic pile to produce enough electricity to successfully plate a silver coin with gold, serving to be the first significant electroplating experiment[1].

Nowadays, the electrochemical deposition of metals is utilized for a multitude of applications. These range from the fabrication of nanoparticles to film plating for surface modifications, either decorative or functional. By considering both ends of the spectrum, electrodeposition can be viewed as a versatile tool for materials engineering. Nonetheless, for such an old technique that has been extensively studied, the potential areas for development often come in question, especially in a time when the chemical industry is focused on environmental sustainability, either in terms of industrial waste, or in providing green energy solutions, in particular batteries and fuel cells. Hence, using classical techniques, like electrodeposition, for materials and process optimization for environmental sustainability promotes further research and development into the well-established field of electrochemical metal deposition.

In the case of the fuel cell industry, for example, one of the major challenges is building an appropriate grid scale energy storage solution. This is in short the electrocatalytic splitting of water into hydrogen and oxygen in polymer electrolyte membrane electrolyzer set ups[2]. The splitting of water can be classified as two separate reactions; the hydrogen evolution reaction (HER) at the cathode, and the oxygen evolution reaction (OER) at the anode. For both of these reactions a suitable catalyst is required, and so far the most promising catalysts are noble metals[2–4]. However, the use of noble metal catalysts presents the economic challenge of their very high cost[5].

Nanomaterials, particularly as catalysts, carry the advantage of large specific surface areas, thus increasing catalytic activity[6]. This in turn allows for a reduction in the noble metal loading of electrocatalysts, and thus is a promising way to decrease the costs for these technologies. Moreover, in recent years, this has evolved into the fabrication of nanocrystals with well-defined shapes and high index facets to further improve the catalytic efficiency, as well as the faceting of single crystal surfaces. Studies have been reported on the faceting of iridium (210) single crystals using thermal and electrochemical methods[7–10]. Work with deposition of preferentially oriented nanocrystals has been successfully implemented with gold, platinum, and palladium[11–13]. This is made possible by employing new electrodeposition techniques, such as Square Wave Potentials (SWP), where electric potential pulses are used, instead of the classical direct current (Galvanic) technique.

In the case of platinum, which exhibits the highest electrocatalytic activity for the HER[3], single crystal tetrahexahedral (THH) nanocrystals could be deposited onto glassy carbon (GC) substrates. Such surfaces contain a very high density of atomic steps and dangling bonds, which increase activity greatly. Not only does electrocatalytic activity increase by up to 400% for similar platinum surfaces, but these surfaces are also thermally stable up until 800ºC, making them very attractive for industrial applications[12].

On the other hand, applications for functional surface modifications, like hardness, wear resistance, corrosion protection, electrical and thermal conductivity, as well as decorative applications require the deposition of metal films on the surface. This allows for cost reduction by giving low cost materials the required surface characteristics[14,15].

Electrochemical chromium deposition is one of the most commonly used electrodeposition processes to achieve these goals[16]. To date, the majority of the electrodeposited chromium comes mainly from galvanic baths containing hexavalent chromium[17]. However, the use of hexavalent chromium poses a huge threat to people and to the environment, due to its toxic and carcinogenic nature. The greatest health threat arises from chromic acid mist, which is produced during galvanic plating with Cr(VI)[18]. Moreover, chromium plating industries are the major source of chromium contamination in ground water, which is insoluble and harmful to the environment[19].

As a result, the commercial use of Cr(VI) has already been banned in many countries[20,21]. In addition, according to the European legislation for chemicals “REACh” (Registration, Evaluation, Authorization and Restriction of Chemicals), the use of hexavalent chromium will be banned as of 2027. The previous sunset date for Cr(VI) was in 2017, however this was extended for 10 more years, mainly because no promising alternatives are available. Apart from legal regulations though, the overall rising environmental and health awareness promotes the search for a less dangerous alternative[17].

The use of aqueous Cr(III) baths for chromium deposition is a promising approach with much less risk. However, the large-scale implementation still involves some challenges[22]. Organic complex ligands have to be added to the solution to make the stable and almost inert $[Cr(H_2O)_6]^{3+}$ hexaquo-complex accessible for reduction. However, this complicates the already extremely complex and not yet fully understood deposition mechanism[23].

In this work, two independent systems were studied; the electrodeposition and electrochemical activity of well defined iridium nanospheres, and the electrodeposition of chromium from Cr(III) solutions. Not only do both systems require more research, especially in the initial stages, but also both systems have applications in environmental sustainability.

In the case of iridium, iridium nanoparticles have shown superior behavior as electrocatalysts for the OER[2]. However, the electrochemical deposition of iridium comes with the main challenge of hydrogen evolution that occurs during deposition, blocking the surface. Hence, the reported structures of iridium deposits in literature are mainly agglomerates and irregular structures[24]. Therefore, in order to be able to electrochemically deposit shape and size controlled nanoparticles for electrocatalysis, a SWP technique, coupled with a nucleation pulse to control the initial growth of the particles was developed. The results show that by varying different parameters, particle size and coverage, as well as surface morphology of the particle can be varied, and their effects on the electrocatalytic activity towards carbon monoxide adlayer oxidation presented.

As for chromium deposition, potentiodynamic deposition measurements on GC electrodes were designed to investigate the similarities and differences in the initial stages of growth between simple dilute Cr(III) and Cr(VI) electrolytes. Based on these measurements a mechanism for deposition was proposed and the key aspects in hindering deposition from trivalent chromium identified. Later, a new electrolyte was developed based on long time monitoring of electrolytes as well as UV-VIS spectra, which showed the formation of a monomeric aquo-complex as result of a slow ligand exchange reaction at low pH's. This was then complexed with malic acid to improve the complex's stability. As a result, a new accelerated preparation process for concentrated electrolytes was created, and tested on different substrates. Finally, initial investigations were conducted on different organic complexing agents, and their effects on the deposited chromium films.

2 Theoretical Background

2.1 Electrochemical Deposition of Metals

One of the most important applications of electrochemistry is electrochemical deposition, in order to change the chemical and physical properties of materials[14]. This ranges from the deposition of monodispersed nanoparticles, in order to increase surface area for applications like electrocatalysis, to millimeter thick layers to serve a multitude of applications like corrosion resistance, electrical conductivity, decorative purposes and enhancement of mechanical properties. Thus, understanding the mechanisms behind the electrodeposition of metals is of key importance, in order to obtain the desired output. These mechanisms are greatly influenced by many factors, such as solution medium, substrate material, side reactions and growth mode.

In general, electrodeposition occurs via the following pathway:

$$M^{z+} + ze^- \rightleftharpoons M_{(s)}$$

where M is any metal with a valency z[25]. The metal cations in solution are reduced to solid metal at the cathode, which is the substrate. In the above equation, the state symbol of the metal ion has been left out, because in principle, there are three main media from which metals could be deposited; aqueous solutions, organic solvents or ionic liquids.

The most widely employed medium is aqueous solution, due to its ease of handling, and low cost. However, aqueous solutions offer a considerably narrow potential window. The hydrogen evolution reaction (HER) sets the lower limit of this window. While most noble metals can be deposited from aqueous electrolytes, other metals, like lithium and aluminium, which are of great technological importance, cannot, since the potentials required for their deposition are outside of the potential window offered by aqueous solutions. For such metals, organic solvents and/or ionic liquids (room temperature molten salts) can be of great help since they offer wider potential windows[26].

Electrodeposition from aqueous solution follows a nucleation and growth scheme[27]. The reaction direction is governed by the Nernst equation:

$$E = E^0 + \frac{0.0592}{z} \log [M^{z+}]$$

where E^0 is the standard electrode potential of the M/M^{z+} electrode, and z is the number of electrons involved in the reaction[15]. Hence, in order to have a stable nucleus to support further growth, the electrode potential due to applied current E_I should be higher than the equilibrium potential E, to drive the reaction forward[27]. The difference between both potentials is defined as the overpotential η[28], such that:

$$\eta = E_I - E.$$

The stability of the nucleus also depends on the Gibb's free energy (Δg) for nucleation, which is the sum of both bulk free energy and surface free energy[26]:

$$\Delta_{g(nucl)} = \Delta_{g(bulk)} + \Delta_{g(surface)}$$

Figure 2.1 highlights the relationship between Δg and nucleus size for a stable nucleus.

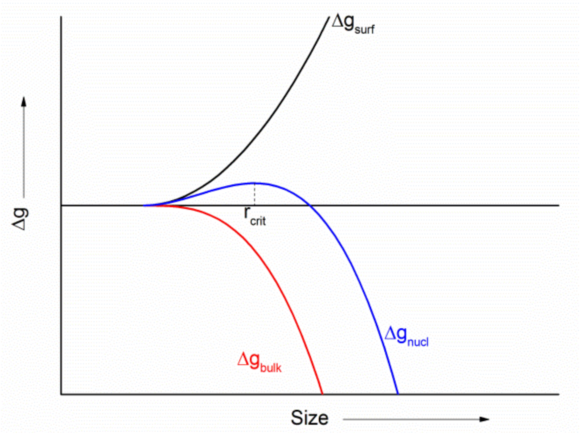

Figure 2.1 Gibbs free energy of nucleation as a function of particle size

Therefore, for it to be stable, a nucleus should have a minimum radius of $r > r_{crit}$. Once a stable nucleus is obtained, subsequent growth could follow a two- or three-dimensional growth profile.

In order for the formed metal nuclei to grow, metal cations have to be readily present in solution. These cations then need to be adsorbed onto the nucleus surface and reduced into atoms. This achieved by applying a negative electrode potential, that allows the adsorption of the metal ions in solution onto the already formed nucleus, where it is then reduced. Thus, the potential acts as the driving force for such growth, and by varying the potential, the rate of growth can also be varied.

2.1.1 Growth modes

There are two main modes of growth; two-dimensional and three-dimensional growth. Three-dimensional growth occurs on foreign substrates, where the binding energy between an adsorbed metal ion and the substrate is lower than that between the metal ion and the native metal. In this case, larger overpotentials are required, in order to facilitate a 3D island growth mode, regardless of the metal-substrate misfit. This is referred to as overpotential deposition (OPD). These clusters could then grow in size until they fuse together into a homogeneous layer. This is known to as the "Volmer-Weber" growth mode[27].

On the other hand, two-dimensional growth takes place if the binding energy between the adsorbed metal ions and the substrate is larger than that with the native metal. In such case, the surface is initially modified by a few monolayers in the underpotential deposition (UPD) region. Growth due to OPD could follow either a "Frank-van der Merwe" or a "Stranski-Krastanov" growth mode, depending on the lattice misfit between both materials. The former is an epitaxial layer-by-layer growth mode that occurs if the misfits are negligible. Upon further growth, deposition behaves as it would on a native metal surface.

For larger lattice misfits, the initial layers are internally strained, with a crystal structure different from that of the substrate and that of the bulk metal. Further deposition continues as unstrained 3D islands on top of the strained layers, which is energetically favored, following the "Stranski-Krastanov" growth mode. Therefore, the overall deposit is always influenced by the initial stages[27], and hence it is crucial to investigate these initial mechanisms, to be able to control the output. Figure 2.2[29] summarizes nucleation and growth modes.

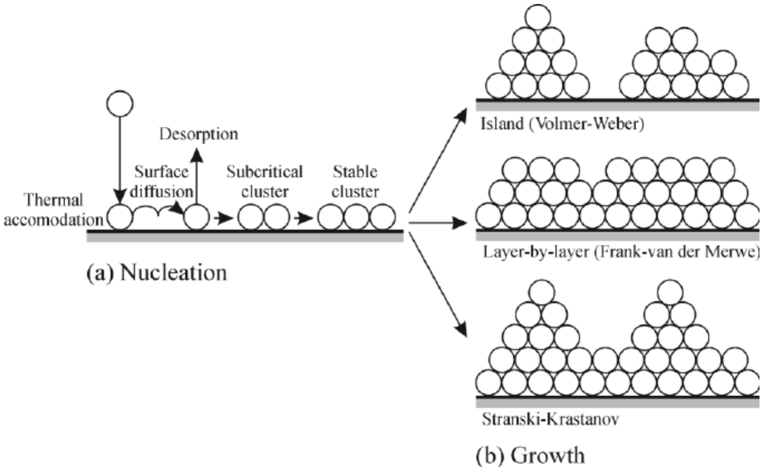
Desorption
Surface diffusion
Subcritical cluster
Stable cluster
Thermal accomodation
(a) Nucleation
Island (Volmer-Weber)
Layer-by-layer (Frank-van der Merwe)
Stranski-Krastanov
(b) Growth

Figure 2.2 Nucleation and Growth modes[29]

2.1.2 Glassy Carbon

As previously shown, the choice of substrate affects the binding energy and thus the growth mode. Within the scope of this work, both metallic (brass) and non-metallic (glassy carbon) substrates were used.

Considering the latter, glassy carbon (GC) is an agranular non-graphitizable type of carbon. It has a low permeability to liquids and gases and its original and fractured surfaces have a glassy appearance, hence its name[30]. The use of glassy carbon as a substrate holds many advantages. These include, its usability over a wide potential range in aqueous and organic solutions[31,32], stability in highly acidic or alkaline solutions, and chemically inert due to its very small pore size and low oxidation rates at high temperatures[33]. This makes it very suitable as a catalyst support. Figure 2.23[34] shows a structural model of glassy carbon.

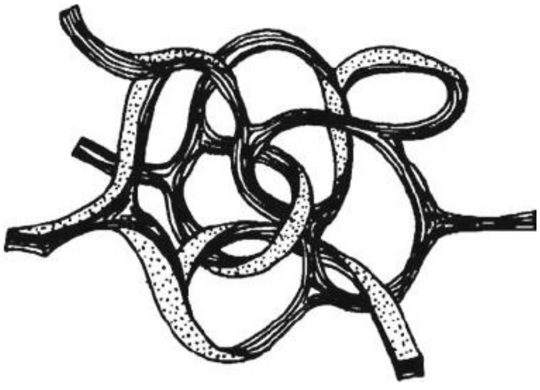

Figure 2.3 Structural model of glassy carbon[34]

For iridium and chromium deposition, the very high overpotential for the hydrogen evolution reaction (HER) on glassy carbon plays an important role, since the deposition potential for both metals occurs far into the HER region. In addition, due to its amorphous structure, GC exerts no epitaxial effects onto the deposits, which was vital to be able to assess the intrinsic structural properties of the deposits. Due to the absence of epitaxy, chromium hydride crystals could be deposited on GC[35].

However, for electrochemical deposition to take place on GC, the surface needs to be prepared and activated. Surface preparation is mainly achieved by mechanical polishing using abrasive particles, to have an even, smooth surface[2,7,42–45,33,35–41]. On the other hand, such polishing techniques deactivate the surface of the electrode, which then needs to be re-activated, either thermally, chemically or electrochemically. The aim behind the activation of the surface is to increase the rate of electrode reaction, thus decreasing over potential, increasing sensitivity and resolution, and narrowing peak width[40]. The reason behind such activation could be attributed to the removal of contaminants from the surface and the increase in the surface functional groups, which mediate electron transfer[41].

2.1.3 Side reactions

Metal deposition is usually accompanied by other reactions at the cathode. While these reactions may sometimes hinder or disturb deposition, however within the scope of this study, HER, which is a side reaction for both iridium and chromium deposition, was important to achieve and monitor the deposited species.

In the case of iridium deposition, the adsorption of hydrogen onto iridium nuclei catalyzes further reduction of iridium ions onto the nucleus, allowing the particles to grow[24]. This is due to the preferential adsorption of hydrogen onto iridium, than on GC.
This is demonstrated in Figure 2.4[24].

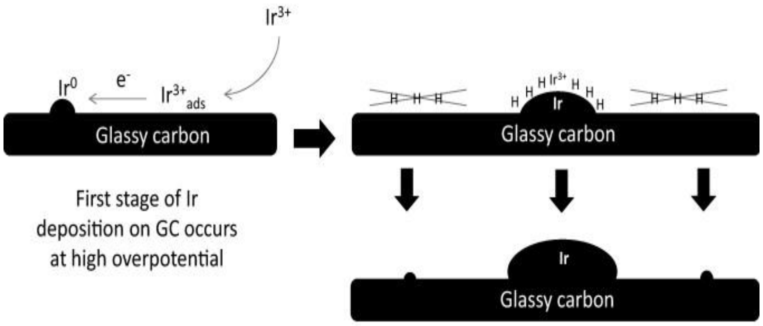

Figure 2.4 Schematic of iridium deposition on glassy carbon[24]

For chromium deposition, the HER plays two roles; the first of which is the incorporation of hydrogen into the lattice, which gives rise to hexagonal chromium hydride crystals. In the absence of strong hydrogen evolution, along with continued deposition, these structures cannot be stabilized. In order to determine if deposition was still progressing, the HER currents were used to monitor deposition. Since hydrogen evolution occurs on metals and not on the GC surface, an increase in HER current would therefore mean an increase in chromium content on the surface. Figure 2.5a shows an example of consecutive cyclic voltammograms where the HER current was used to probe the deposition process, while Figure 2.5b shows an SEM image of a hexagonal chromium hydride crystal.

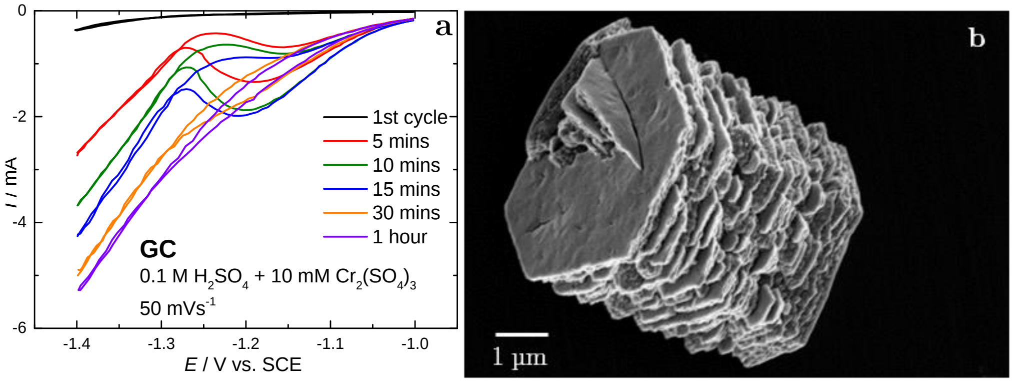

Figure 2.5 (a) Current—potential curves for the potentiodynamic deposition of chromium hydride crystals on GC showing the increase in HER current as deposition time increases (b) SEM image of the deposited chromium hydride on GC

2.2 Coordination Chemistry

2.2.1 Overview

Coordination chemistry deals with the formation of complex molecules. These consist of a central ion or atom (coordination center), that is coordinated with ions or molecules that form a ligand shell surrounding the coordination center. The number of ligands that can be chemically bound to the central atom/ion is known as the coordination number[46]. Since both iridium and chromium form complexes, understanding the properties of such systems is essential to tackle the challenges involved with electrodeposition.

It is important to differentiate between complex molecules, ionic and covalent compounds. Ionic compounds are formed by the electrostatic interaction between positively charged and negatively charged ions, where the former donates an electron to the latter. Covalent compounds arise from sharing an electron pair between two atoms; each of the two atoms provides an electron to the covalent bond. In a complex molecule, however, the ligand is bound to the central atom/ion by overlapping a filled orbital of the ligand, with an empty orbital of coordination center. In other words, a covalent bond is formed, where the ligand provides both electrons[46]. The ligand shell, made up of all the ligands bound to the central atom form the first coordination sphere surrounding the metal atom[47]. If the ligands are charged, the total charge of the complex will be different from that of the central ion. This charged complex could then act as the cation or anion in an ionic compound. For example, if we consider Potassium hexachloroiridate (III), which has the formula K_3IrCl_6, Ir^{3+} is coordinated with six chloride (Cl^-) ions, thus the charge of the complex is $[IrCl_6]^{3-}$. This complex now serves as an anion to potassium cations (K^+). Upon dissolution in water, the ligands do not dissociate from the complex[46], rather in solution will be K^+, and $[IrCl_6]^{3-}$.

Given that the ligands are identical, the bond strength between the central atom and each of the ligands, and hence the bond length, will also be identical, giving rise to regular geometries, since the structures are governed by the overlap between metal and ligand orbitals, as well as the repulsion between the ligands. Thus, depending on the coordination number, complexes have regular geometrical structures, as shown in Figure 2.6[48].

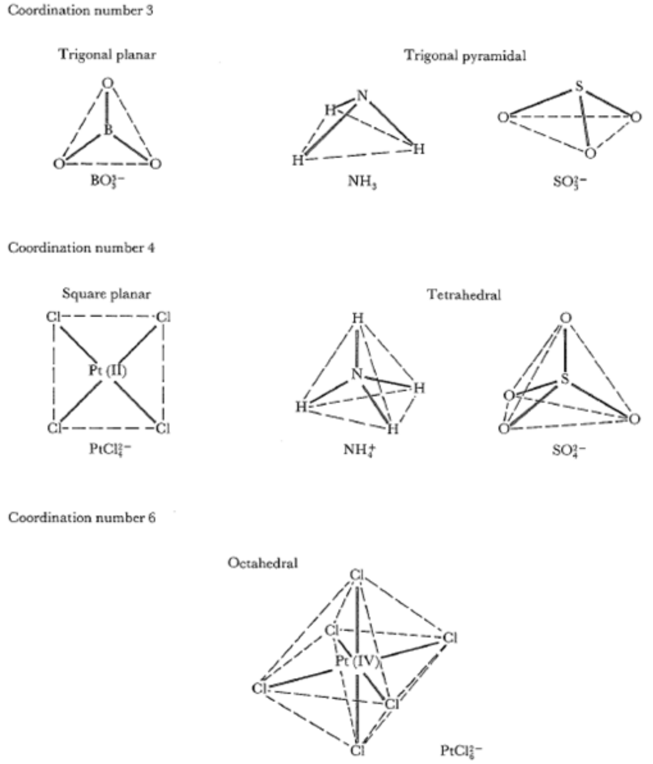
Coordination number 3
Trigonal planar
Trigonal pyramidal
BO$_3^{3-}$
NH$_3$
SO$_3^{2-}$
Coordination number 4
Square planar
Tetrahedral
Pt (II)
PtCl$_4^{2-}$
NH$_4^+$
SO$_4^{2-}$
Coordination number 6
Octahedral
Pt (IV)
PtCl$_6^{2-}$

Figure 2.6 Geometric structures of complexes based on their respective coordination numbers[48]

If the ligands are not identical, however, the structure becomes irregular. This phenomenon is advantageous when trying to destabilize the chromium hexaquo-complex in order to facilitate electrodeposition, by introducing an organic ligand to substitute at least one of the water molecules[15], for example.

2.2.2 Octahedral Complexes

Throughout this work, the characterization of chromium complexes played an important role for the continuous development of the process. Since trivalent chromium forms octahedral complexes, a fundamental understanding of the ligand field theory is important for evaluating the UV-VIS spectra, which were the primary characterization technique for the formed chromium complexes.

Transition metal ions have five d-orbitals. As a free ion, each of these orbitals are energetically identical. Upon formation of an octahedral complex with six coordinated ligands, electrostatic repulsion takes place between the d-electrons of the central ion and the lone pairs of the ligand. This in turn causes an increase in the energy levels of the d-orbital. However, the magnitude of the repulsion forces is not uniform; the d-electrons closer to the ligand's electron cloud are more affected than those that are further away.

Thus, it is energetically favorable for the *d*-electrons closer to the lone pair of the ligand to move into orbitals further away[46]. The *d*-orbitals are split into two groups, in relation to the energy of a hypothetical spherical ligand field; one with a higher energy level (e_g), and one with a lower energy level (t_{2g}), as illustrated in Figure 2.7[49].

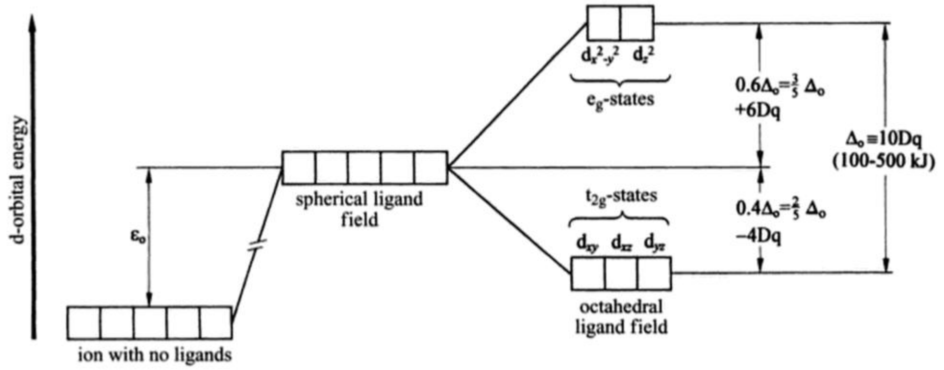

Figure 2.7 Ligand field splitting of d-orbitals[49]

Figure 2.7 shows that the ligand field splitting (Δ_0), can have a value of 100-500 kJ. For complexes of the same metal ion, this is determined by the nature of the ligand. Each ligand has a certain affinity to split the d-orbitals, and hence the ligands are ordered in the spectrochemical series, based on how large their ligand filed splitting is.

The larger the value of Δ_0, the higher the energy required to excite an electron from the t_{2g} state to the e_g state. Using photons for electron excitation, this means that a higher energy translates to a smaller wavelength. Here, it should be made clear that the color seen is the complementary color of the portion of light absorbed by the complex. For example, a green complex absorbs the red portion of light.

Therefore, such a phenomenon makes it possible to identify complexes, based on the absorbed wavelengths, using UV-VIS spectroscopy. In addition, peak shifts can also be used to determine whether a ligand exchange reaction occurred or not, and if the new ligand causes a larger or smaller splitting of the ligand field.

2.3 Chromium

2.3.1 Overview

Chromium was first discovered in 1797 in Crocoite, a mineral consisting of lead chromate, but it was not until 1894 that pure chromium metal could be obtained from the ore. It was named chromium, which is derived from the Greek word "chroma", translating to color, because of the many colorful compounds it forms[16]. Chromium is mostly present in the form of Chromite, an iron chromium oxide. The majority of the extracted chromium is used for chromium plating, alloying for corrosion resistant super-alloys, and the production of stainless steel. Electrodeposited chromium is perhaps the most important plated metal, mainly as the final deposit on parts, due to its advantageous physical and chemical properties, which enhance the performance and/or the optical appearance of the plated part[28].

Electroplated chromium layers offer an enhancement in mechanical properties of the plated base metal, in particular hardness and wear resistance[50]. More importantly, they resist corrosion and tarnishing, thus maintaining a superior optical appearance. While chromium has a standard potential suggestive of a base metal and would thus be expected to corrode like iron, for example, it forms an oxygen-induced passivation layer which allows it to be have similar to noble metals[51]. It is because of these properties, that people have been industrially modifying materials with electroplated chromium layers since the early 1900's[28].

Depending on layer thickness, chromium deposits can be classified as decorative or functional: Decorative deposits are usually less than 0.8 µm thick. They not only provide shiny, reflective finish, but are also providing corrosion resistant, and durable. Functional, or hard, chromium deposits on the other hand, have a thickness customarily greater than 0.80 µm and are used for industrial applications. For such applications, chromium offers lucrative properties, such as heat resistance, increased hardness, wear and corrosion resistance, as well as decrease in friction[28].

2.3.2 Complex chemistry of Trivalent Chromium

As a transition metal, chromium has diverse redox chemistry. Complex compounds of chromium with oxidation numbers from -I to VI are known, with complexes of Cr (II), Cr (III), and Cr (VI) occurring much more frequently than those of the other oxidation states[16]. Out of all possible oxidation states, trivalent chromium is the most stable, usually six-fold coordinated in an octahedral environment[46].

Due to the octahedral symmetry, the five *3d*-orbitals are split into an e_g and a t_{2g} orbital set, as previously described in Section 2.2.2. Trivalent chromium has a d3 electron configuration. The three t_{2g}-orbitals in the most stable state are each occupied by one electron.

Since only the energetically lower orbitals are occupied, octahedral Cr (III) complexes are energetically very favorable and therefore stable. Consequently, a ligand exchange is associated with a high activation energy, which is why these complexes are considered to be kinetically inert and that ligand-exchange reactions can exhibit half-lives in the range of hours[20,46,52].

Characteristic of Cr (III) complexes with aquo ligands is the formation of polynuclear complexes by condensation. Depending on the pH, temperature and concentration of the solution; dimers, trimers, and higher oligomers can be formed by hydroxide-ligand bridging[46,52] The dependence of the degree of oligomerization on solution pH of a dilute Cr (III) solution is shown in Figure 2.2[53].

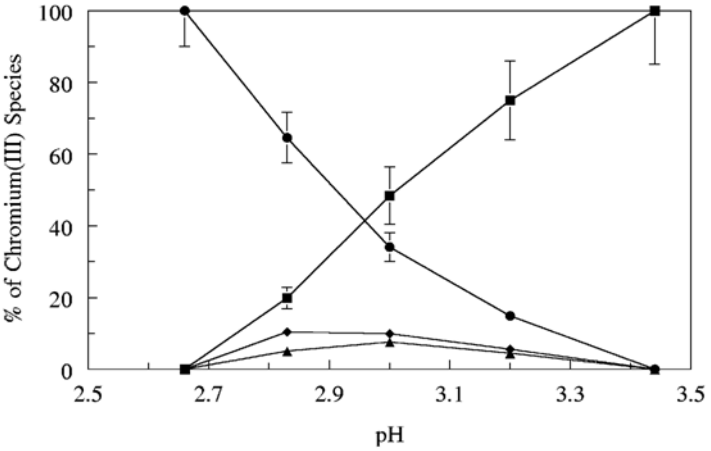

Figure 2.8: Dependence of degree of oligomerization on pH in a 0.05 M Cr (III) solution. Symbols: monomer (●), dimer (◆), trimer (▲), unseparated higher oligomers (■)[53].

This influence of pH is transferable to concentrated solutions; whereby the formation of polynuclear complexes shifts to lower pH ranges as the chromium concentration increases[54].

With regard to the pH of chromium-containing solutions, it should be noted that the pure aquo-complex of trivalent chromium has a *pKa* value of about 4, and thus its behavior is acidic, similar to formic acid[52].

$$[Cr(H_2O)_6]^{3+}_{(aq)} \rightleftharpoons [Cr(OH)(H_2O)_5L]^{2+}_{(aq)} + H^+_{(aq)}$$

The dissociation of one of the water ligands into a hydroxo ligand and a proton is what causes the solutions to be acidic. The hydroxo ligand can then condense to give rise to single or double hydroxo-bridged dimers[28].

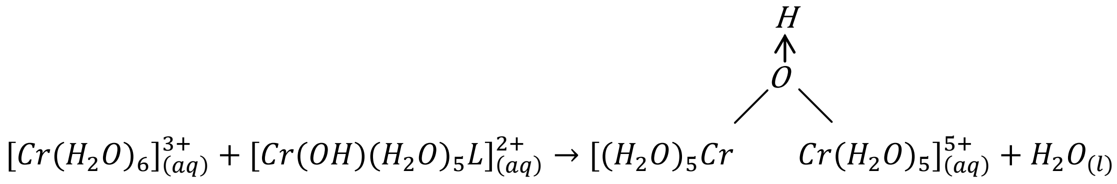

$$[Cr(H_2O)_6]^{3+}_{(aq)} + [Cr(OH)(H_2O)_5L]^{2+}_{(aq)} \rightarrow [(H_2O)_5Cr \overset{\overset{H}{\uparrow}}{O} Cr(H_2O)_5]^{5+}_{(aq)} + H_2O_{(l)}$$

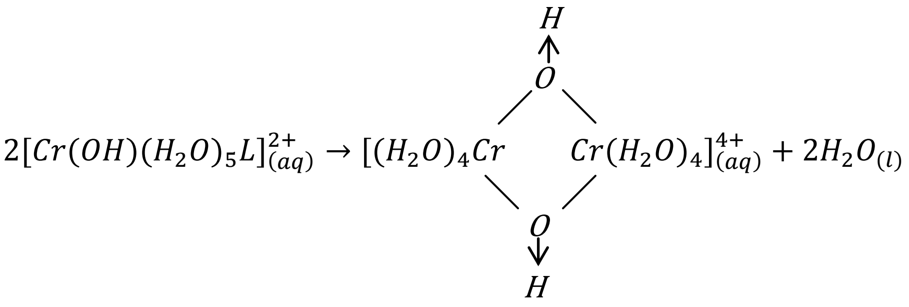

$$2[Cr(OH)(H_2O)_5L]^{2+}_{(aq)} \rightarrow [(H_2O)_4Cr \underset{\underset{H}{\downarrow}}{\underset{O}{\overset{\overset{H}{\uparrow}}{\overset{O}{\quad}}}} Cr(H_2O)_4]^{4+}_{(aq)} + 2H_2O_{(l)}$$

The above process is referred to as olation. Continued olation results in polymerization of the trivalent chromium species, which can reach the extent of precipitation of chromium hydroxide. This process is accelerated by heating, an increase in pH, or an increase in concentration[28].

Olation and consecutive polymerization result in a decrease in active species for electrodeposition. The larger the molecule, the more difficult it is to deposit. In other words, an inconsistent behavior of the bath would be expected. In order to prevent this, anions are added to the solution that coordinate to the chromium ion stronger than the hydroxide ligand. These, along with other additives, will be discussed in Section 2.3.4.

2.3.3 Electrodeposition of Chromium

For a long time, chromium deposition was performed almost exclusively from hexavalent chromium solutions, whereas deposition from trivalent chromium electrolytes was considered impossible[55]. It was only in the 1970s that the first methods for decorative chromium plating with Cr (III) were commercially employed[56]. A market study published in 2009 revealed that until the date of the data collection no hard chromium plating baths with Cr (III) were available[51]. Since hexavalent chromium, which has been mainly used so far, is toxic, carcinogenic, and soon to be prohibited by legislation, there is an increasing demand for a less hazardous process[17].

Chromium plating based on trivalent chromium is a promising alternative, but also presents special challenges, mainly since Cr (III) forms very stable hexaquo-complexes in aqueous solutions, which cannot be directly reduced, due to their stability[22,55].
To counteract this problem, complexing agents are added, which undergo ligand exchange reactions with the water ligands attached to the chromium. Ligand exchange increases the distance between the chromium center and the remaining aquo ligands, disturbing the regular octahedral structure[22,57], which leads to an easier elimination of further water molecules and a smaller distance between the cathode and the trivalent chromium ion, accelerating the electron transfer for the reduction[23]. Often, salts of organic acids, urea or hypophosphites are used as complexing agents[56]. The resulting complexes are thermodynamically more stable than the hexaquo complex.

Another challenge is that the reduction reaction of Cr (III) to chromium has a standard reduction potential of −0.74V.

$$Cr^{3+}_{(aq)} + 3e^{-} \rightarrow Cr_{(s)}$$

Thus, a higher potential is required for the chromium deposition from acidic solution than for the hydrogen evolution, the standard reduction potential of which is defined as 0 V. Accordingly, hydrogen is always formed at the cathode during the chromium deposition, as a result of which the efficiency of the process significantly decreases.

$$2H^{+}_{(aq)} + 2e^{-} \rightarrow H_{2\,(g)}$$

Due to hydrogen evolution, the pH at the cathode rises locally, which may lead to the olation of the chromium species in solution, which limits further chromium deposition. This is described in section 2.3.2.

These problems could be solved by using non-aqueous solvents, which is very difficult to implement in industrial applications. In addition, research in this area has yet to show any promising results[22].

In aqueous solution, the reduction of chromium complexes takes place with stripping of the ligand shell at the cathode.

$$[Cr(H_2O)_5L]^{2+}_{(aq)} + 3e^{-} \rightarrow Cr_{(s)} + 5H_2O_{(l)} + L^{-}_{(aq)}$$

Based on mechanistic investigations, a two-step reaction sequence with a Cr (II) intermediate is proposed for the reduction process.

$$[Cr(H_2O)_5L]^{2+}_{(aq)} + e^{-} \rightarrow [Cr(H_2O)_5L]^{+}_{(aq)}$$

$$[Cr(H_2O)_5L]^{+}_{(aq)} + 2e^{-} \rightarrow Cr_{(s)} + 5H_2O_{(l)} + L^{-}_{(aq)}$$

The standard reduction potentials in this case, excluding the ligand sphere, are -0.41 V for the first step and -0.91 V for the second step[56,57].

The first deposited chromium layers inherit the texture of the underlying metal. Therefore, a smooth and low-defect substrate is essential for smooth and shiny deposit, especially when it comes to decorative chromium. In order to achieve such a substrate, parts are usually plated with nickel first, which also enhances the corrosion resistance. The more shiny the nickel layer, the shinier the chromium layer deposited on it. As the thickness of the chromium layer increases, the influence of the substrate texture decreases. Therefore, for hard chromium layers, a nickel undercoat is not required[51].

2.3.4 Trivalent Chromium Bath Additives

For an industrially functional trivalent chromium bath, a combination of additives are required to achieve the desired optical and thickness requirements. These additives include inorganic compounds, the most important of which is Boric acid, and organic additives, which are usually classified as complexing agents, wetting agents, and brighteners.

Boric acid is a main ingredient in many plating baths, not just chromium[44,45,58]. While most of literature claims that boric acid is a pH buffering agent, however, since boric acid has a pKa value of 9.24, it is highly unlikely that boric acid acts as a buffer in acidic electrolytes. This is also supported by measurements that were performed, that show no significant difference between deposition with and without boric acid on GC electrodes. However, for deposition on metallic substrates, the presence of boric acid was essential to obtain a deposit in the first place.

This behavior could be related to the reduction of boric acid at very negative potentials the metal surface[59].

$$B(OH)_3 + 7H^+ + 8e^- \rightleftharpoons BH_4^- + 3H_2O \qquad E_0 = -0.481\ V$$

The equation shows that this reaction consumes seven hydrogen ions, which would be readily present at the surface, since chromium deposition occurs deep within the hydrogen evolution region. By adsorbing on the surface, there would be a local hindrance of hydrogen evolution, during which the chromium ions can adsorb on the surface, forming nuclei, which allow for further film growth. However, to date, the mechanism by which boric acid facilitates metal deposition remains unknown.

Of the organic additives, perhaps the most vital would be the complexing agents, since they modify the molecule's structure, and prevent olation, both of which are essential to obtain active chromium species[60]. These are typically organic anions higher up the spectrochemical series than aquo ligands, and thus can undergo a ligand exchange reaction with at least one of the water molecules. This in turn distorts the octahedral structure of the complex, allowing an easier path for the chromium center to reach the electrode surface[23].

At the right concentrations, wetting agents and brighteners allow for increased homogeneity, as well as current efficiency at low current densities[61]. This is because they adsorb on the surface during deposition, thus blocking active sites and reducing nucleation rate, which allows the existing nuclei to grow into a homogeneous film[62,63].

2.4 Iridium

2.4.1 Overview

Iridium is a noble (or platinum group) metal. It has the atomic number 77, and is considered the most corrosion resistant metal known. It was discovered in 1803 while examining the black residue left after dissolving crude platinum in aqua regia. It is also a very hard and brittle material, making it very difficult to machine. It is also unattacked by any acid nor aqua regia, however, it can be attacked by certain molten salts, like sodium chloride and sodium cyanide[59].

Like most noble metals, the electrocatalytic activity of Iridium makes it a metal of interest. Studies have shown that Iridium has the highest activity for the Oxygen Evolution Reaction (OER)[2]. The reason behind this is that Iridium has the largest number of free d-electrons per atom of the noble metals, after Ruthenium, which has a very low stability. This implies that iridium will from strong metal-hydroxyl bonds, thus resulting in a low overpotential. The value of the overpotential is always preferred to be a minimum, since this anodic process is a major source of energy loss in reactions like the electrolysis of water, for example. It is also one of the few metals whose oxide acts as a metallic conductor[64].

The use of noble metals in catalysis has many advantages. These include the ability to be used at high temperatures and in aggressive acidic media. They also are degradation resistant upon the exposure to air or upon being subjected to temperature cycles[65]. However, the use of noble metal bulk electrodes is extremely costly making them unfit for application. Hence, finding new ways to decrease the amount of noble metal catalysts used while maintaining a good catalytic efficiency is of paramount importance for the widespread use of such systems.

Research on nanoscaled catalysts has gained a lot of interest in the past few years. One of the highlights of such research is the possibility of synthesizing nanocrystals with well-defined shapes. It has been shown that catalytic efficiency, as well as the chemical and physical properties, of the nanocrystal is not only dependent on its size, but also on its shape[6]. Thus, surface structure plays an important role in catalytic activity. This has therefore opened up a new possibility for the widespread use of noble metal catalysts. By using shape-controlled nanoparticles supported on a substrate, the catalytic efficiency can be improved, while greatly reducing the amount of noble metal loading on the electrode, and thus decreasing the cost

2.4.2 Electrochemical Deposition of Iridium

Electrochemical metal deposition is a fast and convenient method to deposit nanocrystalline metallic particles on a conductive substrate[66]. Using such a method to prepare noble metal electrodes is highly favorable due to its versatility, the high purity of deposits and the possibility to readily control the loading of the deposits. In addition, electrodeposited nanoparticles show higher adhesion to the substrate surface with respect to other chemical deposition techniques[24]. Moreover, chemical deposition techniques may require the use of a surfactant material, which may contaminate the catalyst being prepared.

One of the initial attempts to deposit Iridium from aqueous solution was done by MacNamara in 1962, where iridium was deposited onto a platinum electrode from chloriridic acid (H_2IrCl_6)[67]. More recently, the deposition under ultrasound sonification of Iridium from a solution of sodium hexabromoiridate (Na_3IrBr_6) was investigated[31]. Other studies also investigated the deposition of iridium onto silicon single crystals, porous nickel electrodes and gold substrates[32,68,69]. A more relevant investigation describes the deposition of iridium aggregates onto glassy carbon and platinum electrodes. Figure 2.9 shows the SEM image of such iridium aggregates deposited onto glassy carbon[24].

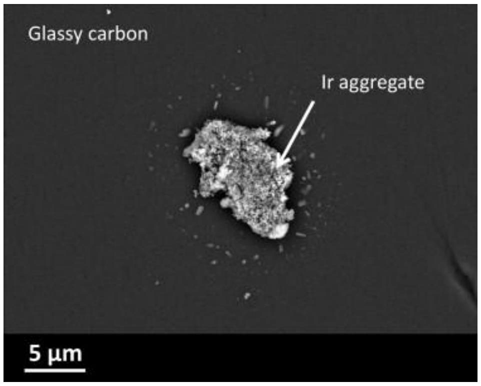

Figure 2.9 SEM image of an iridium aggregate on glassy carbon[24]

The randomly shaped aggregate in Figure 2.9 highlights the main challenge with Iridium deposition, which is that conventional deposition techniques do not yield consistent results. Nonetheless, the following mechanism for Iridium deposition on GC electrodes was concluded from this study[24].

$$Ir^{3+} \rightarrow Ir^{3+}_{ads}$$

$$Ir^{3+}_{ads} + 3e^{-} \rightarrow Ir^{0}$$

$$3H^{+} + 3e^{-} \rightarrow 3H_{ads}$$

$$3H_{ads} + Ir^{3-}_{ads} \rightarrow Ir^{0} + 3H^{+}$$

This shows that the adsorption of hydrogen is essential for Iridium deposition, as previously explained in Section 2.1.3.

2.4.3 Iridium Electrocatalysis

Catalysis is the use of a material, a catalyst, to increase the rate of a certain reaction that would not occur, or would occur very slowly, in the absence of the catalyst. This increase in reaction rate should not be accompanied by a change in the standard Gibbs energy change of the reaction. An ideal catalyst is one that does not get used up in the reaction process; it is both a reactant and a product of the reaction[30]. Figure 2.10 illustrates a simplified energy diagram with and without a catalyst.

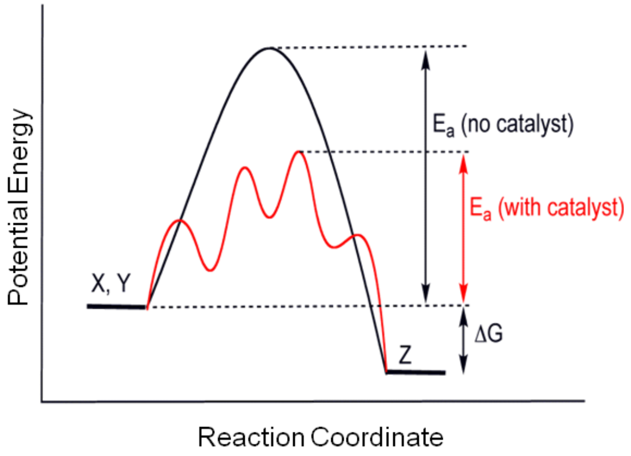

Figure 2.10 Energy diagram for a system with (red) and without (black) a catalyst, adopted from[30]

E_a represents the activation energy required of the reaction. This energy needs to be provided to the reactants, in the form heat, electricity, etc. and once this amount of energy is larger than the activation energy, then the reaction can take place. In the presence of a catalyst, however, it can be shown from the red curve that the amount of energy required to activate the reaction decreases and thus the reaction can occur at higher rates. It should finally be noted that the difference in potential energy for the reaction remains the same with and without using a catalyst.

Iridium is one of the most promising oxygen evolution reaction (OER) catalysts[2,70–72]. Its stability makes it a better candidate than Ruthenium, which has an even higher electrocatalytic activity, as shown in Figure 2.11[2].

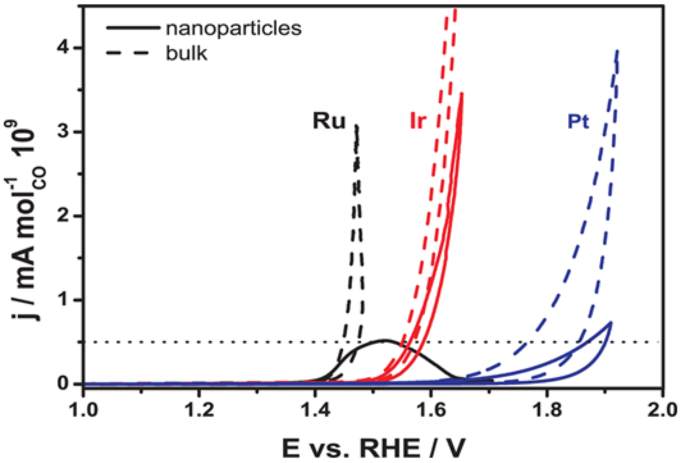

Figure 2.11 Comparison between the activities of bulk (dashed) Pt, Ru, and Ir and their nanoparticles (solid) for the OER[2]

The graph in Figure 2.11 shows that despite the higher overpotential required for the OER to occur on Iridium, its activity is nevertheless higher, especially if the nanoparticles of each metal are compared to one another.

In this work, the electrocatalytic activity of Iridium towards carbon monoxide (CO) adlayer oxidation was investigated, in order to electrochemically characterize the surface of the deposited Iridium particles. CO adlayer oxidation is used as a surface test reaction due to its simplicity and its functionality as a neutral probe to both surface sensitivity and activity[73]. Moreover, the electrochemical active surface area (EASA) could be determined from CO adlayer oxidation. The effects of modifying the surface roughness on CO adlayer oxidation behavior of the particles is shown and discussed in Section 4.1.3.

3 Experimental Methods

3.1 Electrochemical Techniques

All electrochemical measurements were performed using one of three types of potentiostat/galvanostat devices. The first is a HEKA PG510 Potentiostat/Galvanostat combined with a homemade square wave generator and controlled by homemade LabView software. The second is a Metrohm Autolab PGSTAT 128 Potentiostat/Galvanostat, controlled by the NOVA 1.11 software. Lastly, for the larger samples a VOLTCRAFT LSP-1165 voltage/current supply was used, where a current output higher than 0.8 A is possible.

3.1.1 Cyclic Voltammetry

Cyclic voltammetry (CV) is one of the most powerful and widely used electrochemical techniques. The sample under investigation, the working electrode (WE), is brought into contact with the solution under potential control. This is the initial potential (E_i), from which the potential is scanned to the lower potential limit (E_A), and then the scan direction is reversed until the positive potential limit (E_B) is reached, all with a predetermined scan rate. All the potentials are measured against a reference electrode (RE), which in this work was a Saturated Calomel Electrode (SCE). The current flowing between the WE and a counter electrode (CE) is recorded by the potentiostat, and plotted against the applied potentials. The resulting graph is characteristic for each system; hence the essential use of cyclic voltammetry was to characterize the system before deposition to ensure a reproducible quality at the start of each measurement, and to determine the success of deposition afterwards. Cyclic voltammetry of noble metals, such as iridium in aqueous solutions, display peaks for the adsorption and desorption of hydrogen and oxygen species[74].

By controlling the upper and lower potential limits of the cyclic voltammogram, it is also possible to alter the surface properties of the working electrode, by controlled oxidation and reduction. This technique is used to activate the surface of the glassy carbon electrodes in 0.1 M H_2SO_4, prior to electrodeposition experiments[40,41], and also to increase the roughness of the pre-deposited iridium spheres. The electrochemical activation of glassy carbon (GC) electrodes is discussed in more detail in section 3.4.1.

Within the scope of this work, cyclic voltammetry has also been employed to potentiodynamically deposit chromium hydride crystals onto glassy carbon. This allows for the removal of hydrogen from the surface and thus further particle growth is possible. This is discussed in depth in section 4.2.2.

3.1.2 Pulsing Methods

In this work, two types of pulsing techniques were employed for electrochemical deposition; square wave potential (SWP) pulsing for iridium, and galvanic pulsing techniques for chromium.

The SWP technique consists of a cleaning pulse at 1.2 V for 1 second, a nucleation pulse of potential E_n for a time (t_n) of 10 ms, and a square wave to simultaneously reshape and grow the spheres by consecutive adsorption and desorption of oxygen at the upper (E_u) and lower (E_l) potential limits respectively[12]. A schematic of the employed SWP program can be seen in Fig 3.1.

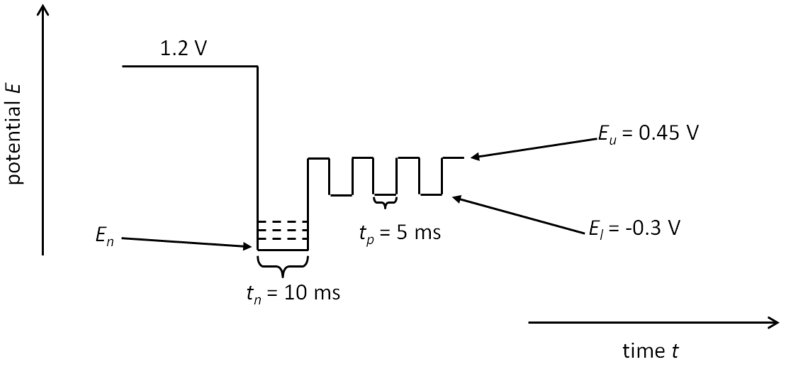

Figure 3.1: Schematic of the SWP profile used for electrodeposition of Ir nanospheres

Nucleation is achieved by a very short pulse with a very negative overpotential, to allow progressive nucleation at the active sites[66], while overcoming the formation of hydrogen bubbles on the surface that block active sites[38].

In the case of galvanic pulsing, a negative current pulse (I_L) is used to galvanostatically deposit chromium for a pulse duration of t_L, followed by a zero current pulse, I_U, for a pulse duration of t_U. These pulses could be symmetric or asymmetric, therefore an additional parameter, cycle duration (t_C) is fixed, so that for all measurements; $t_L + t_U = t_C$. The program is applied for a plating time of t_T. This is illustrated in Figure 3.2.

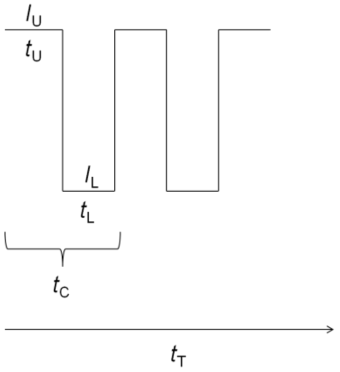

Figure 3.2: Schematic of the galvanic pulsing technique used for Cr deposition

3.1.3 Galvanostatic Deposition

Galvanostatic deposition has a major technological relevance, since it is the most commonly employed electrodeposition technique, due to apparatus simplicity, ability to maintain bath parameters, ensure reproducible quality and to minimize waste. Since potential control is not a part of the process, a reference electrode is not needed and hence the apparatus is simplified to a two-electrode system consisting of anode and a cathode, the part to be plated. Typically, parts are electroplated with a certain current density (j), measured in A dm^{-2}, for a certain duration. For the majority of the galvanostatic measurements in this work, a cathodic current density between 5 and 10 A dm^{-2} was used for durations ranging from 5 to 10 minutes. The anodes used were graphite electrodes, in the case of GC, and mixed metal oxide (MMO) anodes in the case of metal surfaces.

3.2 Ultraviolet-Visible Spectroscopy

The absorption of light in the ultraviolet and visible range is based on the electronic excitation of molecules or complexes, and is governed by the following equation,

$$\Delta E = h\nu$$

where ΔE is the energy required for excitation, ν is the frequency of the absorbed light and h is Planck's constant.

Since these electronic excitations are coupled with changes in the vibrational and rotational states, they result in absorption bands, instead of the expected sharp spikes related to the energy difference between the different electronic states. Thus the absorbance, or extinction E_λ, is dependent on the wavelength-specific molar extinction coefficient ε_λ, the concentration of the solution c, and the length of the path taken by the light in the solution l, according to the Beer-Lambert law[20,75,76].

$$E_\lambda = log\frac{I_0}{I} = cl\varepsilon_\lambda$$

The molar extinction coefficient at the maximum of the absorption band is proportional to the square of the transition dipole moment and thus to the probability of the electronic transition. Since this probability is different for each light absorbing species, the location of the extinction maximum and the associated molar absorption coefficient can be used to distinguish different substances.

Therefore, this spectroscopic method was used to identify changes in the chromium complex at different preparation stages, using an Agilent Technologies Cary 60 UV-Vis spectrometer.

In complexes, charge transfer transitions, opposite to the electronic excitation of the d-electrons within the central atom, are associated with a large spatial shift of the electron, resulting in a significantly larger transition dipole moment, leading a higher molar absorption coefficient. The electron transfer can proceed from the ligand to the metal as well as from the metal to the ligand[75].

3.3 Surface Characterization Techniques

3.3.1 Scanning Electron Microscopy (SEM) and Energy Dispersive X-ray Spectroscopy (EDX)

In SEM, a focused electron beam is scanned across the sample surface, which is inserted into a high vacuum chamber. The electron column is under ultrahigh vacuum (UHV) conditions to avoid as much beam diversion as possible. The electron column contains the electron gun, and two or possibly more electron lenses to guide the electron beam onto the sample.

The electron gun of the SEM can generate electrons and accelerate them to an energy value within a range of 0.1-30keV. This electron beam is given off a tungsten hairpin gun, which produces a spot size that is too large to get a sharp image. Magnetic lenses demagnify the beam to have a much smaller spot focused onto the sample. Then the deflection system causes the beam to move along a rectangular raster, which simultaneously generates a similar raster on the screen[77].

By inelastic collisions of the irradiated primary electrons with the atoms of the sample surface, secondary electrons are released from the atoms. The penetration depth of the primary electrons is dependent on the acceleration voltage of the electrons and the angle of incidence of the beam. The spatially resolved detector signals resulting from the impact of secondary ions on the detector are combined by software to form an overall image. Since more secondary electrons are emitted at edges and corners than in flat surfaces, they appear bright. Surfaces that are perpendicular to the detector appear brighter than surfaces that have a different inclination. The images generated by the SEM are therefore quite comparable to the visual perception of surfaces[78,79].

In addition to quantifying the secondary electrons for topographic analysis, the elemental composition of the surface was also analyzed by EDX, using an XMax 50 detector attached to the ZEISS LEO 1550 VP SEM apparatus used. The secondary electrons, which come from the near-nuclear levels of the sample atoms, leave vacant or partially occupied energetically favorable orbitals. These orbitals are filled with electrons from higher energy levels, emitting the excess energy as X-rays. Since the emitted X-ray radiation has specific frequencies for each element, the combination of SEM and energy dispersive X-ray spectroscopy (EDX) allows an elementarily resolved image of the surface to be scanned[80,81].

3.3.2 X-Ray Fluorescence (XRF) and Spectral Photometry

In order to evaluate the properties of the deposited chromium film, it is necessary to determine the film thickness, as well as the optical appearance of the film. These properties were assessed using X-Ray Fluorescence (XRF) and Spectral Photometry.

The thickness of the electrodeposited chromium layers on metallic substrates was determined using a FISCHERSCOPE X-RAY XDV-SDD device. This method for determining the layer thickness is based on the analysis of element-specific XRF[82].

By irradiation of X-ray photons, an electron in a low energy orbital from the substrate atom is knocked out. To fill the gap, an electron of the same atom is transferred from a higher energy orbital to the incompletely occupied lower energy orbital. As the electron passes into a more stable state, it has to give off energy. If the energy is emitted in the form of X-rays, the process is called X-ray fluorescence. The emitted wavelengths are characteristic of each element[75,82].

The measurement of X-ray fluorescence is a commonly employed non-destructive method to measure layer thicknesses. It exploits the fact that the intensity of the X-ray fluorescence of an element is proportional to the thickness of the corresponding layer[83]. By calibration with layers of known thickness, in the case of chromium, layers with a thickness of up to 40 µm can be determined with good accuracy. At higher layer thicknesses, the determination is no longer possible, since the increase in intensity of the X-ray fluorescence is minimal, in comparison to the further increase in film thickness[82]

In addition, the thickness of the deposited metal layer can also be determined by the absorption of the X-ray fluorescence by the background material. Both the incident X-ray radiation and the X-ray fluorescence emitted from the background material, are exponentially attenuated when penetrating the layer above. From the attenuation of the intensity, the thickness of the metal layer can also be calculated[82]. Taking this into consideration makes it possible to determine the thickness of deeper layers, in the case of multilayer systems[83].

For the evaluation of the optical properties of the chromium films, spectral photometry was used. This makes it possible to carry out an objective analysis of the optical appearance in addition to the subjective impression of the surfaces. This was done with a portable X-rite Ci6x spectrophotometer.

The principle is similar to that of a UV-Vis spectrometer, as described in Section 3.2. By comparing the light intensity reflected by the sample in certain sections of the spectrum, differences in color shades and brightness can be detected in comparison to previously determined reference points[84,85].

3.4 Preparation Techniques

3.4.1 Glassy Carbon

Prior to deposition, the surface of the GC electrodes should always have the same roughness. This was obtained by consecutive grinding, using silicon carbide grinding paper, and polishing, using alumina paste. The procedure is summarized in Table 3.1.

Table 3.1: Stepwise preparation of the glassy carbon surface

Step	Grinding/Polishing	Grit/Particle Size
1	Grinding	2500 grit SiC paper
2	Grinding	4000 grit SiC paper
3	Polishing	1.0 µm alumina suspension
4	Polishing	0.3 µm alumina suspension

After each step, the GC electrodes were rinsed with Milli-Q water, with a specific resistivity of 18.2 MΩ cm, in an ultrasonic bath, to remove any inclusions on the surface.

After the mechanical surface treatment, the GC electrodes were clamped onto a stainless steel rod using a crocodile clip, and wrapped in Teflon tape, in such a way that only the polished surface would come into contact with the solution. Next, the surface was cleaned/activated by a voltammetric treatment in 0.1 M H_2SO_4, thoroughly purged with nitrogen. After immersion at −0.1 V vs. SCE, the GC was subjected to five potential cycles, between −0.28 V and 1.20 V, at a scan rate of 50 mV s^{-1}. A typical cyclic voltammogram of an activated GC electrode is shown in Figure 3.3.

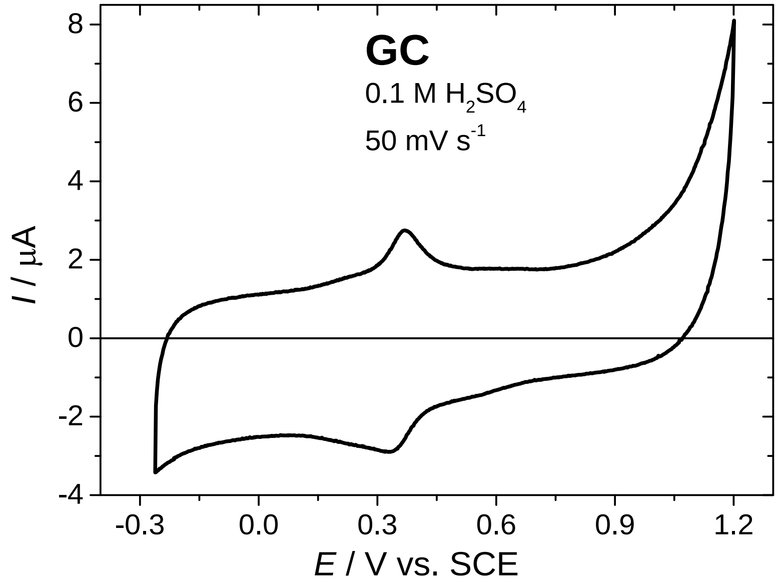

Figure 3.3: Typical cyclic voltammogram of an activated GC electrode in 0.1 M H_2SO_4 at 50 mV s^{-1}

The successful activation of the GC electrode is characterized by the emergence of the peaks at around 0.35 V, which are related to the quinone/hydroquinone redox couple[41].

3.4.2 Brass sheets

Electrodeposition measurements were mainly carried out on commercially available brass sheets, that were cut into squares, with an area of either 4 cm^2 or 16 cm^2. These were sometimes polished to a mirror finish, but due to the tedious process, this was not always the case. Prior to deposition, the substrates were rinsed with Milli-Q water, followed by Isopropanol, then again by Milli-Q water.

3.4.3 Glassware

Glassware was left in piranha solution (also known as caroic acid) overnight and afterwards rinsed thoroughly with Milli-Q water. Caroic acid was made in the lab by mixing concentrated sulphuric acid and a 30% aqueous solution of hydrogen peroxide, in a ratio of 3:1, respectively. The sulphuric acid is poured in a large glass container, and the hydrogen peroxide is introduced to the sulphuric acid drop wise, with the solution being mixed by a magnetic stirrer.

After the glassware has been in the caroic acid overnight, it is removed from the acid and rinsed thoroughly with Milli-Q water, and boiled out twice, to make sure that no traces of the solution are left on the glassware.

3.4.4 New Chromium (III) Solution

The preparation technique of the newly developed chromium (III) solution is very critical, in order to obtain the required result. While this will be discussed thoroughly in the upcoming chapter, the technical details on the preparation of the solution are briefly summarized in Table 3.2.

Table 3.2: Stepwise preparation technique of the newly developed Cr (III) plating solution

Step	Description
1	Dissolve 0.15 mol L^{-1} of Cr salt in 1 M H_2SO_4, while heating at 100°C for 3 hours
2	Allow to cool until the color of the solution changes from green to blue
3	Add 0.127 mol L^{-1} (17 g/L) Malic acid and heat at 65°C for 1.5 hours
4	Allow to cool, then adjust the pH to 1 using 50% NaOH solution
5	Add 0.81 mol L^{-1} (50 g/L) of Boric acid and heat at 65°C for 1.5 hours
6	Allow to cool, then adjust the pH to between 1.7 and 2 using 50% NaOH solution

3.5 Chemicals and Materials

In this section, a comprehensive list of all of the chemicals and materials used in this work are summarized in Tables 3.3 and 3.4, respectively.

Table 3.3: Details of the chemicals used

Chemical name	Chemical Formula	Purity/Amount	Manufacturer
Sulfuric Acid (Technical)	H_2SO_4	95–97%	Merck, Darmstadt
Hydrogen peroxide	H_2O_2	30%	Merck, Darmstadt
Sulfuric Acid (Suprapur)	H_2SO_4	96%	Merck, Darmstadt
Iridium (III) Chloride hydrate	$IrCl_3 \cdot xH_2O$	99.98%	Sigma-Aldrich, Steinheim
Carbon Monoxide	CO	4.7	MTI
Nitrogen	N_2	5.0	MTI

Chromium(III) Sulfate hydrate, trace metals basis	$Cr_2(SO_4)_3 \cdot xH_2O$	99.99%	Sigma-Aldrich, Steinheim
Chromium(III) Sulfate hydrate for synthesis	$Cr_2(SO_4)_3 \cdot xH_2O$	18 – 26% Cr	Sigma-Aldrich, Steinheim
Chromium (VI) Oxide	CrO_3	99.99%	Sigma-Aldrich, Steinheim
Chromium Hydroxide Sulfate	$Cr(OH)(SO_4)$	17% Cr	Vopelius Chemie AG, Fürth
Boric Acid	H_3BO_3	99.99%	Acros Organics, Geel
DL-Malic Acid	$C_4H_6O_5$	99.5%	Merck, Darmstadt
Sodium Hydroxide	NaOH	99%	Merck, Darmstadt
Sodium Sulfate	Na_2SO_4	99.99%	Merck, Darmstadt
Perchloric Acid	$HClO_4$	37%	Merck, Darmstadt
Isopropanol	C_3H_8O	100%	VWR International, Darmstadt

Table 3.4: Details of the materials used

Material	Manufacturer
Glassy Carbon Electrodes	HTW, Thierhaupten
2500 grit Grinding Paper	Bühler, USA
4000 grit Grinding Paper	Bühler, USA
1.0 µm Alumina polishing suspension	Bühler, USA
0.3 µm Alumina polishing suspension	Bühler, USA
Polishing Cloth	Bühler, USA
Polycrystalline Chromium Electrode	MaTeck, Jülich
Brass Sheet	Metallwarenfabrik Hirsch, Heusenstamm
Platinode MMO 187 LOC anode	Umicore, Schwäbisch Gmünd
Graphite rod (counter electrode)	Goodfellow GmbH, Germany
Saturated Calomel Electrode	SI Analytics, Mainz
Platinum wire and sheet (counter electrode)	MaTeck, Jülich

4 Results and Discussion

4.1 Electrochemical deposition of Iridium on GC Electrodes

In this section, the results of the study performed on the electrochemical deposition of Iridium are summarized. Prior to all deposition measurements, the GC electrodes were grinded, polished, and electrochemically activated as described in section 3.4.1. The deposition was performed out of a solution containing 0.5 M H_2SO_4 + 10 mM $IrCl_3$.

For CO adlayer adsorption, CO gas was bubbled in a solution of 0.1 M H_2SO_4 for 10 min with the iridium-loaded GC held at −0.1 V vs. SCE. The dissolved CO was purged out of the solution with nitrogen gas for 1 hour. The adsorbed CO adlayer was oxidized via a voltammetric scan up to 0.7 Vat 10 mV s^{-1}.

4.1.1 The influence of the nucleation potential E_n

The main challenge in iridium deposition is the successful nucleation of iridium on the GC surface. This is due to the fact that the nucleation potential for Iridium lies within the hydrogen evolution reaction (HER) region. Hence, the blockage of the surface by hydrogen bubbles hinders the formation of stable nuclei to support further growth. In order to investigate the nucleation behavior, a double step technique was employed to determine a suitable overpotential for nucleation. This included a nucleation potential (E_n) of −1.6 V vs. SCE for 200 ms, followed by a growth potential (E_g) of −0.2 V vs. SCE for 1 hour. The resulting voltammogram of the deposited iridium particles, along with an SEM image of the deposit are shown in figure 4.1.

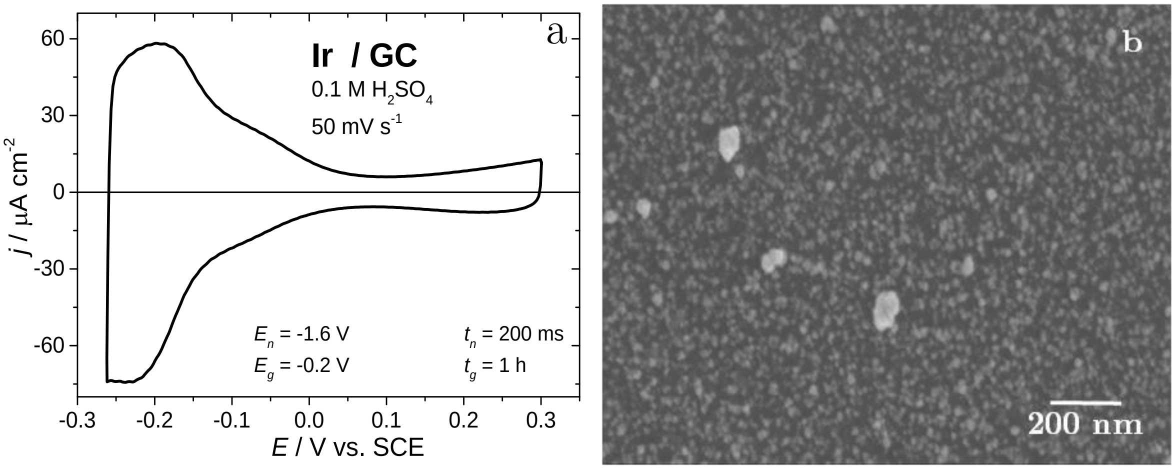

Figure 4.1 (a) Current–potential curve of the Ir nanoparticles, deposited on a GC electrode via the double-step technique, in 0.1 M H_2SO_4 at 50 mV s^{-1}, (b) SEM image of the deposit. Adapted by permission from Springer Customer Service Centre GmbH: Springer US, Electrocatalysis, Electrochemical Fabrication of Well-Defined Spherical Iridium Nanoparticles and Electrocatalytic Activity towards Carbon Monoxide Adlayer Oxidation by Sheasha et al. © Springer Science + Business Media New York 2015

Figure 4.1a shows the current–potential curve of the Ir nanoparticles, deposited on a GC electrode via the double-step technique, in 0.1 M H_2SO_4 at 50 mV s^{-1}. The current-potential curve shows two main regions. The region below 0 V contains the hydrogen adsorption peaks. These peaks are similar to those of Ir nanoparticles fabricated by Reier et al.[2]. The start of the double layer region is at around 0 V vs. SCE. Above 0.3 V, starts the surface oxidation of iridium, and thus the potential was reversed at to prevent surface oxidation. Figure 4.1b shows the SEM image of the deposited Ir nanoparticles on GC. It is evident that the structure, as well as the size of the particles is not uniform. Nevertheless, it shows that −1.6 V is a sufficient overpotential for nucleation.

Thus, a nucleation potential of −1.6 V was included into the SWP scheme in Figure 3.1 and then increased systematically to −1.1 V vs. SCE. The SEM images of the deposited particles are shown in Figure 4.2.

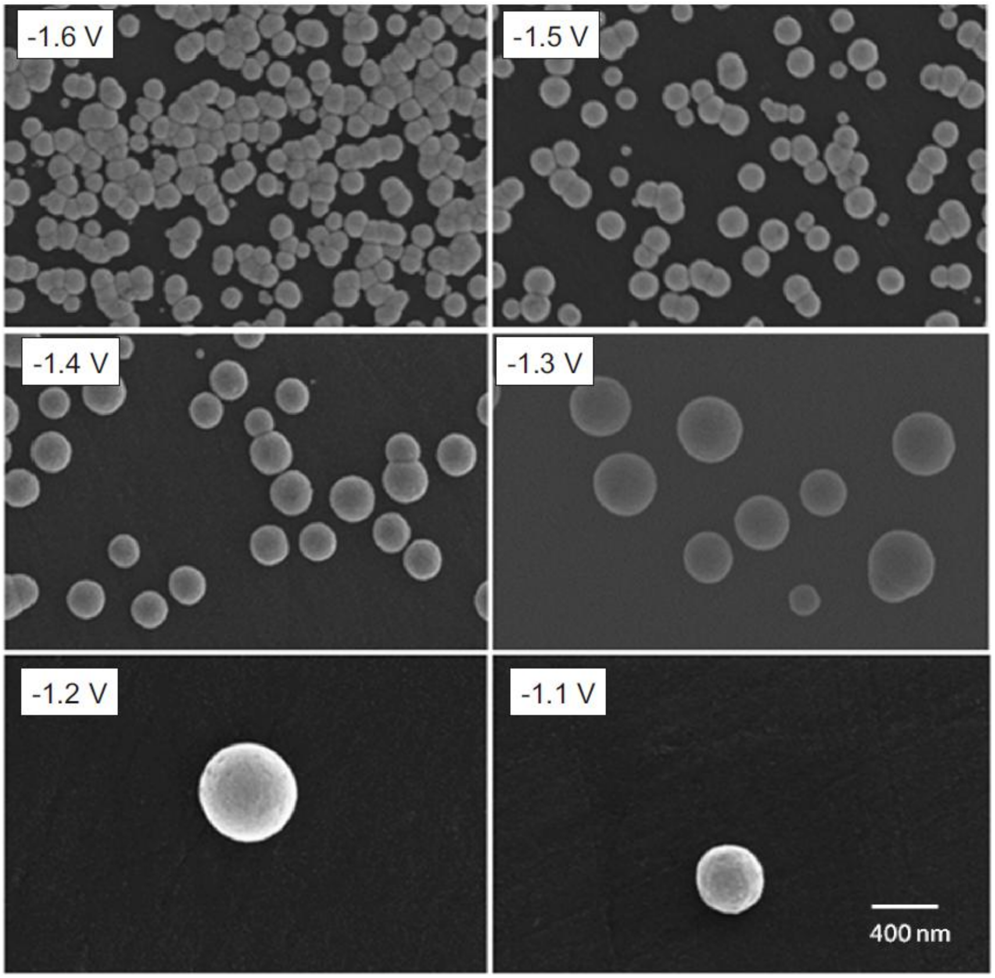

Figure 4.2 Influence of E_n on particle size and density. Reprinted by permission from Springer Customer Service Centre GmbH: Springer US, Electrocatalysis, Electrochemical Fabrication of Well-Defined Spherical Iridium Nanoparticles and Electrocatalytic Activity towards Carbon Monoxide Adlayer Oxidation by Sheasha et al. © Springer Science + Business Media New York 2015

The SEM images show two strong dependencies on nucleation potential. Not only is the particle size larger with more positive nucleation potentials, but on the other hand, the number of deposited particles decreases as well.

Such observations for the increase of particle density together with a decrease in particle size at more negative nucleation potentials are in line with a study on silver nanoparticles, where a similar nucleation method was performed[66]. This is because nucleation occurs faster at more negative potentials and the interdependent growth is larger, due to the overlapping of diffusion zones. Hence, a slight increase in polydispersity would be expected. However, due to the rapid increase in particle density, there is a limited increase in size for each particle, resulting in an overall decrease in average size[66]. This effect is also clearly seen in the voltammograms of each of the samples. The voltammograms of the different samples in 0.1 m H_2SO_4 at 50 mV s^{-1}, as well as the dependence of average particle size and the logarithm of average particle density on nucleation potential are shown in Figure 4.3.

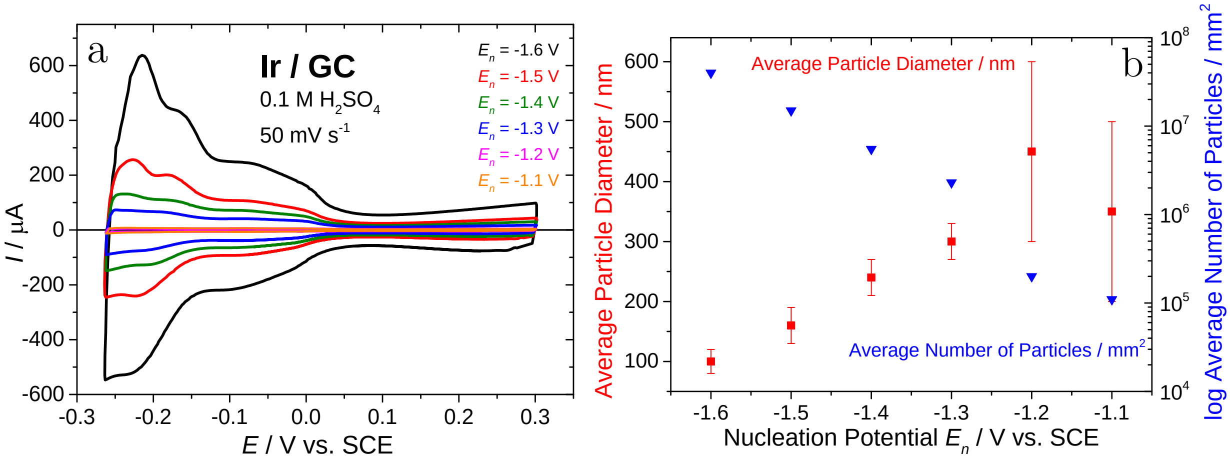

Figure 4.3 (a) Current–potential curves of the Ir nanoparticles, deposited on a GC electrode via the SWP technique at different values of E_n, in 0.1 M H_2SO_4 at 50 mV s^{-1}, (b) Particle size and density as a function of E_n. Adapted by permission from Springer Customer Service Centre GmbH: Springer US, Electrocatalysis, Electrochemical Fabrication of Well-Defined Spherical Iridium Nanoparticles and Electrocatalytic Activity towards Carbon Monoxide Adlayer Oxidation by Sheasha et al. © Springer Science + Business Media New York 2015

The current-potential curves in Figure 4.3a show a decrease in hydrogen adsorption currents with increasing nucleation potentials. This is due to the decrease in number of particles, as highlighted in Figure 4.3b. The standard deviation (SD) of the particle size is plotted as error bars, showing that at $E_n < -1.3$ V vs. SCE the measured particle size maintains no statistical reliability, due to the scarcity of particles on the surface, which is evident from voltammograms as well. Hence, a nucleation potential of −1.3 V vs. SCE was used to obtain large iridium spheres, with a good dispersion and statistical relevance.

4.1.2 The influence of SWP duration on size

Increasing particle size by increasing the duration of the SWP was also investigated, at a fixed nucleation potential. For this study, the previously chosen nucleation potential of −1.3 V vs. SCE was fixed and the SWP was run for 2 hours. The results are shown in comparison to the standard SWP duration of 1 hour in Figure 4.4.

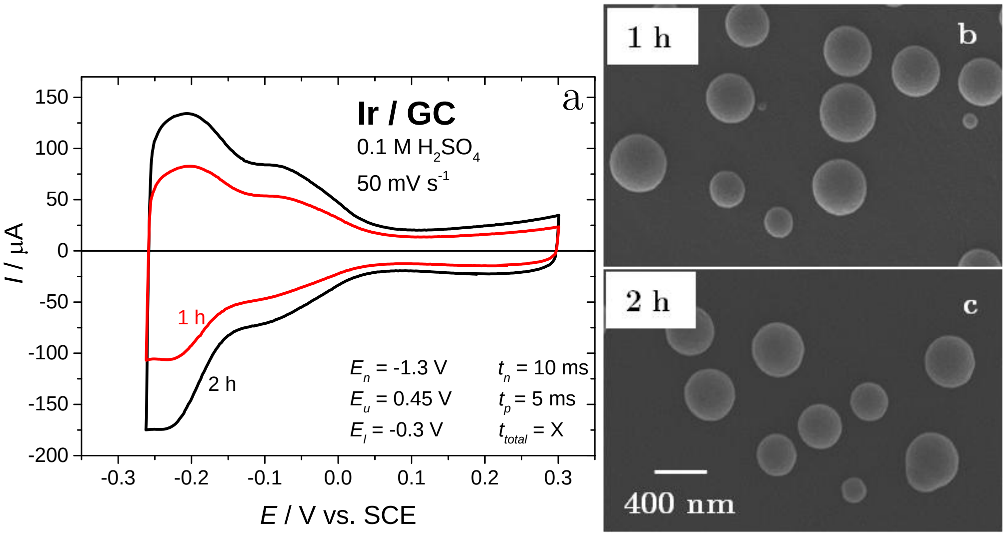

Figure 4.4 (a) Current–potential curves of the Ir nanoparticles, deposited on a GC electrode via the SWP technique for 1 hour (red) and 2 hours (black), in 0.1 M H_2SO_4 at 50 mV s^{-1}, (b), (c) SEM images of the particles deposited for 1 hour and 2 hours, respectively. Adapted by permission from Springer Customer Service Centre GmbH: Springer US, Electrocatalysis, Electrochemical Fabrication of Well-Defined Spherical Iridium Nanoparticles and Electrocatalytic Activity towards Carbon Monoxide Adlayer Oxidation by Sheasha et al. © Springer Science + Business Media New York 2015

The current-potential curves in Figure 4.4a show an increase in hydrogen adsorption currents with an increase in SWP duration. This means that for the same particle density, which would be expected since the nucleation parameters were identical in both cases, a higher iridium loading is present on the surface. This can thus be translated to an increase in particle size, as shown in the SEM images in Figure 4.4b. A 1.7 times increase in electrochemically active surface area (EASA) would be expected because of the observed 1.3 times increase in average particle diameter. This is in very good agreement with the calculated factor of increase in hydrogen adsorption charge, which is around 1.6.

4.1.3 Probing the surface with CO adlayer oxidation

CO adlayer oxidation was used to investigate the effects of particle size and surface morphology on the electrocatalytic activity of the particles, in terms of peak potential. Particles were prepared at with different sizes; 100 nm, 200 nm, 290 nm, and 370 nm. Figure 4.5 shows SEM images of the particles, as well as the oxidation curves for each of them.

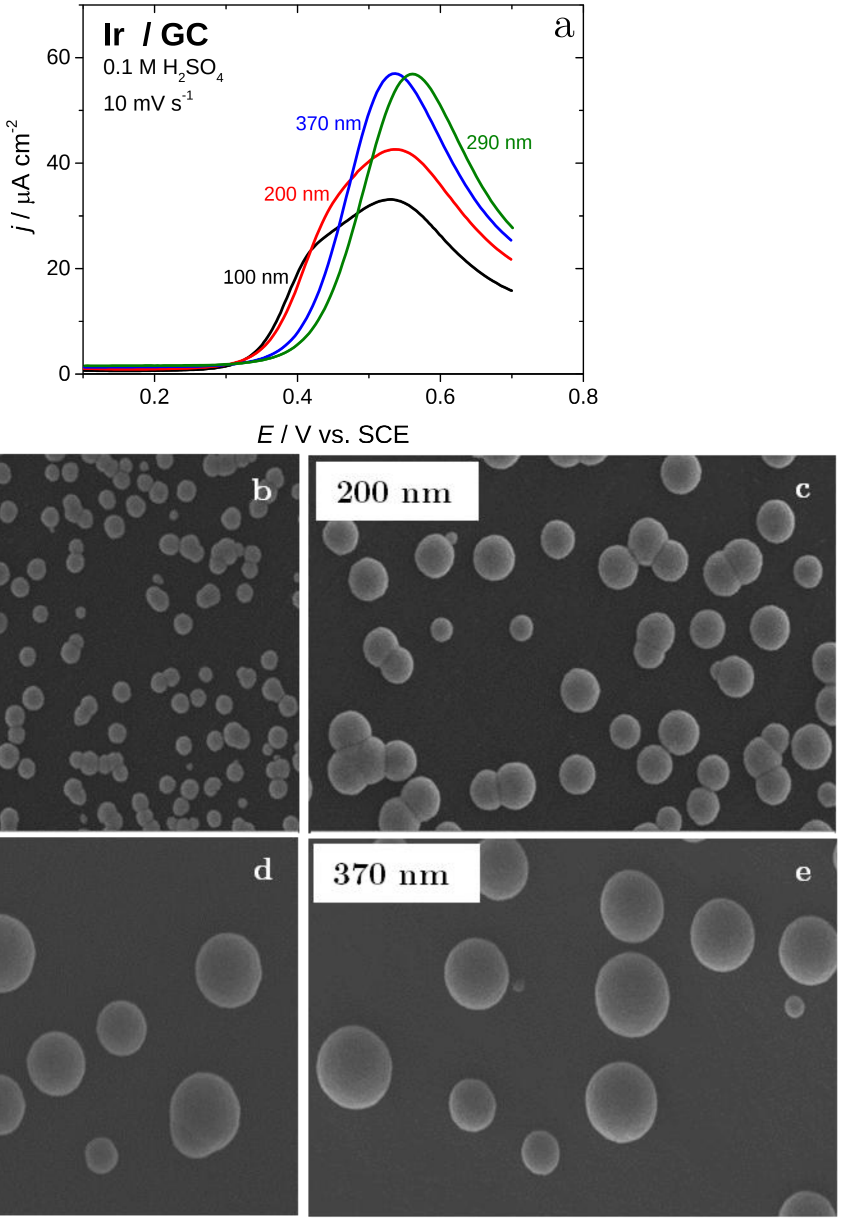

Figure 4.5[38] **(a) Current–potential curves for carbon monoxide adlayer oxidation on Ir particles with different sizes deposited on GC, in 0.1 M H_2SO_4 at 10 mV s^{-1}, (b), (c), (d), (e) SEM images of Ir nanospheres with average diameters of 100 nm, 200 nm, 290 nm, and 370 nm, respectively.** Adapted by permission from Springer Customer Service Centre GmbH: Springer US, Electrocatalysis, Electrochemical Fabrication of Well-Defined Spherical Iridium Nanoparticles and Electrocatalytic Activity towards Carbon Monoxide Adlayer Oxidation by Sheasha et al. © Springer Science + Business Media New York 2015

The results show that there is no significant shift in peak potential, in relation to particle size. Smaller particles show a broader peak, with a pre-oxidation hump. This could be either due to the non-homogeneity of the spherical structure of smaller particles, or due to the presence of some agglomerates at the higher nucleation overpotentials. On the other hand, the larger particles display a higher oxidation current, due to the narrower oxidation peak.

Next, the sample with the largest particle size was subjected to potential cycles between −0.3 V and 0.7 V vs. SCE, in 0.1 M H_2SO_4 at 50 mV s^{-1}, for 1 hour. This resulted in a roughening of the surface of the iridium spheres. After that, CO adlayer oxidation was performed with the roughened particles. The resulting oxidation curves are shown in Figure 4.6a, and the induced surface change could be seen in Figures 4.6b and the as-prepared sphere in 4.6c.

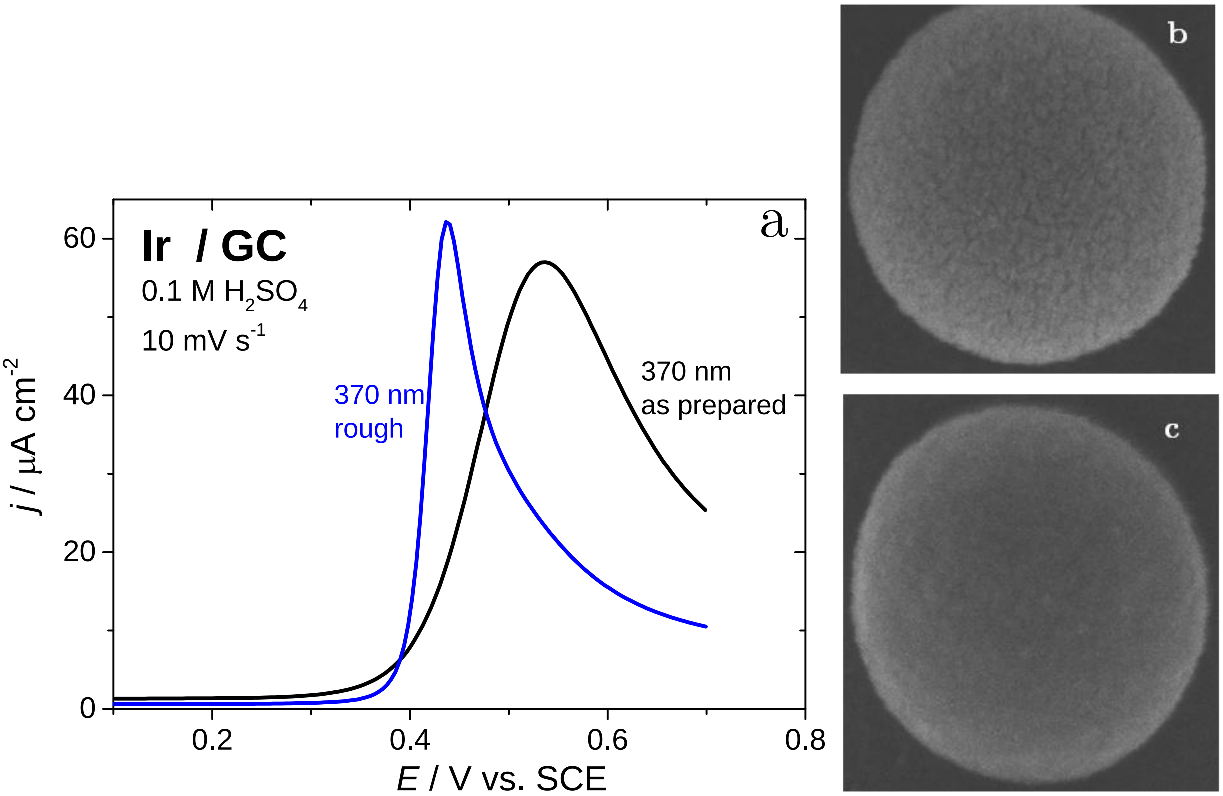

Figure 4.6[38] **(a) Current–potential curves for carbon monoxide adlayer oxidation on Ir particles with an average diameter of 370 nm but different surface morphologies deposited on GC, in 0.1 M H_2SO_4 at 10 mV s^{-1}, (b), (c) SEM images of rough and as prepared particles, respectively.** Adapted by permission from Springer Customer Service Centre GmbH: Springer US, Electrocatalysis, Electrochemical Fabrication of Well-Defined Spherical Iridium Nanoparticles and Electrocatalytic Activity towards Carbon Monoxide Adlayer Oxidation by Sheasha et al. © Springer Science + Business Media New York 2015

The curves show a large shift towards lower overpotentials, and hence a higher electrocatalytic activity, for the oxidation of CO in the case of the rough particles. Due to the roughening by potential cycling, an enrichment of oxygen species on the surface of the particles at lower potentials could occur, which is the main requirement for CO adlayer oxidation[9]. Moreover, there might be residual surface oxides contributing to the enhanced activity. In fact, the rougher particles are more active towards CO adlayer oxidation than planar Ir(210) single crystal surfaces prepared using inductive heating and cooled in a CO rich atmosphere[9].

4.2 Electrochemical Behavior of Chromium and Chromium Solutions

In this section, the measurements carried out to understand the chromium system are discussed. These could be further classified into three systems; the first investigating the electrochemical behavior of chromium in sulfuric acid using cyclic voltammetry. This was important to determine the potential stability window of metallic chromium in this medium.

The second and third systems involve CV and potentiodynamic deposition of chromium onto GC electrodes from trivalent solutions, and hexavalent solutions, respectively. These two systems when compared with each other revealed the similarities and differences between the industrially pre-dominant hexavalent system and the investigated trivalent one. Moreover, a deposition mechanism is proposed, that explains why these differences occur, based on the experimental results. This was crucial to decide which aspects of the trivalent system needed to be addressed, in order to develop a comparably functional system to hexavalent chromium electrolytes.

4.2.1 Chromium Metal in 0.1 M H_2SO_4

In order to have a more detailed understanding of the redox behavior of Chromium, electrochemical measurements were carried out for polycrystalline Cr in Nitrogen-purged 0.1 M H_2SO_4. Starting at a potential of −0.1 V vs. SCE, where no surface oxidation could be seen, the potential was scanned negatively into the HER region, as shown in Figure 4.7.

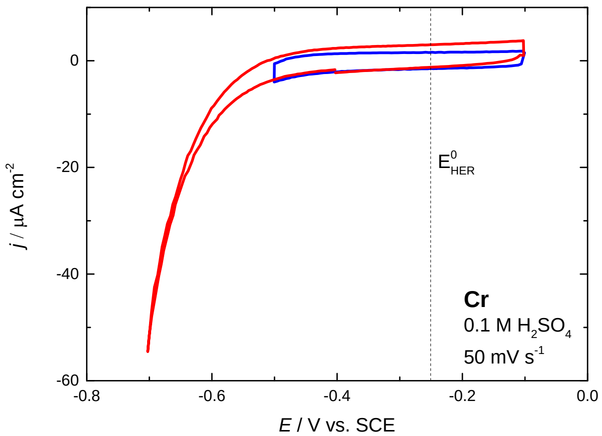

Figure 4.7 Current–potential curves of a massive chromium electrode in 0.1 M H_2SO_4 at 50 mV s^{-1}

In the blue graph in Figure 4.7, no reduction and/or hydrogen evolution peak is seen at −0.5 V, although the standard potential of the HER vs. SCE is at around −0.3 V. Scanning more negatively reveals that the onset of the HER is at around −0.4 V. Within the hydrogen evolution region, it is assumed that the chromium surface is metallic, and there is no indication of reduction of surface oxides. This is later evident as the HER runs in parallel to chromium deposition on GC electrodes.

Based on the voltammetric behavior in Figure 4.7, the negative potential for the window opening experiment was set at −0.6 V vs. SCE, and the potential systematically increased until 1.0 V. Figure 4.8 shows the result of the window opening measurements.

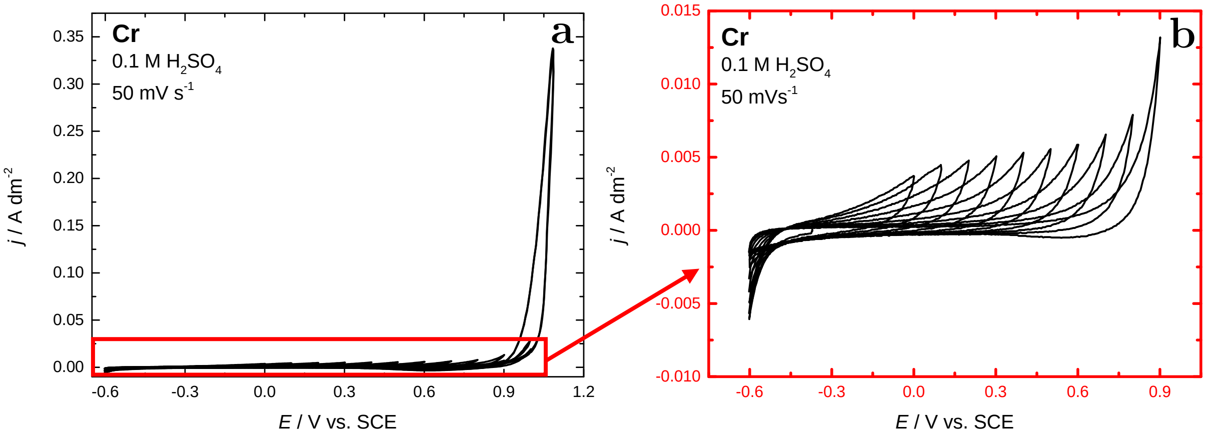

Figure 4.8[35] **(a) Window opening measurement showing bulk oxidation and/or dissolution of a massive chromium electrode 0.1 M H_2SO_4 at 50 mV s^{-1}, (b) surface oxidation region.** Adapted by permission from John Wiley & Sons, Inc.: WILEY-VCH, ChemElectroChem, Potentiodynamic Chromium Deposition from Trivalent and Hexavalent Systems on Glassy Carbon Electrodes: Initial Stages and Mechanistic Insights by Sheasha et al. © 2017 Wiley-VCH Verlag GmbH & Co. KGaA, Weinheim

From these graphs, two distinct regions could be identified. The first region involves the surface oxidation of the chromium disk, which is shown in greater detail in Figure 4.8b. This can be seen from the slight decrease in current of the positive scans with increasing positive potentials, due to incomplete reduction of surface oxides in the negative scan. However, an additional increase in potential to 1.0 V results in an increase in current of over 30 times. This could be related to bulk oxidation or dissolution of chromium. In order to further investigate this behaviour, SEM images of both the polished and the oxidised surface are shown in Figure 4.9, in order to demonstrate the structural differences between both surfaces.

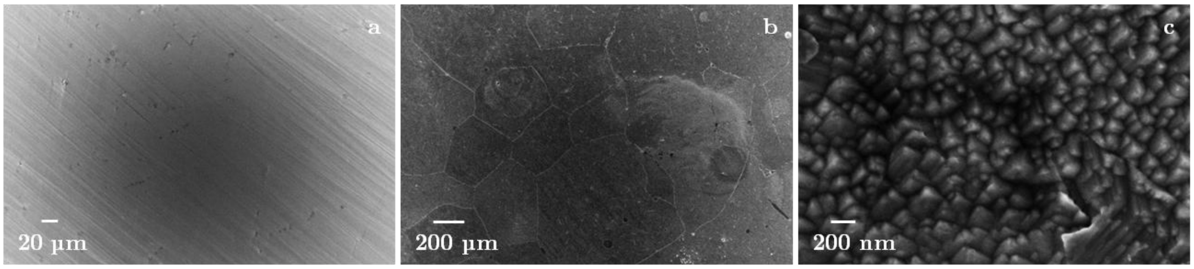

Figure 4.9 (a) SEM image of polished Cr electrode, (b), (c) SEM images of oxidised chromium surface. Adapted by permission from John Wiley & Sons, Inc.: WILEY-VCH, ChemElectroChem, Potentiodynamic Chromium Deposition from Trivalent and Hexavalent Systems on Glassy Carbon Electrodes: Initial Stages and Mechanistic Insights by Sheasha et al. © 2017 Wiley-VCH Verlag GmbH & Co. KGaA, Weinheim

Together with the images, it could be foreseen that deposition below −0.6 V should yield an oxide-free deposit, since oxide reduction and subsequent hydrogen evolution on chromium already occurs in this region. And since the HER overlaps with deposition, HER currents can be used to monitor the growth of the electrodeposited chromium, since an increase in the EASA of chromium will result in an increase in HER currents, which occurs mostly on metallic surfaces rather than on GC.

4.2.2 Potentiodynamic deposition on GC

After understanding the redox behavior of chromium in 0.1 M H_2SO_4, the next step was to try and achieve chromium deposition from chromium (III) on GC, using this base electrolyte with 10 mM $Cr_2(SO_4)_3$ dissolved in it. Since the current state of the art in chromium plating is the use of Cr (VI) compounds, similar measurements were also performed in 0.1 M H_2SO_4 + 10 mM CrO_3. Thus the GC electrode was immersed at −0.1 V vs. SCE and then negatively scanned to −1.4 V. In order to accelerate deposition, the potential was then reversed at −1.0 V, to reduce the hydrogen build up on the surface, while still maintaining a high overpotential for deposition. The potential was cycled between these two values for an hour with a scan rate of 50 mV s^{-1}. Afterwards the GC electrodes were removed and the surface analyzed with SEM. The results are summarized in Figure 4.10.

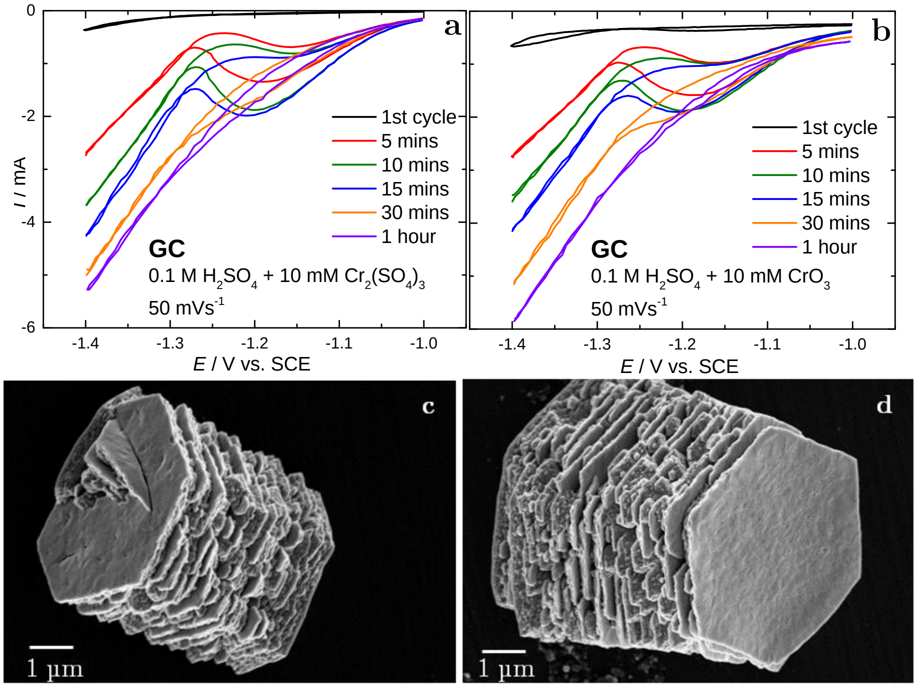

Figure 4.10 Current–potential curves for the potentiodynamic deposition of chromium hydride crystals from (a) trivalent and (b) hexavalent solutions on GC for 1 hour at 50 mV s^{-1} (c), (d) SEM images of the deposited particles from Cr^{3+} and Cr^{6+} solutions, respectively. Adapted by permission from John Wiley & Sons, Inc.: WILEY-VCH, ChemElectroChem, Potentiodynamic Chromium Deposition from Trivalent and Hexavalent Systems on Glassy Carbon Electrodes: Initial Stages and Mechanistic Insights by Sheasha et al. © 2017 Wiley-VCH Verlag GmbH & Co. KGaA, Weinheim

The SEM images show that a very similar particle structure obtained from both systems. Deposits from both systems are well-defined hexagonal crystals, characteristic of *hcp* chromium hydride[86,87]. This crystal structure for chromium has been reported since 1926[88], however, the morphology of such a hydride could not analyzed, since it could not be stabilized as films, which most studies dealt with. Due to the strong hydrogen evolution occurring simultaneously with deposition, atomic hydrogen is incorporated into the lattice, forming chromium hydride particles as shown in Figure 4.10.

The current-potential curves also show a very similar behavior for both systems. As the measurement time increases, the hydrogen evolution current increases, suggesting an increase in the chromium content and EASA on the GC surface. Perhaps, the biggest difference is the significant negative current offset in the Cr(VI) system, in contrast to the Cr(III) system. This negative shift is most likely due to the reduction of Cr^{6+} to Cr^{3+}.

Another important feature is the emergence of a cathodic peak after the first cycle, which then fades away after 30 minutes. This could be due to a positive shift in pH in the electrode vicinity, as a result of the consumption of acidic Cr^{3+} complexes, thus shifting the HER to more negative potentials[28]. Another possibility is the reduction of adsorbed

Cr^{3+} species to Cr^{2+}, which is then reduced to metallic Chromium on the GC surface, reducing the HER efficiency[56]. With increasing chromium content, hydrogen evolution occurs more readily suppressing this effect, and hence the peak fades away.

To further understand the nature of this cathodic peak, potentiodynamic measurements were performed with a higher scan rate of 200 mV s^{-1}. Figure 4.11 shows the current-potential curves of scans at 50 and 200 mV s^{-1}.

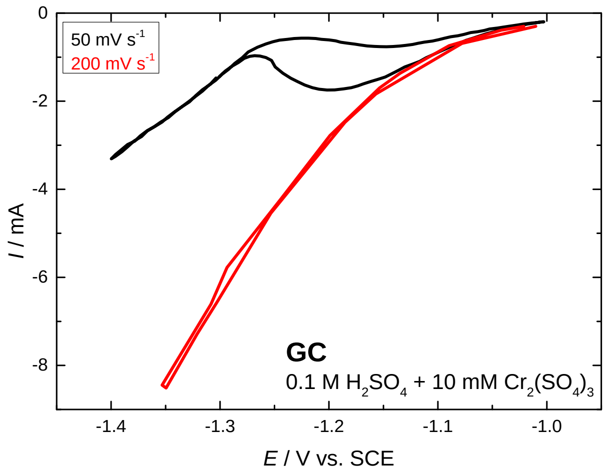

Figure 4.11 Effect of scan rate on potentiodynamic deposition of chromium from a Cr(III) solution on GC. Adapted by permission from John Wiley & Sons, Inc.: WILEY-VCH, ChemElectroChem, Potentiodynamic Chromium Deposition from Trivalent and Hexavalent Systems on Glassy Carbon Electrodes: Initial Stages and Mechanistic Insights by Sheasha et al. © 2017 Wiley-VCH Verlag GmbH & Co. KGaA, Weinheim

The measurements revealed that at 200 mV s^{-1} the peak was no longer present. Instead, hydrogen evolution proceeds directly, and hence the deposition was of a poor quality, in comparison to the original measurement. This observation further strengthens the interpretation that the cathodic peak is related to the reduction of Cr^{3+} complexes on the surface, and that this process requires a longer time than that provided by the higher scan rate.

So far, both systems seem to behave similar to one another from the point of view of the deposited chromium. An increase in cycling time would hence clarify the underlying differences between both systems. This is highlighted by the SEM images in Figure 4.12.

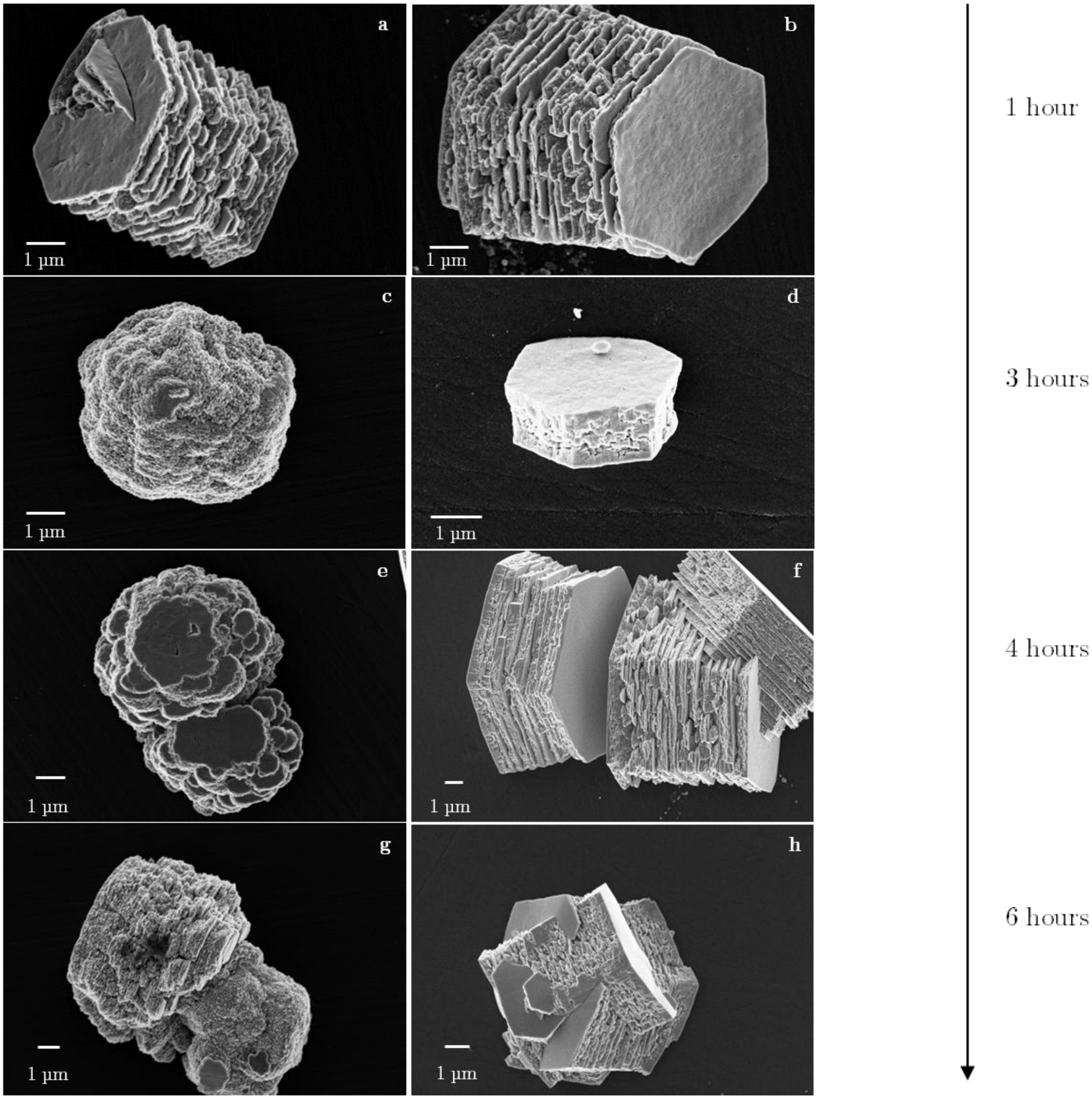

Figure 4.12 SEM images revealing different particle structures on GC after deposition times of (a) 1, (c) 3, (e) 4, and (g) 6 hours from Cr(III) solutions, while (b), (d), (f), (h) represent those changes for the same deposition durations from Cr(VI) solutions. Adapted by permission from John Wiley & Sons, Inc.: WILEY-VCH, ChemElectroChem, Potentiodynamic Chromium Deposition from Trivalent and Hexavalent Systems on Glassy Carbon Electrodes: Initial Stages and Mechanistic Insights by Sheasha et al. © 2017 Wiley-VCH Verlag GmbH & Co. KGaA, Weinheim

The images on the left column show the evolution of particle structure with time for the Cr(III) system, while the right column is for the Cr(VI) system. In the case of the chromium(III) solution, Figures 4.12a, c, e and g show that with longer potential cycling, the hexagonal structure decomposes and the hydrogen escapes from the chromium hydride *hcp* lattice[86], giving rise to more randomly structured chromium particles. This instability could be due to the depletion of trivalent chromium species that are active for deposition in the electrode vicinity. With prolonged deposition, Cr^{2+} builds up close to the GC surface, which, along with the higher pH near he surface, catalyzes the formation of inert oligomers of chromium complexes by olation, whereby metal ions are linked together via OH groups[28]. Thus deposition rate decreases, and hence not enough hydrogen can be included in the lattice to stabilize the *hcp* structures. It was also reported that if the percentage of trivalent chromium decreases below a certain value in solution, the formation of the hexagonal hydride is hindered[89].

On the other hand, Figures 4.12b, d, f and h show that the deposits from Cr(VI) maintain their crystalline *hcp* structure, even with prolonged cycling. This is primarily due to the nature of the Cr^{3+} complexes formed by the reduction of Cr^{6+}, at the surface; chromic dichromate, $Cr_2(Cr_2O_7)_3$. The complexation of Cr(III) ions with dichromate prevents the formation aquo-complexes that are typically formed in Cr(III) solutions[28]. This ensures a continuous supply of Cr^{3+} species that are active for deposition, which can then be reduced to chromium. Since this is always occurring in the presence of hydrogen evolution, hydrogen is being constantly incorporated into the lattice, and the hexagonal hydride is stabilized, independent of cycling time.

4.2.3 Mechanistic Insights

From these findings, a mechanism for hydride formation from both systems could be proposed. This is illustrated in Figure 4.13.

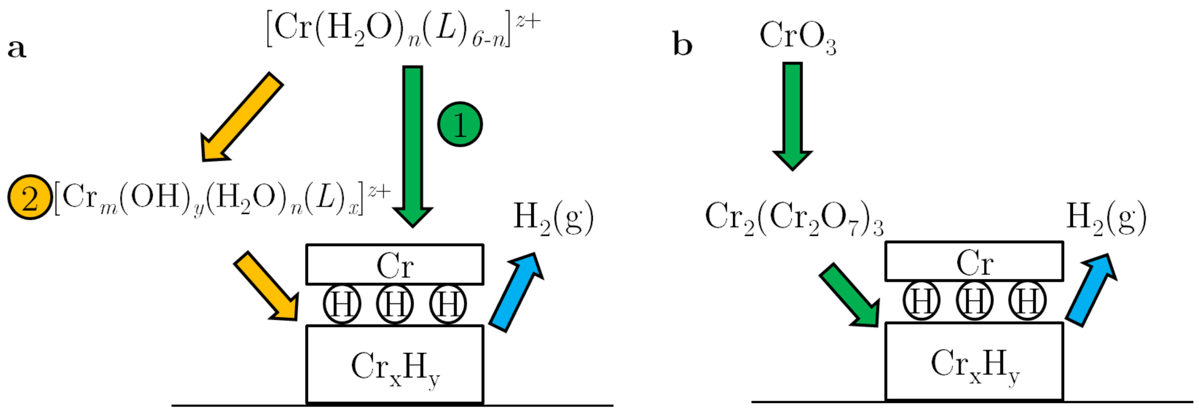

Figure 4.13 Illustrations of proposed mechanisms for chromium hydride deposition from (a) Cr(III) solutions and (b) Cr(VI) solutions. Adapted by permission from John Wiley & Sons, Inc.: WILEY-VCH, ChemElectroChem, Potentiodynamic Chromium Deposition from Trivalent and Hexavalent Systems on Glassy Carbon Electrodes: Initial Stages and Mechanistic Insights by Sheasha et al. © 2017 Wiley-VCH Verlag GmbH & Co. KGaA, Weinheim

Figure 4.13b highlights the deposition mechanism from Cr(VI) electrolytes, in terms of the Cr(III) species formed. There is only one reaction pathway, whereby Cr^{6+} ions are reduced, via Cr^{5+} and Cr^{4+} intermediates, to chromic dichromate, which is then reduced at the surface to chromium hydride, as explained earlier.

Figure 4.13a describes a more complicated mechanism associated with the deposition of chromium from the investigated Cr(III) system. With a solution pH of 1, it is assumed that a $[Cr(H_2O)_n(L)_{6-n}]^{z+}$ ion is predominant in solution, where L could be a bisulphate or hydroxide ligand. During deposition, however, the exact composition of the Cr^{3+} species close to the GC surface cannot be determined due to their tendency to from oligomers, or undergo further ligand exchange reactions, particularly due to the higher pH and Cr^{2+} build up near the surface, which would catalyze such reactions[28]. Hence the species close near the surface could be more generally described as $[Cr_m(OH)_y(H_2O)_n(L)_x]^{z+}$, which could be a poly-nuclear chromium molecule with mono- or dihydroxy bridges between the chromium centers, coordinated with water molecules and ligands[54,90–94].

Therefore, it is likely that during the first hour of potential cycling, the reduction of the predominant monomeric species in solution plays the more significant role; deposition follows Pathway 1. As deposition time is increased, Pathway 2 becomes increasingly dominant, since the increasing build up of Cr^{2+} along with the higher local pH during deposition favor the olation of the chromium complexes into poly-nuclear chromium molecules near the surface. These longer chain molecules are more stable and hence the deposition rate quickly decreases with longer cycling times.

Thus, it was evident that in order to develop a new trivalent system, it is essential to have stable, monomeric, chromium(III) species in solution, for a continuous deposition similar to hexavalent systems. By allowing the solution to stand for a long time (more than one month), it was noticed that the solution color changes from green to blue, which was later confirmed to be a slow ligand exchange to achieve the monomeric aquo-complex, $[Cr(H_2O)_6]^{3+}$. This would be the key building block for the newly developed system, which is discussed in detail in Section 4.3.

4.3 Development of a new electrolyte

In this section, the concept behind the newly developed solution will be explained, along with the supporting spectroscopic and electrochemical measurements. In addition, the preparation technique for the novel electrolyte is mentioned and the underlying changes to the Cr(III) complex chemistry discussed.

4.3.1 Electrochemical measurements with aged solutions

In order to be able to deposit films, hydrogen evolution on the surface should be minimized. Hence, the pH was increased to a value of 3, which is a common value for chromium film deposition from trivalent solutions[23], by decreasing the concentration of H_2SO_4. In order to compensate for the change in conductivity and sulfate concentration, 0.1 M Na_2SO_4 was added to the green solution. The pH of the aged blue solution was adjusted using NaOH. The current-potential curves at 15 minutes of deposition as well as SEM images of both systems after a total cycling time of 2 hours are shown in Figure 4.14.

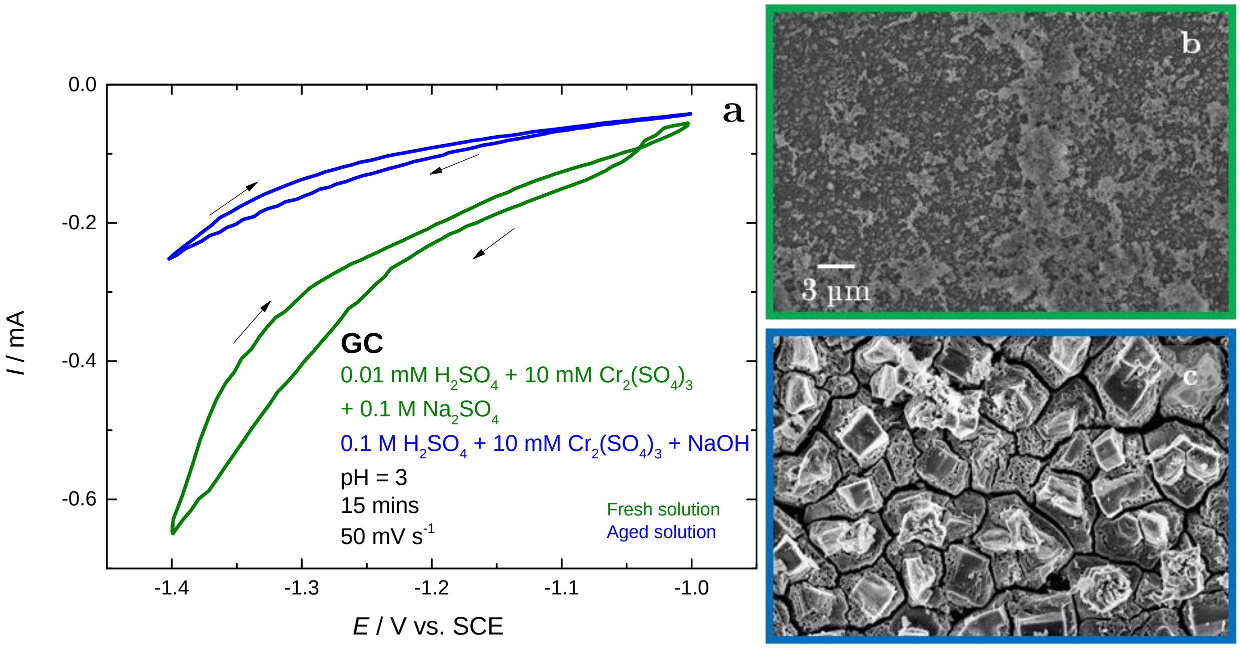

Figure 4.14 (a) Current–potential curves for the potentiodynamic deposition of chromium on GC from a fresh solution (green) and an aged solution (blue) (b) and (c) represent SEM images of the deposits respectively

It is apparent from both the voltammograms as well as the SEM images that the nature of the present chromium(III) species plays a huge role on the quality of the deposit. The deposit from the fresh solution in Figure 4.14b is amorphous, while that from the aged solution (Figure 4.14c) is crystalline, which is also evident from the apparent growth of an incomplete layer on top of the deposit in both cases. Even though by increasing the pH, the HER activity is decreasing, however the currents measured are mainly HER currents. Nonetheless, it can be seen from Figure 4.14a that the HER currents for the aged solution are almost half of that measured for the fresh solution, highlighting a possibly more efficient deposition.

Additionally, since electrodeposition is commonly done with a fixed potential/current, potentiostatic measurements on both systems were carried out, in order to achieve a better understanding of how both systems would behave. Upon systematic investigations, it was found that at −1.3 V vs. SCE, potentiostatic deposition is successful on GC. Hence, Figure 4.15 shows the current transients as well as SEM images for potentiostatic measurements on fresh and aged solutions, at a pH of 3, for 2 hours, at $E = -1.3$ V.

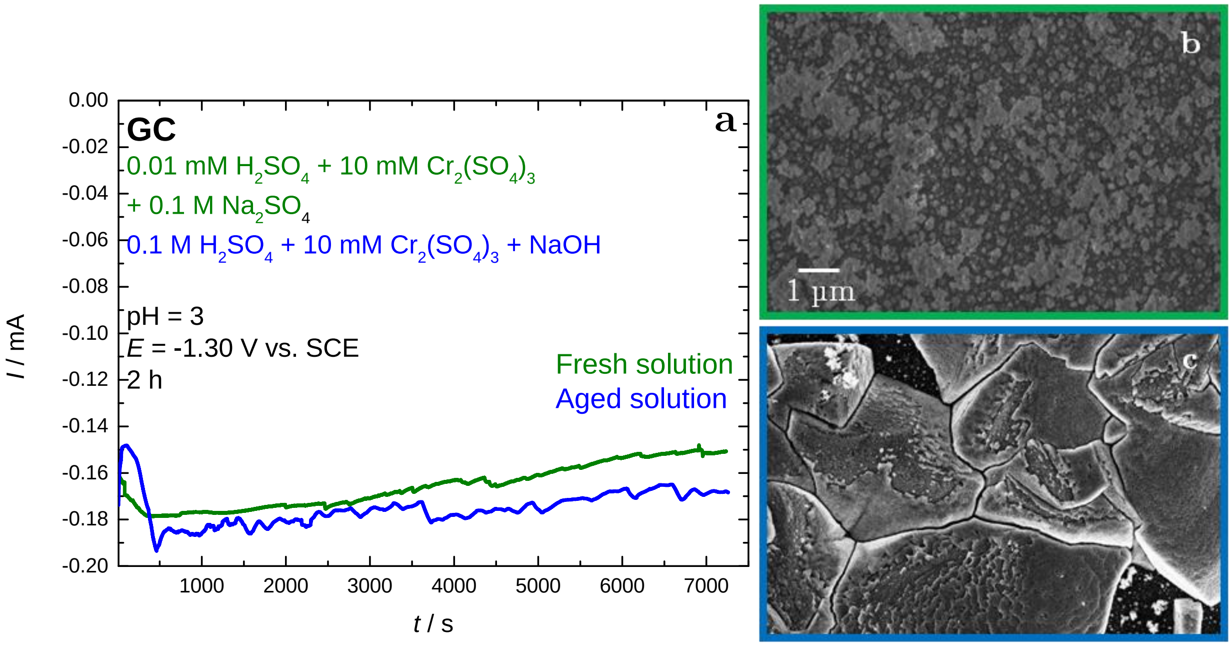

Figure 4.15 (a) Current–time curves for the potentiostatic deposition of chromium on GC from a fresh solution (green) and an aged solution (blue) (b) and (c) represent SEM images of the deposits respectively

While the current transients in Figure 4.15a show a similar behavior, the SEM images in Figures 4.15b and 4.15c are completely different from one another. It is evident that the structure of the deposit from the aged solution consists of large crystalline grains, where a layer-by-layer growth takes place, as seen from the morphology of the crystallites, while that from the fresh solution gives rise to an amorphous film.

4.3.2 Thermal acceleration and up-scaling

Even though the aged system seemed very promising, the extremely long ageing time presented a huge drawback. Thus, the next step was to try and accelerate this process by heating. By heating a solution of 0.1 M H_2SO_4 + 10 mM $Cr_2(SO_4)_3$ for three hours at 100°C, the solution color changed from green to blue. If the pH is then adjusted to 3 by addition of NaOH, similar to the aged solutions, the resulting deposits are similar to those in Figure 4.14c. Hence, this technique was successful to accelerate the formation of the monomeric hexaquo-complexes.

After successfully producing the blue solutions, the next step was to verify if this technique is also possible with higher concentrations. The low chromium(III) concentrations used so far, though ideal to understand the behavior of the system, need to be largely increased to be comparable to other studies/systems. In addition, boric acid, H_3BO_3, was added to the solution. Even though it was later found out that the boric acid does not affect the deposition on GC, however since deposition on metal surfaces, which will be discussed later on, does not happen except in its presence, the addition of boric acid was important for comparability of the results.

Therefore, the chromium concentration was increased to 0.15 mol L^{-1} (10 g/L of Cr^{3+}). In addition, 0.81 mol L^{-1} (50 g/L) of boric acid were added after the preparation of the blue solution, and before adjusting the pH to 3.7. Measurements were also performed with a fresh (green) solution of the same concentration and components. Galvanostatic measurements were carried out in both solutions, with a cathodic current density $j = 5$ A dm^{-2} for 15 minutes. Figure 4.16a shows the structure of the deposit from the fresh solution, while Figure 4.16b shows that from the blue solution.

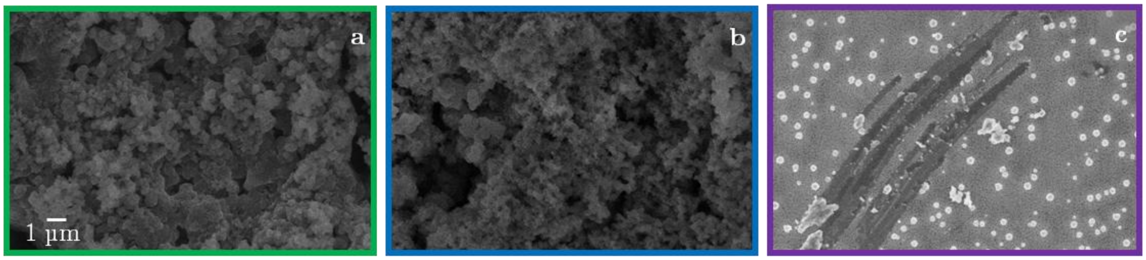

Figure 4.16 SEM images of galvanostatically deposited chromium on GC from (a) a fresh Cr(III) solution, (b) an aged Cr(III) solution (c) a fresh Cr(III) solution complexed with malic acid

The SEM images are very similar, and in both cases chromium hydroxide precipitates were found on the surface. Unlike metallic chromium, this is a light green rough powder, which is responsible for the porous structure seen in Figure 4.16a and b. The formation of the hydroxide is primarily due to the high pH of the solution and the even higher pH at the surface during deposition, which causes olation of the chromium species, and their precipitation as chromium hydroxide. However, underneath these hydroxide precipitates, a thick chromium layer could be seen with the deposit from the blue solution, in contrast to that of the green solution.

To prevent olation and subsequent formation of hydroxides, organic complexing agents are commonly used[28]. In order to demonstrate this effect a fresh solution was complexed with 0.127 mol L^{-1} (17 g/L) of malic acid, by heating the mixture at 65°C for 90 minutes before deposition. This resulted in a color change from green to violet, indicating a successful complexation with malic acid. The result of the deposition is seen in Figure 4.16c, where the porous structures are no longer visible, however the quality of the deposit itself is poor, with different coloration of the film and an inconsistent deposit. This is because the introduction of malic acid to the green solution means the complexation of the pre-existing poly-nuclear chromium molecules, which are themselves difficult to reduce, even if further olation is prevented by complexation with malic acid.

Therefore, in order to develop a new system combining the deposition readiness of the blue solution and the elimination of hydroxides by organic complexation, the chromium hexaquo-complex monomers need to be further complexed with an organic complexing agent, to combine the advantages of both systems.

4.3.3 Designing the new solution

Taking all this into consideration, the composition of the new system would be as follows: 1 M H_2SO_4 + 0.15 M Cr^{3+} + 0.125 M $C_4H_6O_5$ + 0.8 M H_3BO_3 + NaOH. The components are not mixed together at once, but rather as shown in Figure 4.17.

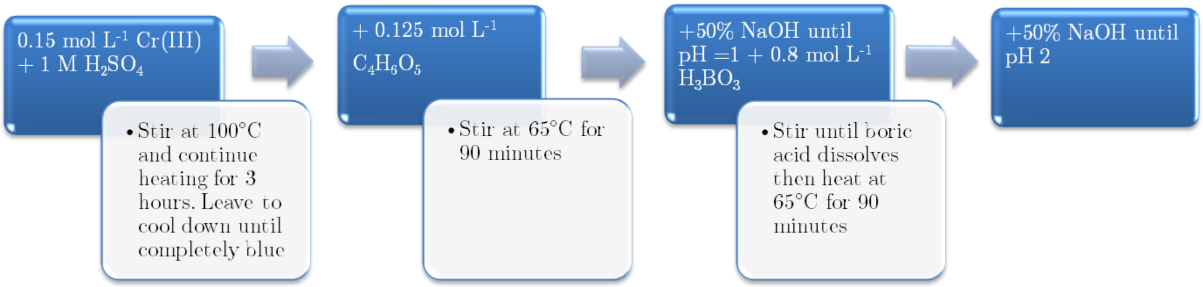
0.15 mol L^{-1} Cr(III) + 1 M H_2SO_4
Stir at 100°C and continue heating for 3 hours. Leave to cool down until completely blue
+ 0.125 mol L^{-1} $C_4H_6O_5$
Stir at 65°C for 90 minutes
+50% NaOH until pH =1 + 0.8 mol L^{-1} H_3BO_3
Stir until boric acid dissolves then heat at 65°C for 90 minutes
+50% NaOH until pH 2

Figure 4.17 Schematic of process required to prepare the new solution

The increase in concentration of H_2SO_4 serves many purposes. During the first stage, the pH is lowered to 0, and thus the formation of hexaquo-complex monomer by heating at 100°C occurs more readily. It also increases the bath conductivity, so that no extra conducting salts need to be added, thus keeping the system as simple as possible. Moreover, it acts as a very good pH buffer in the optimum bath operating pH of between 1.7 and 2, thus no additional buffering agent is required.

The amount of chromium is described as 0.15 M Cr^{3+}, because two different chromium(III) salts were investigated, $Cr_2(SO_4)_3$ and $Cr(OH)(SO_4)$, the latter, basic chromium sulfate, being investigated due to its popularity in the research and industrial fields as a chromium salt for galvanic purposes[95]. For the sake of the UV-VIS spectroscopy study, the solutions were prepared with the basic chromium sulfate. However, the behavior is identical for chromium(III) sulfate.

Before discussing the changes in the nature of chromium complexes due to the aforementioned preparation technique, the spectra of $Cr(OH)(SO_4)$ in 1 M H_2SO_4 and in water were compared to see if there already a difference is to be noticed, even though to the eye both solutions have a deep green color. The spectra are shown in Figure 4.18.

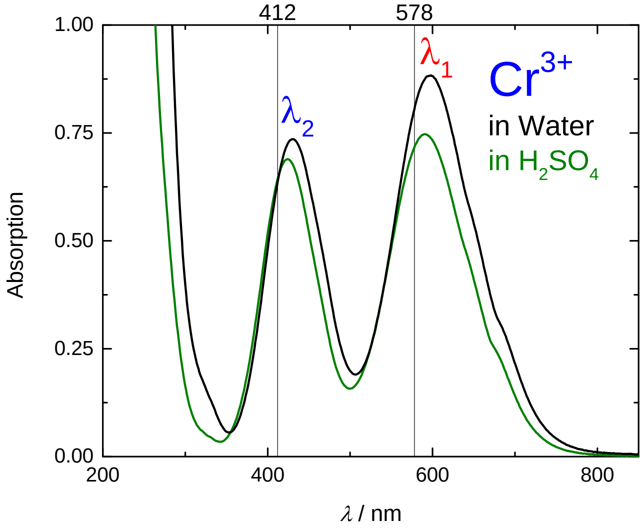

Figure 4.18 UV-VIS absorption spectra of basic chromium sulfate dissolved in water (black) and sulfuric acid (green)

In the spectra of the two solutions, however, differences are quite evident. The smaller wavelengths for the recognizable *d-d* transitions (λ_1 and λ_2) in an acidic environment signal a reduction in ligand field splitting. This can be attributed to the fact that in 1 M H_2SO_4, the pre-existing hydroxide ligand in the $Cr(OH)(SO_4)$ salt is converted by protonation into a water ligand or exchanged for a water molecule. Since water splits the octahedral field more strongly than hydroxide[20], the absorption shifts to higher excitation energies and thus to shorter wavelengths. In addition, the lowering of the pH affects the environment of the complex; chromium complexes tend to oligomerize at higher pH values. Therefore, acidification shifts the equilibrium very much towards the monomer, supporting the earlier hypothesis that a slow ligand exchange reaction to finally obtain monomers of the hexaquo-complex occurs. Since monomeric chromium complexes require higher excitation energies than dimers, trimers, and oligomers, this process enhances the shift of absorption bands to smaller wavelengths[53]. This also supported by the observation that the peaks shift towards the vertical lines, which are the peak positions of the $[Cr(H_2O)_6]^{3+}$ monomer[96].

Figure 4.19 shows the change in the UV-VIS spectra during the first preparation step.

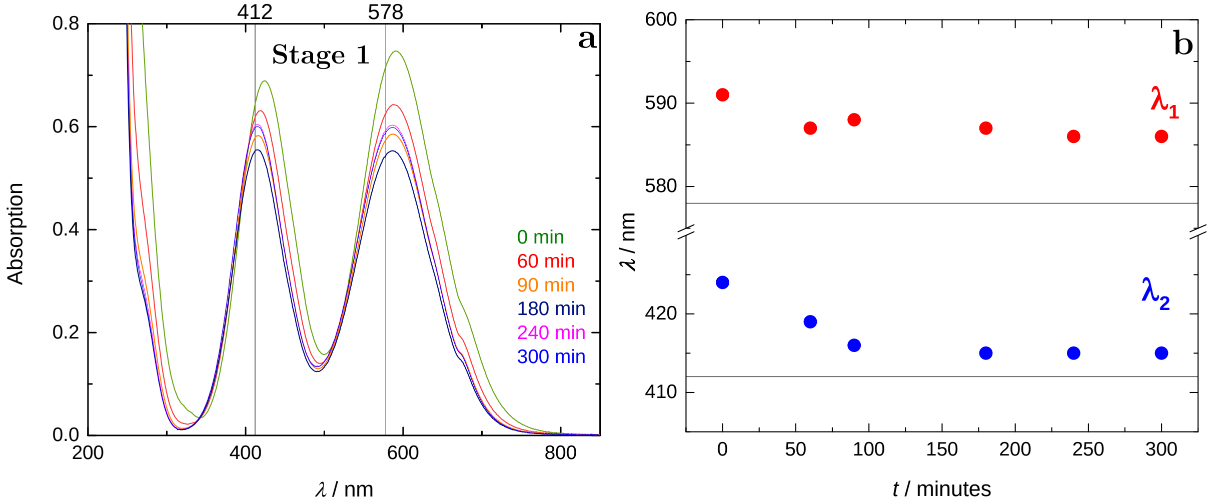

Figure 4.19 (a) Time dependant UV-VIS absorption spectra of the first preparation step (b)change in peak positions during heating as a function of time

Figure 4.19a shows spectra taken at various intervals while the solution is being heated at 100 °C. In 4.19b, the peak positions are plotted vs. heating time, in order to determine how long it is required to heat the solution before reaching equilibrium. Based on these measurements, a heating time of at least 3 hours is required to achieve monomeric hexaquo-complex ions.

Both the shift to higher excitation energies and the blue coloration of the solution strongly suggest an exchange of sulfate with water in the chromium complex. It has been reported that an aquo ligand causes greater ligand field splitting than a sulfate ligand[16], and the observed color change for this ligand exchange, along with the shift in the maximum transmission wavelength between λ_1 and λ_2 to lower values, has also been reported[60].

The ligand exchange reaction is a reversible reaction, which is why the concentration ratio of aquo-complex to sulfate complex depends mainly on the concentration of sulfate in solution:

$$[Cr(H_2O)_5(SO_4)]^+_{(aq)} + H_2O_{(l)} \rightleftharpoons [Cr(H_2O)_6]^{3+}_{(aq)} + SO^{2-}_{4\,(aq)}$$

In order to verify this, an identical solution was prepared, with 1 M perchloric acid, $HClO_4$, where a stronger shift towards the wavelength values of the hexaquo complex monomers after stage 1 would be expected. The differences between both sulfuric acid and perchloric acid systems are highlighted in Figure 4.20.

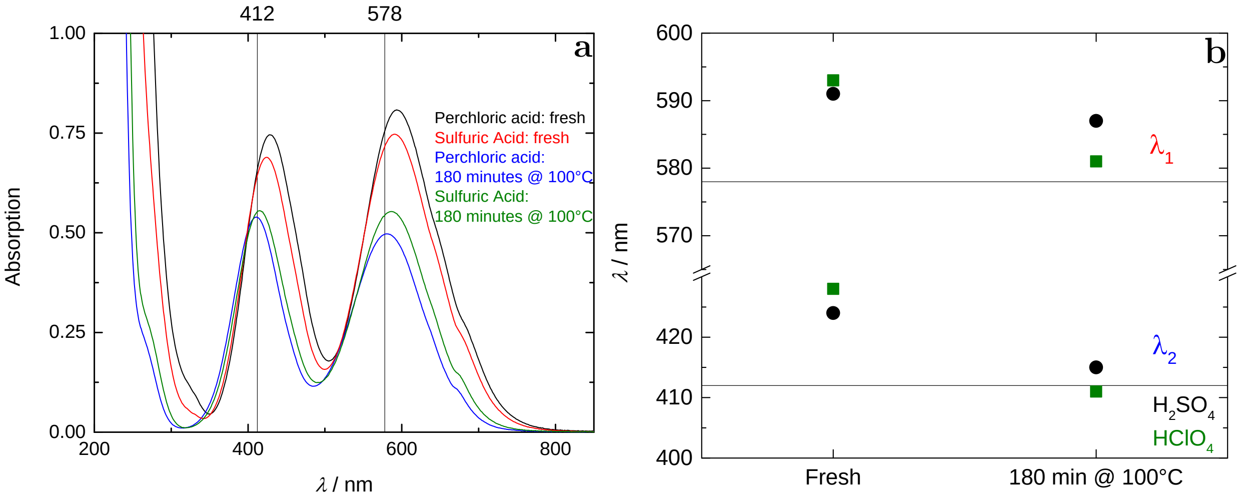

Figure 4.20 (a) Differences in UV-VIS absorption spectra before and after the first preparation step for sulfuric acid and perchloric acid as solvents (b) Peak shifts for both systems

The graphs show that in comparison to the sulfuric acid system, the peaks move closer to the literature values reported for the hexaquo-complex. The much lower sulfate concentration means that the majority of species in solution is the hexaquo-complex, which would be expected to form due to heating at high temperatures, which allows water ligands to replace strongly bound ligands[96].

After successfully obtaining the blue colored solution, consisting primarily of $[Cr(H_2O)_6]^{3+}$, the next step is to further complex the monomers with malic acid. Hence, the malic acid is added to the solution, which is then heated to 65 °C for 90 minutes, to ensure thorough mixing. Even though at the very low pH of 0, it would not be expected that the malic acid dissociates and further complexes the chromium, its presence at such an early stage ensures that along the preparation no olation reactions take place. This was verified by preparing the solution without heating after the addition of malic acid, which lead to similar deposition results.

The addition of NaOH up to adjust the pH to 1 also has very little effect on the UV-VIS spectrum. Only the charge-transfer transition shifts toward longer wavelengths, completely covering the third d-d transition, which is seen in Figure 4.20a as a shoulder at around 300 nm. However, after the boric acid was added, and the solution was heated again for 90 minutes at 65 °C, the spectrum clearly changes. The intensity ratio between both peaks is reversed, with a greater increase in the absorption band at λ_1 than at λ_2. At the same time, λ_1 shifts to a smaller wavelength, and λ_2 to a longer one. This indicates complexation with malic acid. Since malate is a much better ligand than malic acid itself, deprotonation of malic acid is necessary for ligand exchange.

$$C_4H_6O_{5(aq)} \rightleftharpoons C_4H_5O^-_{5(aq)} + H^+_{(aq)}$$

With a *pKa* value of 3.4[59], the equilibrium at pH 1 is strongly shifted towards the acid. Therefore, the complexation takes place only to a small extent, especially since the ligand exchange is thermodynamically favored but kinetically hindered.

$$[Cr(H_2O)_6]^{3+}_{(aq)} + C_4H_5O^-_{5(aq)} \rightleftharpoons [Cr(C_4H_5O_5)(H_2O)_5]^{2+}_{(aq)} + H_2O_{(l)}$$

Heating allows overcoming of the activation barrier, and hence the ligand exchange process is more likely to occur, which is confirmed by the change in the UV-VIS spectra for both sulfuric and perchloric acid systems, as seen in Figure 4.21.

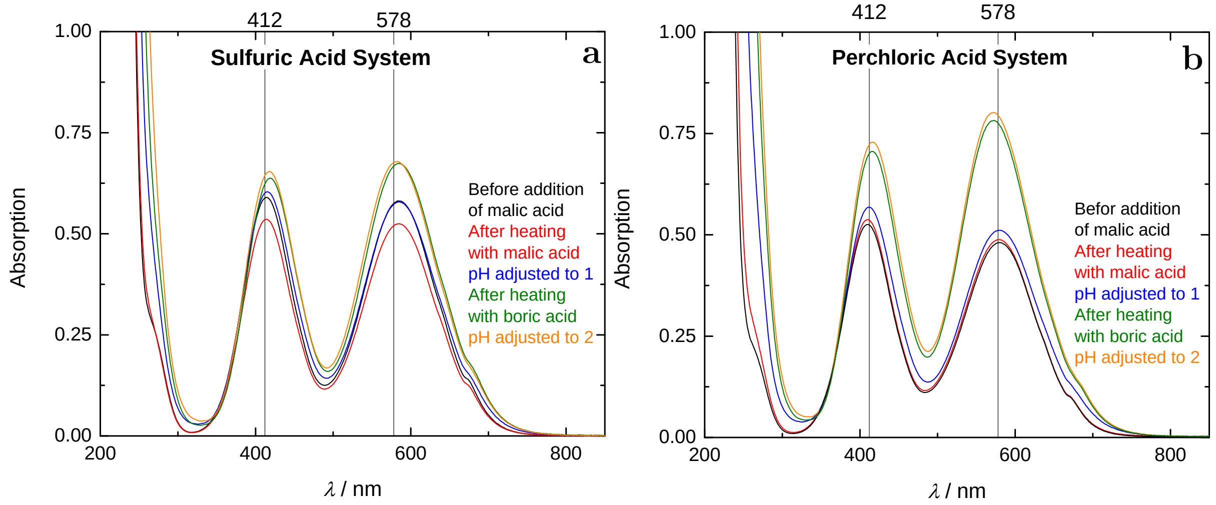

Figure 4.21 UV-VIS absorption spectra for the remaining preparation steps in (a) sulfuric acid and (b) perchloric acid

The presence of boric acid, however, has no effect on the formation of the chromium complex, as comparison spectra for heating without boric acid show. The effect of boric acid on metal deposition is usually attributed to buffering of the solution[17]. However, this is unlikely to be the case, since boric acid has a *pKa* value of 9.27[59], and thus has no buffering capacity in the pH region used. Nonetheless, the presence of boric acid is essential not only for chromium deposition, but also for many other transition metals[14].

In comparison to the sulfuric acid system, only a few differences in the spectroscopy of the perchloric acid system in Figure 4.21b, indicating that the sulfate concentration has negligible influence on the resulting complex in solution after the preparation is complete.

Starting from already lower values for λ_1 and λ_2, the shifts are smaller than those of the sulfuric acid system. This can be due to the lower proportion of complexes containing sulfate or hydrogen sulfate as a ligand in the perchloric acid system, which does not change much as the preparation continues. The increase in absorption after heating with boric acid is much larger than that of the sulfuric acid system in Figure 4.21a. The lower sulfate concentration therefore appears to increase the probability of transition upon excitation.

The kinetic stability of the aquo-complex also explains why upon increasing the pH to 2, no spontaneous change in the spectrum despite the equilibrium shift in the malic acid-malate system. However, after an ageing time of one day, a decrease in the wavelength of the first *d-d* transition occurs, while the wavelength of the second transition remains nearly constant. In addition, the absorption values steadily increase. This indicates a continuously increasing concentration of malate-complexed chromium. The very small shift in wavelength is attributed to the similarity in ligand-field splitting between carboxylates and water. In literature, this behavior is mostly documented only for oxalate[97,98], but malate as a dicarboxylic acid anion should show similar spectrochemical properties.

Electrochemical deposition carried out directly after pH adjustment show a chromium hydroxide precipitates on top of a deposited chromium film. Upon ageing the solution for a few days, this effect disappears. Hence, this provides further evidence that a slow ligand exchange process takes place after the final pH adjustment.

To accelerate the ligand exchange process, the solution was heated to 50 ° C. After two and a half hours at this temperature, a significant increase in absorption is evident, especially at λ_1, which continues systematically. The solution changes its color from dark blue to intense violet. Heating at 50 ° C at a pH of 2 thus proves to be a good way to effect a clear ligand exchange. However, the acceleration of the ligand exchange cannot be achieved by very high temperatures. For example, when the solution is heated to 100 °C, the electrolyte loses the violet tint and returns to the blue color of the aquo-complex.

Since the deprotonation of the second acid group of the 2-hydroxybutanedioic acid (malic acid) has a *pKa* of 5.11[59], it should occur only at significantly higher pH values than the present one. Hence, the malate should act as a single negatively charged ligand. Thus, a bridging of two chromium centers by a malate ligand with two complexing carboxyl groups is unlikely. This is consistent with the theoretical calculations, where it was found that monodental coordination of the oxalate ligand for a chromium (III) pentaqua-oxalate complex occurs at a pH of 3[23].

In summary, Table 4.1 lists the relevant steps for preparing monomericly complexed chromium species. Figure 4.22a and b show the changes in λ_1 and λ_2 for the sulfuric and perchloric acid systems along the course of preparation, respectively. In principle, the spectroscopic behavior of the complex in both media is very similar; with the absorption maxima in perchloric acid in comparison to sulfuric acid shifted by a few nanometers to lower wavelengths.

Table 4.1 Summary of preparation stages and details of each stage

Stage	Preparation Details
A	Fresh Solution
B	Heating at 100 °C for 180 minutes
C	Heating with malic acid at 65 °C for 90 minutes
D	pH adjustment to 1
E	Heating with boric acid at 65 °C for 90 minutes
F	pH adjustment to 2
G	Ageing for 1 day at room temperature
H	Ageing at 50 °C for 120 minutes

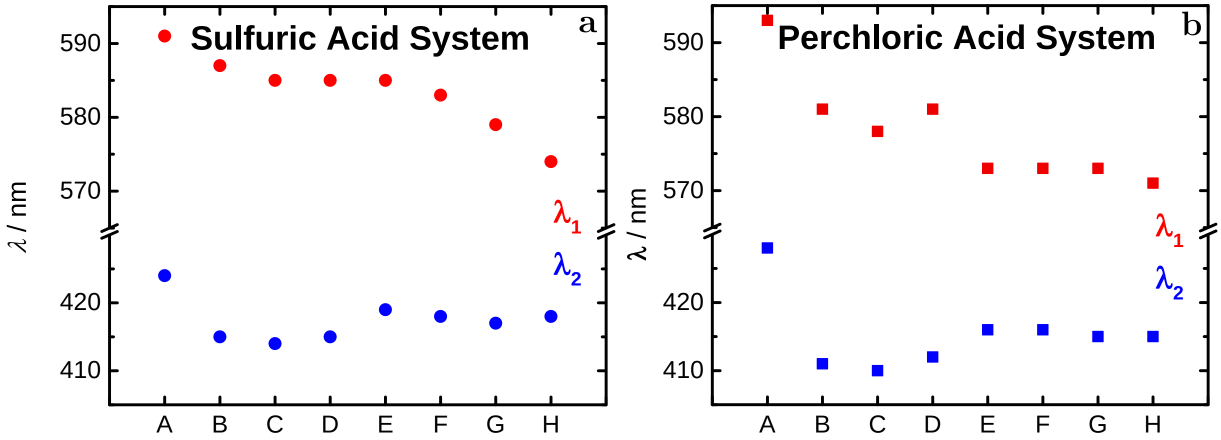

Figure 4.22 Changes in UV-VIS absorption peaks for (a) sulfuric acid system and (b) perchloric acid system

However, these spectroscopic studies can not conclusively clarify whether the sulfate present in the solution influences the complexation or even acts as a ligand in the active Cr(III) complex. The presence of a sulfate or hydrogen sulfate ligand is evidenced by the difference in peak wavelengths between the complexes in the perchloric acid system and the sulfuric acid system. The spectra of the sulfuric acid system show the absorption maxima at higher wavelengths; which indicates the coordination of a spectrochemically weak ligand such as sulfate. However, the difference of 3 nm between both systems after aging is very small.

4.4 Electrochemical deposition from the monomeric complex

Electrochemical deposition measurements were carried out from the newly designed solution, not only to assess the performance of the system, but also as verification that indeed a new species is present in solution, and that the nature of the present species is critical for electrodeposition. While over 1000 measurements were performed to aid in preparation and to understand the system, in this section representative measurements are shown to highlight the plating properties of the new bath.

4.4.1 Electrodeposition on GC

Electrodeposition onto glassy carbon was important to compare the performance of the new system to the previous measurements. Results of galvanostatic deposition at a cathodic current density (j) of 2.5 A dm^{-2} for 30 minutes and 1 hour are shown in Figure 4.23a and b, respectively. Due to the lower pH range, measurements with a similar current density of 5 A dm^{-2} to the measurements in Figure 4.16 were not possible, due to the increased hydrogen evolution. Measurements shorter than 30 minutes yielded very little deposition.

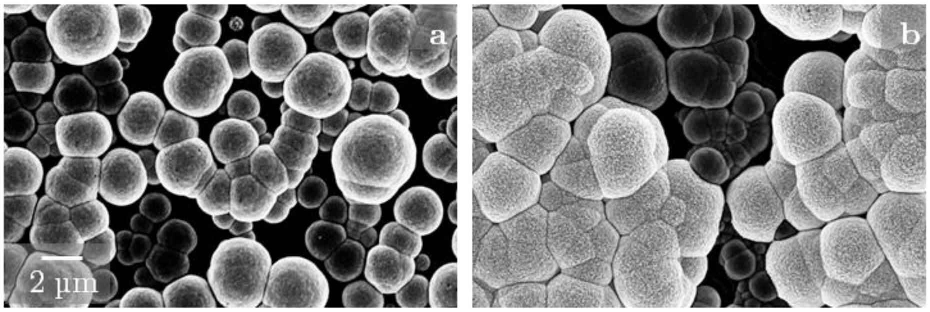

Figure 4.23 SEM images of galvanostatically deposited chromium on GC from the new solution at j = 2.5 A dm^{-2} for (a) 30 minutes and (b) 1 hour

A completely different film structure results from the monomeric complex. Large spherical grains are deposited and the film follows a layer-by-layer growth, which can be seen from the underlying layers in the SEM images.

In order to use higher current densities, galvanic pulsing was employed ($I_U = 0$ A dm^{-2}, $I_L = -5$ A dm^{-2}, $t_T = 30$ minutes, $t_U = t_L = 0.5$ s). For the same parameters, the measurement was also repeated using pulse durations of 0.05 s. However, in order to have a reference to compare to, these measurements were also done in a solution without malic acid. The SEM images for these measurements without malic acid are shown in Figure 4.24a and b, while those with from the monomeric complex in 4.24c and d.

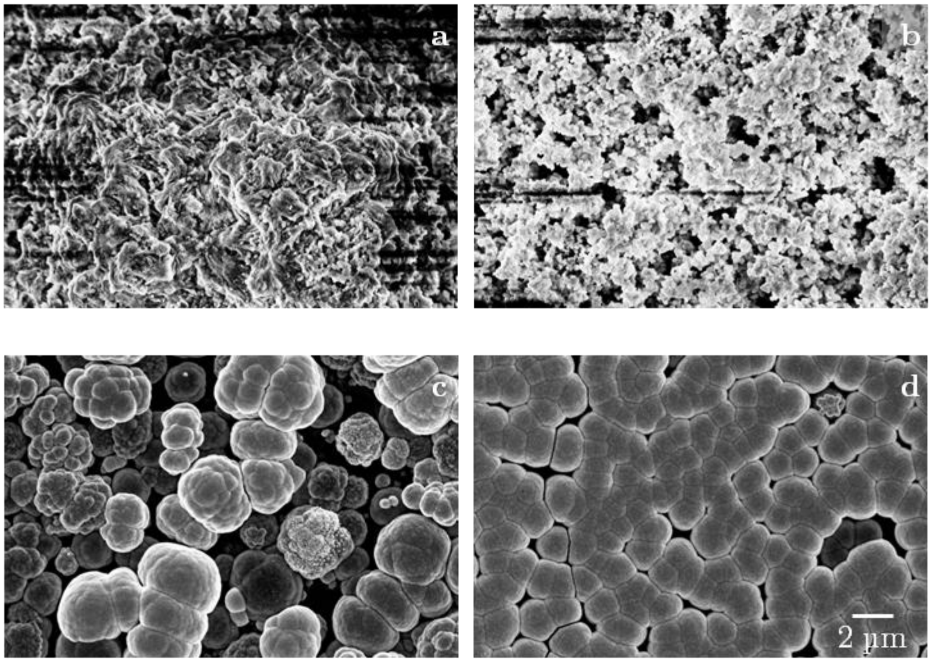

Figure 4.24 SEM images of chromium deposited by galvanic pulsing on GC from (a), (b) non-complexed chromium solution with pulse durations of 0.5 s and 0.05 s, respectively (c), (d) new chromium solution with pulse durations of 0.5 s and 0.05 s, respectively

It is clear from the SEM images that the further complexation with malic acid is vital in order to obtain a well structured deposit. In addition, it seems that a pulse duration of 50 ms is ideal for a uniform layer-by-layer growth of the spherical grains. Moreover, the effect of using a more negative pulse ($I_L = -10$ A dm^{-2}), on the structure of the deposit was investigated. The results in comparison to a similar measurement to 4.24d, are shown in Figure 4.25.

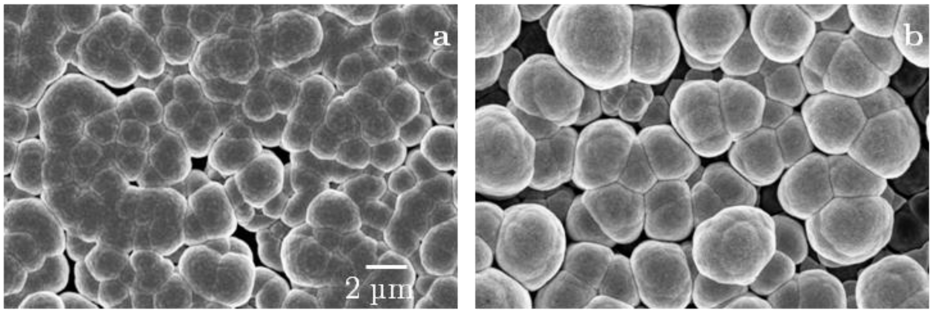

Figure 4.25 SEM images of chromium deposited on G using galvanic pulsing using (a) $I_L = -5$ A dm^{-2} and (b) $I_L = -10$ A dm^{-2}

The images show an increase in particle size, coupled with the increase in cathodic current density. In addition, the particles are less uniform in size and shape than those obtained at $j = -5$ A dm^{-2}. This indicates a lower degree of progressive nucleation with higher cathodic current densities, since stable nuclei are able to form faster and further reduction of chromium ions occurs preferentially on the pre-deposited nuclei.

4.4.2 Electrodeposition on Brass

The use of GC electrodes was vital to the development of the new system, since its utilization as a model electrode allowed for investigating the properties of the solution, with as little substrate interference as possible. However, this is far from practical application. Hence, it was crucial to perform initial measurements on metal surfaces, in order to find out the potential behavior in industrial application.

The common belief in literature and industry is that without the addition of other additives, such as brighteners, whiteners, levelers and wetting agents, very poor or no deposition would occur on metal surfaces. Thus, our aim was to challenge this belief, by investigating the performance of the newly developed system with none of these additives.

Figure 4.26 shows a Hull Cell measurement conducted on brass, where the current density is varied along the sheet, in order to determine the optimum range for current density for galvanostatic measurements.

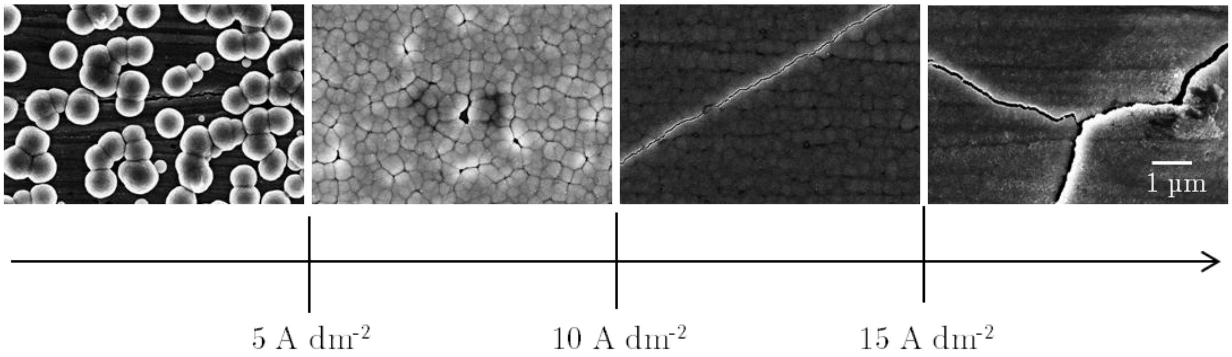

Figure 4.26 SEM images of Hull Cell sample highlighting the microstructure in different current density regions

From Figure 4.26, two important observations could be made. First, the structure of the deposit remains the same; in this case, we also obtain spherical particles. In addition, as the current density increases, the size of the particles decreases, and they tend to form a complete, uniform film. Second, the optimum range of current density could be determined to be between 5 and 15 A dm^{-2}. Below this range, incomplete films are deposited, and above that, the layers start to crack and are broken off the surface by the action of hydrogen.

Using this information, other sample measurements were carried out on brass, some of which are shown in Figure 4.27.

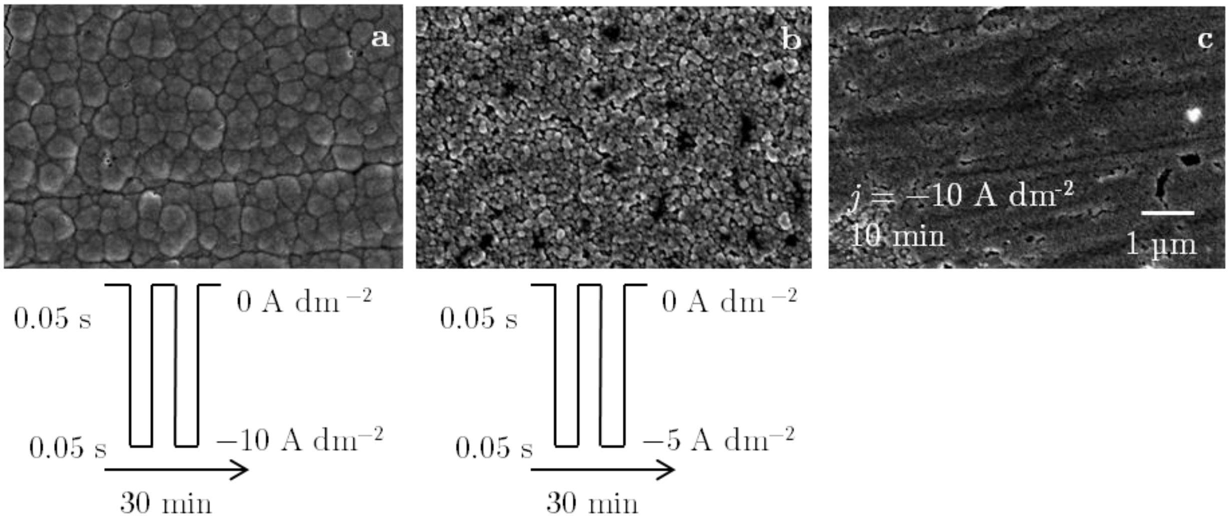

Figure 4.27 (a), (b) **SEM images and galvanic pulsing deposition diagram of chromium deposited on brass at $I_L = -10$ A dm^{-2} and $I_L = -10$ A dm^{-2}, respectively** (c) **SEM image of galvanostatically deposited chromium on brass at $j = -10$ A dm^{-2} for 10 minutes**

The pulsing measurements in Figure 4.27a and b show a similar behavior to the pulsing measurements carried out on GC, in terms of particle size with respect to I_L. However, due to the very large thicknesses deposited, the films would break up, giving a flaky appearance with poor adhesion to the surface.

Galvanostatic deposition, results in a complete film with no addition of additives. While not all the samples of course look identical, however they are quite similar. Photographs of samples repeated with the same parameters are shown in Figure 4.28.

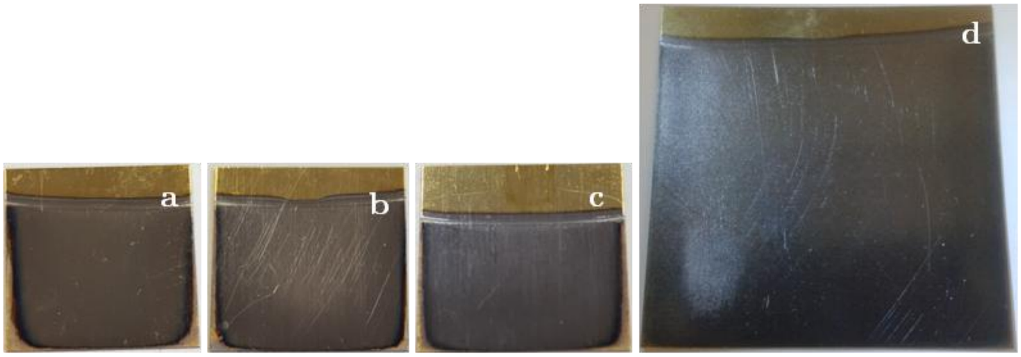

Figure 4.28 Photographs of chromium films deposited on brass sheets with an area of (a), (b), (c)4 cm^2 and (d) 16 cm^2

The films also look identical on larger areas (in this case the area is 4 times larger), as seen in Figure 4.28d. However, the photographs also show that the films are not perfect. Nevertheless, the results show that a complete chromium film can be reproducibly deposited without extra additives. In other words, the newly developed system serves as a fundamental building block, which can be modified by additives, depending on the application, to give the desired outcome, like optical properties and thickness requirements. The part geometry also plays a role in determining the optimum operation parameters.

The pulsing schemes were further optimized to yield higher quality deposits, by modifying the pulse duration and total time. These results are shown in Figure 4.29.

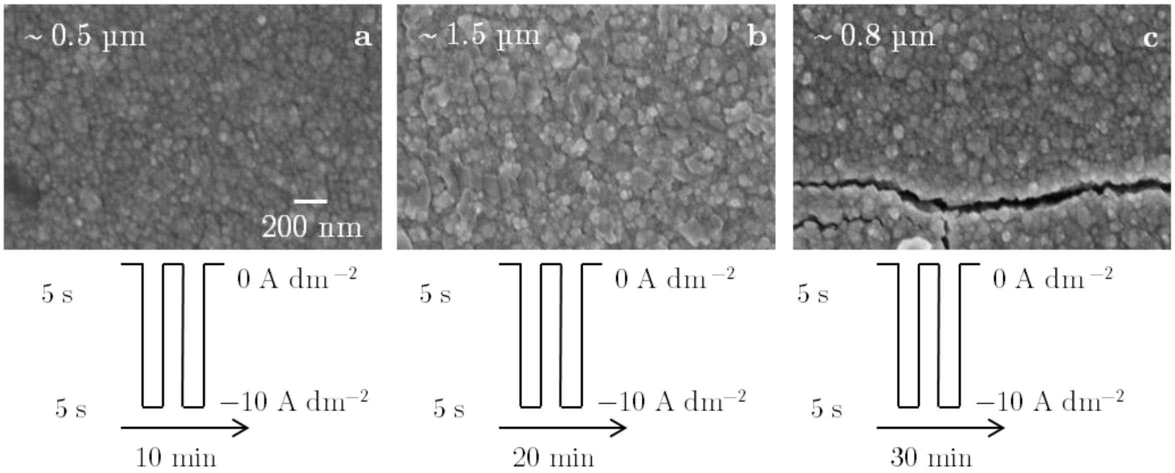

Figure 4.29 SEM images and galvanic pulsing diagrams for chromium deposited on brass for a total pulsing duration of (a) 10 minutes (b) 20 minutes and (c) 30 minutes

The SEM images in Figure 4.29 show that for longer pulse durations the microstructure is more homogeneous. The presence of cracks, like those in Figure 4.29c, is characteristic of thick chromium layers.

4.4.3 Thickness and optical appearance

The optical appearance of the film depends largely on substrate preparation. Figure 4.30 shows a comparison between deposition measurements on an unpolished vs. a polished sample.

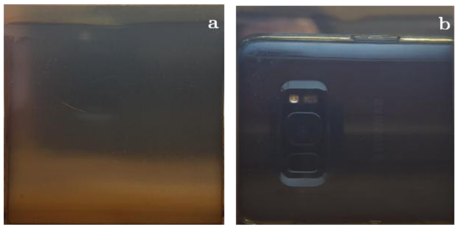

Figure 4.30 Difference in optical appearance between identically deposited chromium films on (a) unpolished and (b) polished brass sheets

Figure 4.30a shows a photograph of chromium deposited on an unpolished brass sheet, while in 4.30b the brass sheet was polished prior to deposition. From the reflection of the camera, it is evident that in order to have the desired mirror-like finish of chromium, especially for decorative purposes, it is necessary to start with a shiny surface. While it is common practice to pre-deposit a nickel film to further enhance the optical appearance, however it was possible to obtain an almost perfect finish on brass.

The effect of deposition temperature on film thickness and color was also investigated. Film color was assessed by measuring the bluish hue of the reflected light, against a preset value. Here, it was essential to understand the microstructural influence on the color of the reflected light. Figure 4.31 shows SEM images of samples deposited at different temperatures, for 5 minutes at $j = -10$ A dm^{-2}.

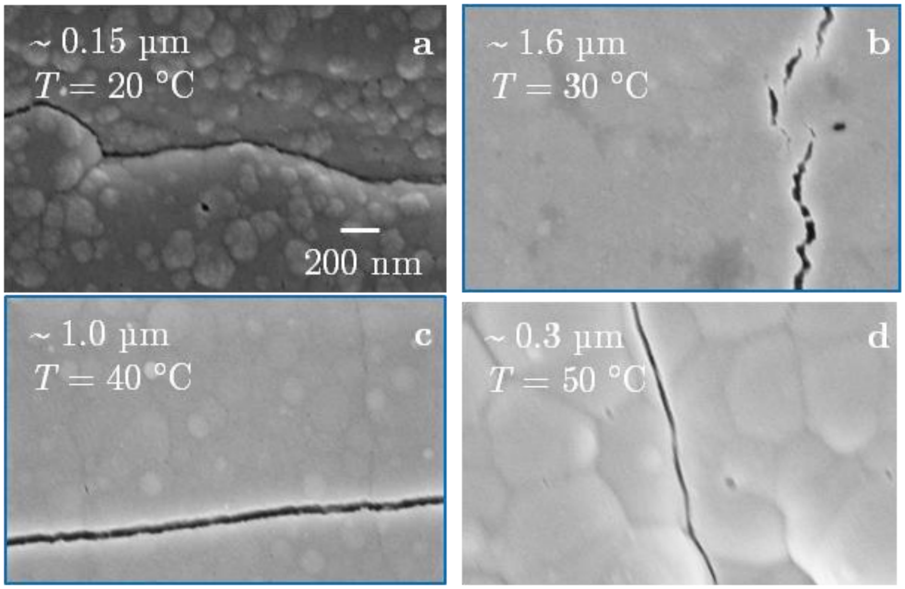

Figure 4.31 SEM images of galvanostatically deposited chromium films on brass for 5 minutes with $j = -10$ A dm^{-2} at temperatures of (a) 20 °C, (b) 30 °C, (c) 40 °C, and (d) 50 °C

The images with a blue border (4.31b and 4.31c) are samples that reflect light with a bluish hue. It can be seen that it is essential to have a very smooth and uniform microstructure in order to obtain the desired optical finish of chromium. The presence of irregularities in the microstructure diffracts light in an undesired way, resulting in reddish or yellowish films. This trend was also seen in many other samples; all the samples that had a similar microstructure to 4.31b and c, reflected a bluish color.

Apart from the color, films are also usually assessed for brightness. This was unfortunately not possible on most of the samples, due to the white haze that could be seen on most of the samples. This was mainly due to large cracks associated with the large thicknesses deposited, which scatter the light in a way that makes the surface seem dull and white, rather than metallic. The cracks are formed due to the volume contraction associated with the decomposition of chromium hydride, which causes strain effects with increasing thickness. These problems are usually solved by additives, which were not used in this work.

Another factor affecting both thickness and optical appearance is the deposition method used. SEM images of a galvanostatically deposited chromium film vs. a film deposited by pulsing are shown in Figure 4.32.

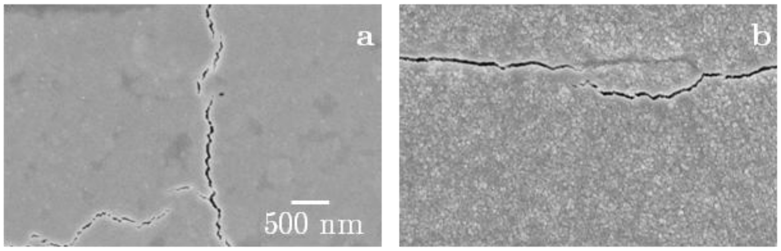

Figure 4.32 SEM images highlighting microstructural differences between (a) galvanostatic deposition and (b) pulse plating of chromium on brass

The resulting microstructure from pulse plating is usually a very rough one, like depicted in Figure 4.32b. This is probably due to the rapid increase in thickness, which prevents a uniform growth of the deposited nuclei to form a homogeneous film.

The relationship between deposition temperature and film thickness, as well as that between deposition technique and film thickness, are plotted in Figure 4.33. These values represent the range of thicknesses which are found at different positions on a sample, for many samples.

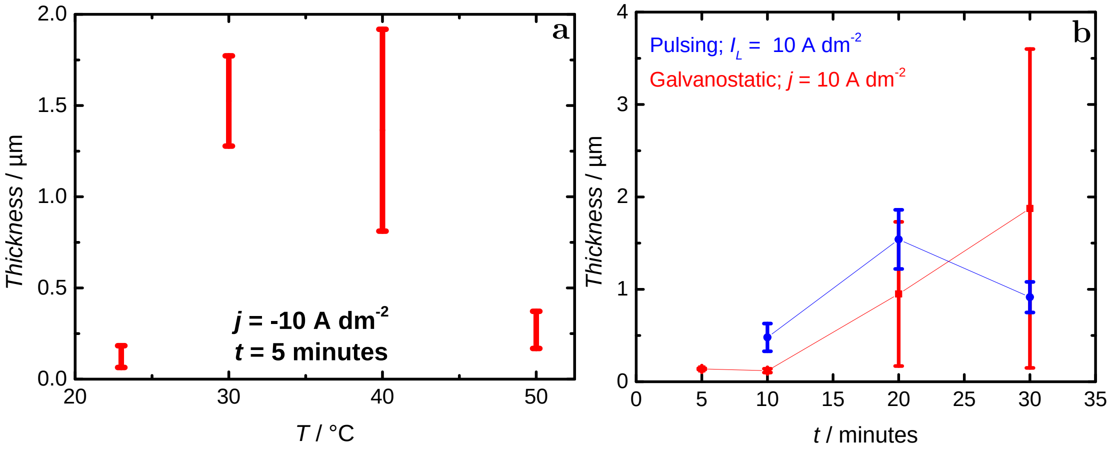

Figure 4.33 (a) Effect of deposition temperature on thickness and (b) relationship between duration and thickness for galvanostatic deposition (red) and galvanic pulse plating (blue)

It can be clearly seen from Figure 4.33a, that the layer thicknesses suddenly increase with an increase in the deposition temperature to 30 °C. Above 40 °C, however, the amount of chromium deposited decreases again. It can be observed that the thick layers at 30 °C and 40 °C are very uneven, as evidenced by the greater variability of the measured values. The deposition at 50 ° C even provides incomplete coverage in some measurements, although the solution gives good results under comparable conditions at lower temperatures.

The decrease in layer thickness at higher temperatures may be associated with the lower overpotential, resulting from the increase in electrolyte conductivity. If the voltage between the anode and cathode is too low, chromium cannot be reduced to the same extent, leading to thinner films. On the other hand, the removal of an aquo ligand is facilitated at higher temperatures, due to stronger molecular vibrations. As a result, the distance between the chromium ion and cathode surface decreases, and therefore the transfer of electrons proceeds much more efficiently. Hence, if more chromium complexes are under coordinated in this way, deposition becomes efficient. These two opposing processes appear to have a trade off between 30 and 40 °C.

Figure 4.33b shows the correlation between thickness, time and deposition technique. In the case of pulse plating, rough layers are formed. Due to the high concentration of chromium complexes that flow to the cathode during the off pulse, a greater supply of chromium ions are available in comparison to galvanostatic deposition, which leads to a fast, efficient, but also irregular film growth. The layer thickness is therefore remarkably high even with short plating times. The decrease in the layer thickness after 20 minutes can be caused by the removal of upper metallic chromium layers due to stress effects caused by hydride decomposition.

For galvanostatic deposition, for short times thinner but homogeneous films are deposited. As the time is increased, certain areas of the film grow while others do not, resulting in the very wide thickness range shown in the graph.

4.4.4 Mechanistic Insights

At the end, it is important to relate all of this information to try to understand the behavior of the system.

As already discussed, the electrolyte is subject to an aging process after the final pH adjustment. Based on the experimental observation that older solutions provide better chromium layers, it was tested whether heating the solution can accelerate this aging. In fact, by heating for a short time, much better results were obtained than would otherwise occur with solutions several days old. The change in the complex was confirmed in the UV-VIS spectroscopy study. It became clear that aging at room temperature over a longer period of time and brief heating of the solution result in a similar change in absorption behavior and thus in the chemical properties of the complex.

After initial attempts to accelerate the aging process by heating at 65 °C, it was experimentally determined that heating for two hours at 50 °C is sufficient to then achieve good deposits. After this step, in most cases, formation of chromium hydroxide due to incomplete complexation could no longer be observed.

Further acceleration attempts by heating the solution more intensively were also tested. However, the results deteriorated significantly after heating to higher temperatures. After heating for 1 hour at 100 °C, the amount of the deposited chromium was greatly reduced. As suggested earlier, boiling the solution leads to a ligand exchange towards the hexaquo complex. Although this step is thermodynamically inhibited, it is made possible with high temperature. Reduction of chromium from the hexaquo-complex is difficult because of the proximity of the aquo ligands to the chromium center, which reduces the amount of deposited chromium[22].

Since the absorption behavior remains constant during heating with malic acid at pH 0, it can be concluded that no ligand exchange takes place in this step. Solutions prepared without this heating step behave in the same way as the electrolytes which were heated after addition of the malic acid in further preparation and in deposition. The assumption that this step has no effect on the dominant complex can thus be confirmed.

Based on these spectroscopic findings, and the electrochemical results, the following mechanism in Figure 4.33 can be proposed. However, it is not possible to determine whether the reactive complex contains a sulfate species or not.

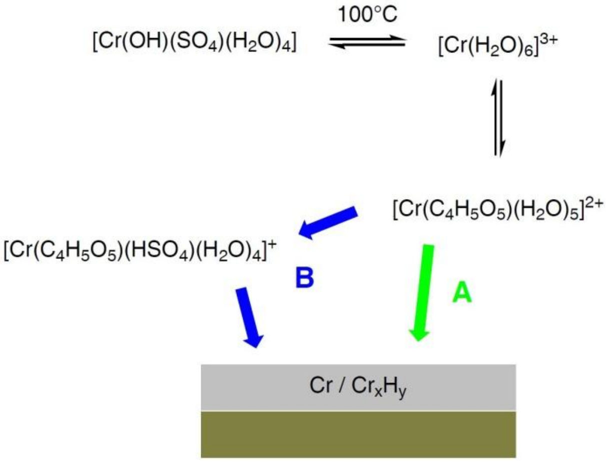
100°C
[Cr(OH)(SO$_4$)(H$_2$O)$_4$]
[Cr(H$_2$O)$_6$]$^{3+}$
[Cr(C$_4$H$_5$O$_5$)(H$_2$O)$_5$]$^{2+}$
[Cr(C$_4$H$_5$O$_5$)(HSO$_4$)(H$_2$O)$_4$]$^+$
B
A
Cr / Cr$_x$H$_y$

Figure 4.34 Illustration for proposed mechanism for chromium deposition from the new solution

In contrast to reaction route B, reaction route A does not include the possibility of re-addition of a sulfate or hydrogen sulfate ligand. This re-complexation cannot be ruled out, even if the direct reduction from the malate complex is more likely. In both cases, the reduction is conceivable via both a one-step mechanism, and/or a two-step mechanism, with a divalent chromium complex as an intermediate.

4.5 Use of other Complexing Agents

In order to further investigate the newly developed system, identical measurements were performed, with the substitution of malic acid with a weaker alternative, formic acid, and a stronger alternative, oxalic acid. While these systems were not as extensively studied as the malic acid system, the deposition results were sufficient to draw important conclusions.

4.5.1 Formic Acid

In order to investigate the action of formic acid as a complexing agent, the preparation was carried out identically, with the malic acid substituted by formic acid. Three identical measurements were carried out sequentially, at a current density of 5 A dm^{-2} for 5 minutes. The results are shown in Figure 4.35.

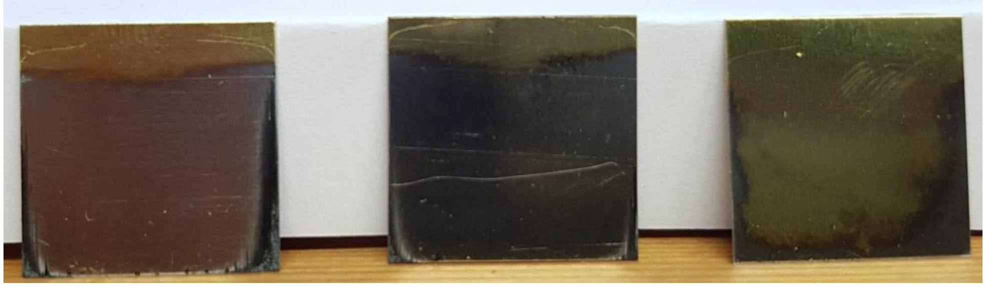

Figure 4.35 Photograph of three consecutive deposition trials (left to right) from a solution complexed with formic acid instead of malic acid

The photograph shows that the deposition very quickly deteriorates (left to right). By the third trial, almost no chromium was deposited. However, for the first measurement, the deposited film was very bright. Figure 4.36 shows an SEM image of the first sample (left).

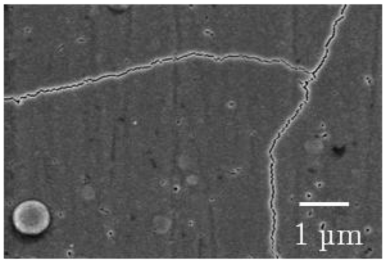

Figure 4.36 SEM image of a chromium deposit from a formic acid complexed solution

The SEM images shows a very smooth microstructure, which is in correlation with the very bright film. However, the quick deterioration means the complexing action of the formic acid is not strong enough to maintain a stable complex.

4.5.2 Oxalic Acid

Similarly, identical solutions were prepared with the malic acid being substituted by oxalic acid. Initially, measurements were also performed at a current density of 5 A dm^{-2} for 5 minutes. The samples are shown in Figure 4.37.

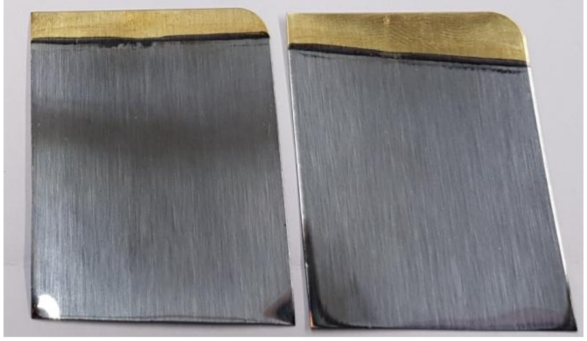

Figure 4.37 Photograph of two consecutive deposition measurements from a solution complexed with oxalic acid instead of malic acid

The results showed a very high reproducibility of the measurement, due to the stronger complexing action of the oxalic acid. In order to additionally probe the versatility of the oxalic acid system, measurements were also carried out at 4 and 6 A dm^{-2}. Figure 4.38 shows photographs, as well as SEM images of samples performed at 4, 5, and 6 A dm^{-2} for 5 minutes each.

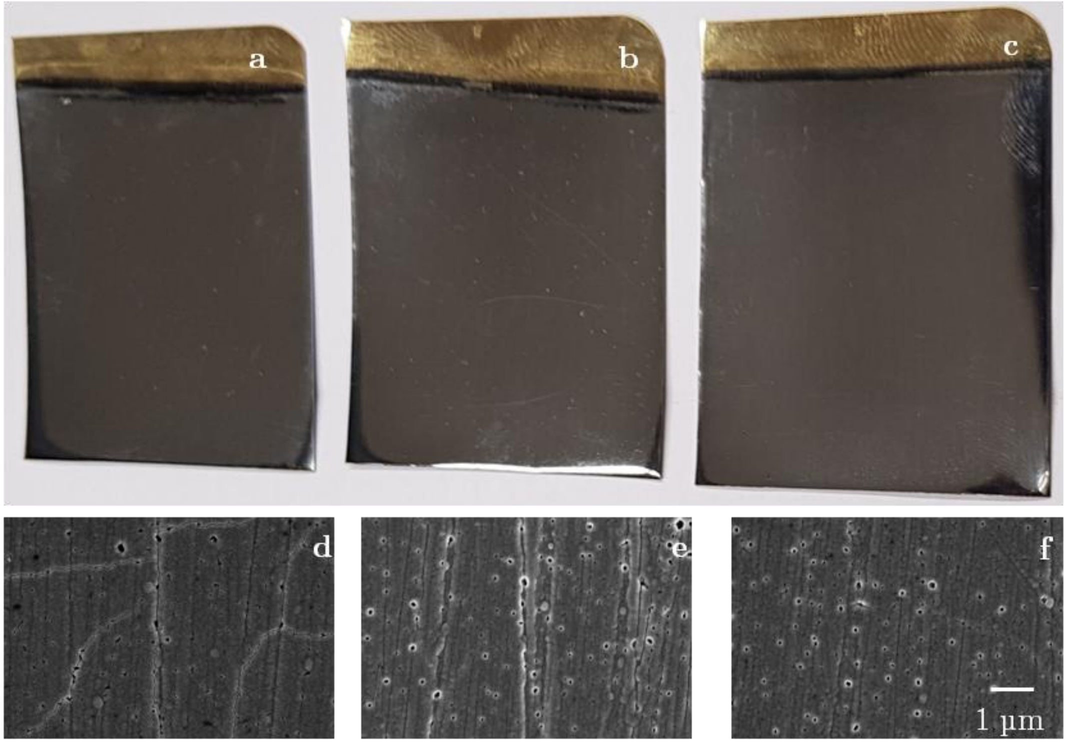

Figure 4.38 (a), (b), (c) Photographs of galvanostatically deposited chromium films on brass from an oxalic acid complexed solution for 5 minutes with cathodic current densities of 4, 5, and 6 A dm^{-2} respectively. (d), (e), (f) show the corresponding SEM images of each sample

While all the films seemed similar to the eye, however, the SEM images show that as the current density is increased, the surface irregularity also increases. On the other hand the film thickness was almost identical in all samples, which was roughly 0.25 µm. Thus, the next step was to investigate the effect of deposition time on film thickness. Using a current density of 4 A dm^{-2}, the deposition was carried out for 5 and 10 minutes. The corresponding photographs and SEM images are shown in Figure 4.39.

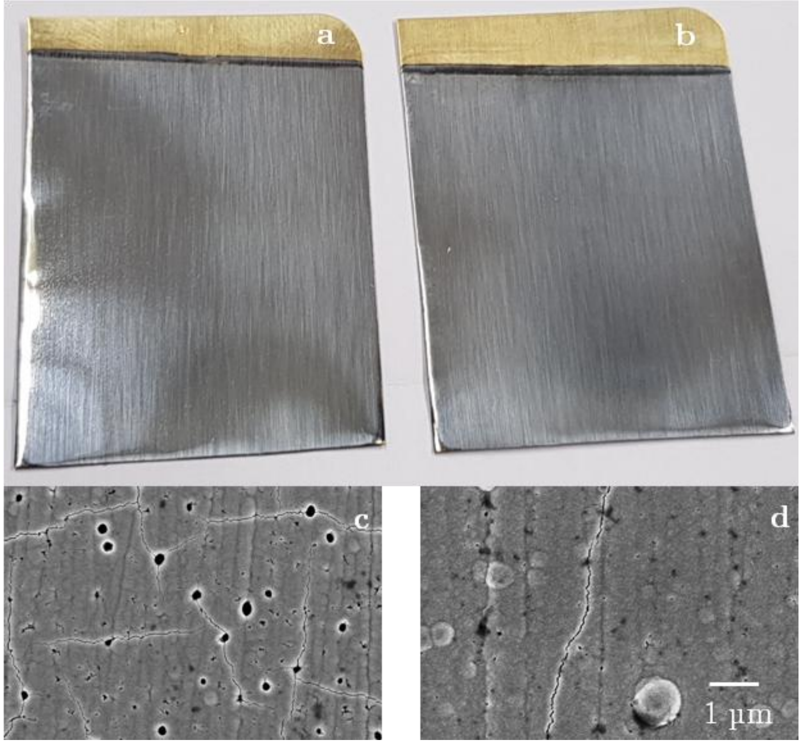

Figure 4.39 (a), (b) Photographs of galvanostatically deposited chromium films on brass from an oxalic acid complexed solution with $j = -4$ A dm^{-2} for 5 and 10 minutes, respectively. (c) and (d) show the corresponding SEM images for each sample

As the deposition time increases, it is clear that the film becomes more dense, with fewer pores and cracks. In addition, the thickness was doubled from about 0.25 µm to 0.5 µm. Moreover, the oxalic acid system showed a high resilience towards changes in pH. Measurements were conducted at pH values of up to 4 and gave identical deposits.

Hence, it can be clearly seen that the nature of the complexing agent itself plays a vital role in determining the quality of the deposit. Comparing all three complexing agents shows that the higher up the spectrochemical series, the more stable the complex is, and thus, the better the quality of the deposit.

5 Conclusions and Outlook

5.1 Conclusions of the Iridium Study

In this study, well-defined iridium nanospheres could be electrodeposited from aqueous solution onto glassy carbon electrodes, using a similar method to that found in literature for the electrodeposition of platinum nanospheres[12]. While, previous studies have reported the possibility of depositing aggregates of iridium onto platinum and glassy carbon[24], or the deposition of nano-porous structures of a few nanometers in size[69], there have been no reports on the electrodeposition of well-defined iridium structures.

The electrodeposition of Iridium from aqueous solutions presents the challenge of hydrogen evolution and subsequent bubble formation, which blocks the substrate surface and prevents deposition. This challenge was overcome by employing a very high overpotential for a few milliseconds, allowing for progressive nucleation on the active sites of the GC surface[66]. In addition, by varying different parameters, the size and loading of the iridium nanospheres could be varied. Moreover, cyclic voltammetry and SEM investigations were carried out to characterize the iridium nanostructures.

Finally, the electrocatalytic activity of the Iridium nanospheres towards CO adlayer oxidation was investigated, as a means of probing the particle surface. It was found that in terms of oxidation peak potential, particle size does not have a significant influence on the electrocatalytic activity. However, 100 and 200 nm particles showed a different CO oxidation profile, in contrast to the larger ones. This may be a result of some agglomeration, or the influence of size on surface structure, since smaller particles tend to be less uniform in structure than larger nanospheres.

The electrocatalytic activity could be enhanced by voltammetric treatment of the particles in 0.1 M H_2SO_4. The peak potential for the treated particles showed a shift to more negative values. This might be an effect of surface roughening due to potential cycling.

The next step would be the fabrication of preferentially oriented nanocrystals with well defined facets, similar to those produced from other noble metals, such as platinum and palladium[12,13]. While, many attempts have been carried out to electrodeposit other preferentially oriented nanocrystals of iridium, it was found that iridium behaves differently to platinum and palladium under such conditions, since it was not possible to obtain similar nanostructures.

Hence, a new method needs to be investigated to deposit preferentially oriented iridium nanocrystals with well defined facets. There is a wide range of parameters to be investigated, including electrolyte, concentration and pH effects, which all play an important role in determining the suitable conditions to obtain such nanocrystals.

Nevertheless, the iridium nanospheres themselves provide a basis for more research. For example, the iridium nanospheres can be used as cores, and other metals can be deposited on top of them and the electrocatalytic activity of such core-shell structures investigated. Thus, this study provides the framework for a large field of research on the nano-modification of carbon supported iridium electrodes and the use of iridium as an electrocatalyst in industrial applications. The modification of such nanostructures to get a high electrocatalytic activity with minimum loading can overcome economic barriers, and open many doors for new applications.

5.2 Conclusions of the Chromium Study

The aim of this study was to find a suitable substitute for Cr(VI) systems for chromium deposition, since these systems have proven to be hazardous to the environment as well as toxic for humans. The most promising alternative is a Cr(III) substitute, however trivalent chromium systems come with many challenges coupled with the constantly changing chemistry of the plating bath.

Thus, in order to develop a new system for chromium deposition, it was essential to understand the underlying similarities and differences between both systems, particularly in the initial stages of deposition. This was achieved by designing a fundamental study to investigate the time-dependant potentiodynamic growth of chromium on glassy carbon electrodes from simple baths of Cr(III) and Cr(VI).

The use of GC electrodes minimizes substrate interactions with the environment, as well as epitaxial effects, which may influence the deposition behavior. These advantages allow a deeper investigation of the deposition mechanism from both systems.

The results of the fundamental study showed that hexagonal chromium particles were successfully deposited onto the GC surface from both systems at pH 1. For a *bcc* metal, it would be highly unlikely that such hexagonal structures are pure chromium. Based on literature, it can be concluded that the deposits are *hcp* chromium hydride crystals. At room temperature and pressure, this serves to be the first reporting of stable hexagonal chromium hydride under these conditions.

SEM analysis of the deposited chromium revealed that at least for the first hour of deposition, both systems yield large, crystalline hexagonal chromium hydride crystals. With longer deposition times though, deposits from trivalent chromium tend to decompose into amorphous structures, unlike the deposits from hexavalent chromium, which maintain their hexagonal structural integrity, independent of deposition time.

This is likely due to the formation of long chain oligomers of the Cr^{3+} aquo complexes via olation reactions, which are catalyzed by the presence of Cr^{2+} species and higher pH values near the surface. These long chain oligomers cannot be easily reduced to chromium metal, and thus the concentration of active species decreases below the critical percentage for chromium hydride formation. However, this process is not present in the hexavalent system, due to the presence of a different Cr^{3+} intermediate, chromic dichromate, which does not take part in such olation reactions. Hence, the continuous supply of active species results in the stabilization of chromium hydride for up to 6 hours.

Therefore, the key to developing a reliable Cr(III) plating bath is to generate an active Cr(III) complex and to ensure that the bath chemistry remains unchanged. Since higher pH's promote olation, the simple solution was kept at pH 1. By monitoring the solution for a long time of about 4 weeks, it was evident that the solution color changes from green to blue, indicating a very slow ligand exchange process, until the solution consisted mainly of the monomeric aquo-complex, $[Cr(H_2O)_6]^{3+}$. Electrochemical measurements at pH 3 on GC revealed crystalline films, in contrast to amorphous deposits from green solutions, as well as lower HER currents, indicating a potentially more efficient process.

The acceleration of the ligand exchange process was investigated, and it was found that by heating the solution and further lowering of the pH, the blue solution could be obtained within a few hours. Upscaling to higher concentrations and investigating galvanostatic deposition resulted in the formation of hydroxides on the surface.

In order to prevent hydroxide formation, further complexation with an organic acid was required. Electrochemical measurements carried out on GC after complexation with malic acid revealed a superior film structure, with no evidence of hydroxides on the surface. In addition, the preparation of the solution was followed stepwise by UV-VIS spectroscopyto verify that the process parameters for the newly developed preparation technique, which include temperature, time and pH changes, are sufficient for successful ligand exchange and subsequent complexation with the organic acid.

While the deposition results on GC were impressive, the real test for the system would be the performance for plating metal surfaces. For these investigations, another important component, boric acid, was needed for deposition to take place. Boric acid is believed to be a buffer for plating baths, however its exact function is not fully understood to date, since its pKa value is much higher than that of the solution. A series of galvanostatic and galvanic pulsing measurements were used to investigate the electrodeposition on brass at different pH values, temperatures, current densities and deposition times. The results show successful plating on brass with film thicknesses varying from 100 nm to more than 3 µm.

Finally, the action of other complexing agents, formic acid and oxalic acid, as a substitute for malic acid was also investigated. From these measurements, it could be concluded that the type of organic acid used determines the quality of the deposit. Comparing all three complexing agents shows that the higher up the spectrochemical series, the more stable the complex is, and thus, the better the quality of the deposit.

Nevertheless, the scope of this research could be made wider. Fundamental investigations into the action of boric acid and the search for a substitute would be very important, since boric acid itself is considered a hazardous substance. The search for film enhancing additives, for different decorative as well as functional applications is another interesting aspect, to further tune this bath to fit different industrial applications.

5.3 Thesis Outlook

The recommendations for future work with respect to iridium and chromium deposition have been mentioned in the previous sections. In this section, the projection of the knowledge obtained from these studies onto other systems is briefly discussed.

Both of the systems under investigation presented unique challenges, for the well-established discipline of electrochemical metal deposition. These challenges could only be properly tackled by appropriate fundamental research. While nowadays the mainstream direction of research is more applied, however in some cases the best way to tackle the application related difficulties is by taking a few steps back and conducting basic, fundamental research to verify the underlying problems.

In this thesis, this was achieved by taking a closer look at the initial stages of both iridium and chromium deposition. By identifying the nucleation problem in iridium and the changing complex chemistry of chromium, it was then possible to find a suitable solution. This leads to the next important aspect; process development.

For successful innovation in a simple electrochemical technique like metal deposition, identifying and optimizing key stages in the related processes is paramount. This could be achieved by developing the electrochemical process itself, like in the iridium study, or by modifying the preparation technique of the electrolyte, to optimize its performance with a simple electrochemical process such as galvanostatic deposition, as in the case of the chromium study.

Finally, by combining both process optimization methodologies of electrochemical and electrolyte process development for the same system, systems that were once thought to be impossible can be investigated from a different perspective. With the aid of fundamental research, the different challenges can be separately investigated, and for each a suitable solution can be found.

Bibliography

[1] C. Raub, in *Met. Plat. Patination Cult. Tech. Hist. Dev.* (Eds.: S. La Niece, P.B.T.-M.P. and P. Craddock), Butterworth-Heinemann, **1993**, pp. 284–290.

[2] T. Reier, M. Oezaslan, P. Strasser, *ACS Catal.* **2012**, *2*, 1765–1772.

[3] L. A. Kibler, *Chemphyschem* **2006**, *7*, 985–991.

[4] J. K. Norskov, C. H. Christensen, *Science* **2006**, *312*, 1322–1323.

[5] V. R. Stamenkovic, B. Fowler, B. S. Mun, G. Wang, P. N. Ross, C. A. Lucas, N. M. Marković, *Science* **2007**, *315*, 493–497.

[6] K. Zhou, Y. Li, *Angew. Chem. Int. Ed. Engl.* **2012**, *51*, 602–613.

[7] P. Kaghazch, F. C. Simeone, K. A. Soliman, L. A. Kibler, T. Jacob, *Faraday Discuss.* **2009**, *140*, 9.

[8] K. A. Soliman, F. C. Simeone, L. A. Kibler, *Electrochem. commun.* **2009**, *11*, 31–33.

[9] K. A. Soliman, D. M. Kolb, L. A. Kibler, T. Jacob, *Beilstein J. Nanotechnol.* **2014**, *5*, 1349.

[10] I. Ermanoski, C. Kim, S. P. Kelty, T. E. Madey, *Surf. Sci.* **2005**, *596*, 89–97.

[11] T. Ming, W. Feng, Q. Tang, F. Wang, L. Sun, J. Wang, C. Yan, *J. Am. Chem. Soc.* **2009**, *131*, 16350–16351.

[12] N. Tian, Z.-Y. Zhou, S.-G. Sun, Y. Ding, Z. L. Wang, *Science (80-.).* **2007**, *316*, 732–735.

[13] N. Tian, Z.-Y. Zhou, N.-F. Yu, L.-Y. Wang, S.-G. Sun, *J. Am. Chem. Soc.* **2010**, *132*, 7580–7581.

[14] D. Pletcher, *Industrial Electrochemistry*, Chapman And Hall, London, **1982**.

[15] M. Paunovic, M. Schlesinger, *Fundamentals of Electrochemical Deposition*, John Wiley & Sons Inc., Pennington, NJ, **1998**.

[16] A. F. Holleman, E. Wiberg, N. Wiberg, *Lehrbuch Der Anorganischen Chemie*, Walter De Gruyter, Berlin, **2007**.

[17] V. S. Protsenko, F. I. Danilov, *Clean Technol. Environ. Policy* **2014**, *16*, 1201–1206.

[18] J. Guertin, J. A. Jacobs, C. P. Avakian, *Chromium(VI) Handbook*, CRC Press, Florida, **2001**.

[19] D. Golub, Y. Oren, *J. Appl. Electrochem.* **1989**, *19*, 311–316.

[20] M. Binneweis, M. Jäckel, H. Willner, G. Rayner-Canham, *Allgemeine Anorganische Chemie*, Spektrum Akademischer Verlag, Heidelberg, **2011**.

[21] Y. Yao, Q. Wei, M. Sun, Y. Chen, X. Ren, *RSC Adv.* **2013**, *3*, 13131.

[22] R. Giovanardi, G. Orlando, *Surf. Coatings Technol.* **2011**, *205*, 3947–3955.

[23] Z. Zeng, Y. Zhang, W. Zhao, J. Zhang, *Surf. Coatings Technol.* **2011**, *205*, 4771–4775.

[24] S. Le Vot, L. Roué, D. Bélanger, *Electrochim. Acta* **2012**, *59*, 49–56.

[25] E. Gileadi, *Physical Electrochemistry*, Wiley-VCH, **2011**.

[26] W. Plieth, *Electrochemistry for Materials Science*, Elsevier Science, **2008**.

[27] E. Budevski, G. Staikov, W. J. Lorenz, *Electrochemical Phase Formation and Growth*, Wiley-VCH, Weinheim, **1996**.

[28] M. Schlesinger, M. Paunovic, Eds. , *Modern Electroplating*, John Wiley & Sons Inc., Pennington, NJ, **2000**.

[29] M. Mühlbacher, High-Resolution Characterization of TiN Diffusion Barrier Layers, Linköping University, **2015**.

[30] A. D. McNaught, A. Wilkinson, *IUPAC. Compendium of Chemical Terminology, 2nd Ed. (the "Gold Book").*, Blackwell Scientific Publications, **1997**.

[31] T. Ohsaka, M. Isaka, K. Hirano, T. Ohishi, *Ultrason. Sonochem.* **2008**, *15*, 283–288.

[32] A. G. Muñoz, H. J. Lewerenz, *J. Electrochem. Soc.* **2009**, *156*, D184.

[33] W. E. Van der Linden, J. W. Dieker, *Anal. Chim. Acta* **1980**, *119*, 1–24.

[34] S. Chakraborty, Ed. , *Microfluidics and Microfabrication*, Springer Science+Business Media, LLC, New York, **2010**.

[35] Y. Sheasha, D. Yücel, L. A. Kibler, M. Knape, S. Holl, S. Henne, S. Heitmüller, T. Jacob, *ChemElectroChem* **2017**, *4*, 1390–1394.

[36] N.-F. Yu, N. Tian, Z.-Y. Zhou, L. Huang, J. Xiao, Y.-H. Wen, S.-G. Sun, *Angew. Chem. Int. Ed. Engl.* **2014**, *53*, 5097–101.

[37] Y. Garsany, O. A. Baturina, K. E. Swider-lyons, S. S. Kocha, *Anal. Chem.* **2010**, *82*, 6321–6328.

[38] Y. Sheasha, K. A. Soliman, S.-G. Sun, T. Jacob, L. A. Kibler, *Electrocatalysis* **2015**, *6*, 365–372.

[39] J. Wang, L. D. Hutchins, *Anal. Chim. Acta* **1985**, *167*, 325–334.

[40] G. N. Kamau, *Anal. Chim. Acta* **1988**, *207*, 1–16.

[41] I. Hu, D. H. Karweik, T. Kuwana, *J. Electroanal. Chem.* **1985**, *188*, 59–72.

[42] A. a. Isse, S. Gottardello, C. Maccato, A. Gennaro, *Electrochem. commun.* **2006**, *8*, 1707–1712.

[43] F. Maillard, M. Eikerling, O. V. Cherstiouk, S. Schreier, E. Savinova, U. Stimming, *Faraday Discuss.* **2004**, *125*, 357–377.

[44] X. Yang-tao, D. Yu-jie, Z. Wei, X. Tian-dong, *Surf. Coatings Technol.* **2017**, *330*, 170–177.

[45] G. Trejo, H. Ruiz, R. O. Borges, Y. Meas, *J. Appl. Electrochem.* **2001**, *31*, 685–692.

[46] E. Riedel, *Allgemeine Und Anorganische Chemie*, Walter De Gruyter, Berlin, **1982**.

[47] C. E. Mortimer, U. Müller, *Chemie*, Georg Thieme Verlag, Stuttgart, **2007**.

[48] R. E. Dickerson, H. B. Gray, G. P. Haight Jr., *Chemical Principles*, The Benjamin / Cummings Publishing Company, Inc, Menlo Park, **1979**.

[49] E. Wiberg, N. Wiberg, *Inorganic Chemistry*, Academic Press, **2001**.

[50] S. Ghaziof, K. Raeissi, M. A. Golozar, *Surf. Coatings Technol.* **2010**, *205*, 2174–2183.

[51] Jens Bohnet, Entwicklung Eines Verfahrens Zur Abscheidung Technischer Chromschichten Aus Einem Chrom(Ⅲ)-Elektrolyt ３, **2009**.

[52] N. N. Greenwood, A. Earnshaw, *Chemie Der Elemente*, VCH Verlagsgesellschaft, Weinheim, **1988**.

[53] L. Rao, Z. Zhang, J. I. Friese, B. Ritherdon, S. B. Clark, N. J. Hess, D. Rai, *J. Chem. Soc. Dalt. Trans.* **2002**, 267.

[54] H. Stunzi, L. Spiccia, F. P. Rotzinger, W. Martyt, *Inorg. Chem.* **1989**, *28*, 66–71.

[55] J. P. Hoare, *J. Electrochem. Soc.* **1979**, *126*, 190–199.

[56] Y. B. Song, D. T. Chin, *Electrochim. Acta* **2002**, *48*, 349–356.

[57] V. Protsenko, F. Danilov, *Electrochim. Acta* **2009**, *54*, 5666–5672.

[58] N. Van Phuong, S. C. Kwon, J. Y. Lee, J. Shin, B. T. Huy, Y. I. Lee, *Microchem. J.* **2011**, *99*, 7–14.

[59] D. R. Lide, *CRC Handbook of Chemistry and Physics*, CRC Press, Boca Raton, FL, **2005**.

[60] M. A. S. Rodrigues, R. F. Dalla Costa, A. M. Bernardes, J. Zoppas Ferreira, *Electrochim. Acta* **2001**, *47*, 753–758.

[61] J.-Y. Lee, M. Kim, S.-C. Kwon, *Trans. Nonferrous Met. Soc. China* **2009**, *19*, 819–823.

[62] L. Simanavičius, A. Stakenas, A. Šarkis, *Electrochim. Acta* **1997**, *42*, 1581–1586.

[63] E. Michailova, I. Vitanova, D. Stoychev, A. Milchev, *Electrochim. Acta* **1993**, *38*, 2455–2458.

[64] D. N. Buckley, L. D. Burke, *J. Chem. Soc. Faraday Trans. 1* **1975**, *72*, 2431–2444.

[65] P. Panagiotopoulou, D. I. Kondarides, *Catal. Today* **2006**, *112*, 49–52.

[66] M. Ueda, H. Dietz, A. Anders, H. Kneppe, A. Meixner, W. Plieth, *Electrochim. Acta* **2003**, *48*, 2539.

[67] E. L. MacNamara, *J. Electrochem. Soc.* **1962**, *109*, 61–63.

[68] L. Vázquez-Gómez, S. Cattarin, R. Gerbasi, P. Guerriero, M. Musiani, *J. Appl. Electrochem.* **2009**, *39*, 2165–2172.

[69] E. N. El Sawy, V. I. Birss, *J. Mater. Chem.* **2009**, *19*, 8244.

[70] C. P. De Pauli, S. Trasatti, *J. Electroanal. Chem.* **2002**, *538–539*, 145–151.

[71] S. Trasatti, *Electrochim. Acta* **1984**, *29*, 1503–1512.

[72] F. . Mattos-Costa, P. de Lima-Neto, S. a. . Machado, L. . Avaca, *Electrochim. Acta* **1998**, *44*, 1515–1523.

[73] G. García, M. T. M. Koper, *Chemphyschem* **2011**, *12*, 2064–72.

[74] D. A. J. Rand, R. Woods, *Electroanal. Chem. Interfacial Electrochem.* **1974**, *55*, 375–381.

[75] P. W. Atkins, J. de Paula, *Physical Chemistry*, Wiley-VCH Verlag, Weinheim, **2013**.

[76] G. Wedler, *Lehrbuch Der Physikalischen Chemie*, Wiley-VCH Verlag, Weinheim, **2004**.

[77] J. I. Goldstein, D. E. Newbury, P. Echlin, D. C. Joy, C. E. Lyman, E. Lifshin, L. Sawyer, J. R. Michael, *Scanning Electron Microscopy and X-Ray Microanalysis*, Springer US, **2003**.

[78] Y. Leng, *Materials Characterization: Introduction to Microscopic and Spectroscopic Methods*, Wiley-VCH Verlag, Weinheim, **2013**.

[79] G. Dehm, *In-Situ Electron Microscopy : Applications in Physics, Chemistry and Materials Science*, Wiley-VCH Verlag, Weinheim, **2012**.

[80] O. Brümmer, *Handbuch Festkörperanalyse Mit Elektronen, Ionen Und Röntgenstrahlung*, Friedr. Vieweg & Sohn, Braunschweig, Wiesbaden, **1980**.

[81] A. Weidner, H. Biermann, *Moderne Methoden Der Rasterelektronenmikroskopie*, Wiley-VCH Verlag, Weinheim, **2014**.

[82] R. O. Müller, *Spektrochemische Analysen Mit Röntgenfluoreszenz : Theorie Und Industrielle Anwendung*, R. Oldenbourg, München, **1967**.

[83] K. Nygård, K. Hämäläinen, S. Manninen, P. Jalas, J.-P. Ruottinen, **2004**, 354–359.

[84] G. Kortüm, *Kolorimetrie Und Spektralphotometrie*, Springer Verlag Berlin Heidelberg, **1942**.

[85] E. G. Vinokurov, **2010**, *83*, 258–262.

[86] C. A. Snavely, *J. Electrochem. Soc.* **1947**, *92*, 537–577.

[87] W. A. Wood, *London, Edinburgh, Dublin Philos. Mag. J. Sci.* **1937**, *24*, 772–776.

[88] A. J. Bradley, E. F. Ollard, *Nature* **1926**, *117*, 122.

[89] L. Wright, H. Hirst, J. Riley, *Trans. Faraday Soc.* **1935**, *31*, 1253–1259.

[90] U. von Meyenburg, O. Siroky, G. Schwarzenbach, *Helv. Chim. Acta* **1973**, *56*, 1099–1114.

[91] J. E. Finholt, M. E. Thompson, R. E. Connick, *Inorg. Chem.* **1981**, *20*, 4151–4155.

[92] M. Thompson, R. E. Connick, *Inorg. Chem.* **1981**, *20*, 2279–2285.

[93] H. Stünzi, W. Marty, *Inorg. Chem.* **1983**, *22*, 2145–2150.

[94] L. Spiccia, *Polyhedron* **1991**, *10*, 1865–1872.

[95] F. I. Danilov, V. S. Protsenko, V. O. Gordiienko, A. S. Baskevich, V. V.

Artemchuk, *Prot. Met. Phys. Chem. Surfaces* **2013**, *49*, 299–303.
[96] Z. Zeng, Y. Sun, J. Zhang, *Electrochem. commun.* **2009**, *11*, 331–334.
[97] J. Ketelaar, *Chesmische Konstitution*, Springer Fachmedien, Wiesbaden, **1964**.
[98] P. Kurzweil, P. Scheipers, *Chemie - Grundlagen, Aufbauwissen, Anwendungen Und Experimente*, Vieweg + Teubner, Wiesbaden, **2010**.

List of Figures

Figure 2.1 Gibbs free energy of nucleation as a function of particle size............................ 6
Figure 2.2 Nucleation and Growth modes[29] 8
Figure 2.3 Structural model of glassy carbon[34] 8
Figure 2.4 Schematic of iridium deposition on glassy carbon[24] 9
Figure 2.5 (a) Current—potential curves for the potentiodynamic deposition of chromium hydride crystals on GC showing the increase in HER current as deposition time increases (b) SEM image of the deposited chromium hydride on GC 10
Figure 2.6 Geometric structures of complexes based on their respective coordination numbers[48] 11
Figure 2.7 Ligand field splitting of d-orbitals[49] 12
Figure 2.8: Dependence of degree of oligomerization on pH in a 0.05 M Cr (III) solution. Symbols: monomer (●), dimer (◆), trimer (▲), unseparated higher oligomers (■)[53]......... 15
Figure 2.9 SEM image of an iridium aggregate on glassy carbon[24].................................. 20
Figure 2.10 Energy diagram for a system with (red) and without (black) a catalyst, adopted from[30]... 21
Figure 2.11 Comparison between the activities of bulk (dashed) Pt, Ru, and Ir and their nanoparticles (solid) for the OER[2] 22
Figure 3.1: Schematic of the SWP profile used for electrodeposition of Ir nanospheres.... 26
Figure 3.2: Schematic of the galvanic pulsing technique used for Cr deposition.............. 27
Figure 3.3: Typical cyclic voltammogram of an activated GC electrode in 0.1 M H_2SO_4 at 50 mV s^{-1} 32
Figure 4.1 (a) Current–potential curve of the Ir nanoparticles, deposited on a GC electrode via the double-step technique, in 0.1 M H_2SO_4 at 50 mV s^{-1}, (b) SEM image of the deposit. Adapted by permission from Springer Customer Service Centre GmbH: Springer US, Electrocatalysis, Electrochemical Fabrication of Well-Defined Spherical Iridium Nanoparticles and Electrocatalytic Activity towards Carbon Monoxide Adlayer Oxidation by Sheasha et al. © Springer Science + Business Media New York 2015......... 38
Figure 4.2 Influence of E_n on particle size and density. Reprinted by permission from Springer Customer Service Centre GmbH: Springer US, Electrocatalysis, Electrochemical Fabrication of Well-Defined Spherical Iridium Nanoparticles and Electrocatalytic Activity towards Carbon Monoxide Adlayer Oxidation by Sheasha et al. © Springer Science + Business Media New York 2015 39
Figure 4.3 (a) Current–potential curves of the Ir nanoparticles, deposited on a GC electrode via the SWP technique at different values of E_n, in 0.1 M H_2SO_4 at 50 mV s^{-1}, (b) Particle size and density as a function of E_n. Adapted by permission from Springer

Customer Service Centre GmbH: Springer US, Electrocatalysis, Electrochemical Fabrication of Well-Defined Spherical Iridium Nanoparticles and Electrocatalytic Activity towards Carbon Monoxide Adlayer Oxidation by Sheasha et al. © Springer Science + Business Media New York 2015 40

Figure 4.4 (a) Current–potential curves of the Ir nanoparticles, deposited on a GC electrode via the SWP technique for 1 hour (red) and 2 hours (black), in 0.1 M H_2SO_4 at 50 mV s^{-1}, (b), (c) SEM images of the particles deposited for 1 hour and 2 hours, respectively. Adapted by permission from Springer Customer Service Centre GmbH: Springer US, Electrocatalysis, Electrochemical Fabrication of Well-Defined Spherical Iridium Nanoparticles and Electrocatalytic Activity towards Carbon Monoxide Adlayer Oxidation by Sheasha et al. © Springer Science + Business Media New York 2015......... 41

Figure 4.5[42] (a) Current–potential curves for carbon monoxide adlayer oxidation on Ir particles with different sizes deposited on GC, in 0.1 M H_2SO_4 at 10 mV s^{-1}, (b), (c), (d), (e) SEM images of Ir nanospheres with average diameters of 100 nm, 200 nm, 290 nm, and 370 nm, respectively. Adapted by permission from Springer Customer Service Centre GmbH: Springer US, Electrocatalysis, Electrochemical Fabrication of Well-Defined Spherical Iridium Nanoparticles and Electrocatalytic Activity towards Carbon Monoxide Adlayer Oxidation by Sheasha et al. © Springer Science + Business Media New York 2015 42

Figure 4.6[42] (a) Current–potential curves for carbon monoxide adlayer oxidation on Ir particles with an average diameter of 370 nm but different surface morphologies deposited on GC, in 0.1 M H_2SO_4 at 10 mV s^{-1}, (b), (c) SEM images of rough and as prepared particles, respectively. Adapted by permission from Springer Customer Service Centre GmbH: Springer US, Electrocatalysis, Electrochemical Fabrication of Well-Defined Spherical Iridium Nanoparticles and Electrocatalytic Activity towards Carbon Monoxide Adlayer Oxidation by Sheasha et al. © Springer Science + Business Media New York 2015 43

Figure 4.7 Current–potential curves of a massive chromium electrode in 0.1 M H_2SO_4 at 50 mV s^{-1} 44

Figure 4.8[35] (a) Window opening measurement showing bulk oxidation and/or dissolution of a massive chromium electrode 0.1 M H_2SO_4 at 50 mV s^{-1}, (b) surface oxidation region. Adapted by permission from John Wiley & Sons, Inc.: WILEY-VCH, ChemElectroChem, Potentiodynamic Chromium Deposition from Trivalent and Hexavalent Systems on Glassy Carbon Electrodes: Initial Stages and Mechanistic Insights by Sheasha et al. © 2017 Wiley-VCH Verlag GmbH & Co. KGaA, Weinheim........ 45

Figure 4.9 (a) SEM image of polished Cr electrode, (b), (c) SEM images of oxidised chromium surface. Adapted by permission from John Wiley & Sons, Inc.: WILEY-VCH, ChemElectroChem, Potentiodynamic Chromium Deposition from Trivalent and

Hexavalent Systems on Glassy Carbon Electrodes: Initial Stages and Mechanistic Insights by Sheasha et al. © 2017 Wiley-VCH Verlag GmbH & Co. KGaA, Weinheim................. 46

Figure 4.10 Current–potential curves for the potentiodynamic deposition of chromium hydride crystals from (a) trivalent and (b) hexavalent solutions on GC for 1 hour at 50 mV s^{-1} (c), (d) SEM images of the deposited particles from Cr^{3+} and Cr^{6+} solutions, respectively. Adapted by permission from John Wiley & Sons, Inc.: WILEY-VCH, ChemElectroChem, Potentiodynamic Chromium Deposition from Trivalent and Hexavalent Systems on Glassy Carbon Electrodes: Initial Stages and Mechanistic Insights by Sheasha et al. © 2017 Wiley-VCH Verlag GmbH & Co. KGaA, Weinheim................. 47

Figure 4.11 Effect of scan rate on potentiodynamic deposition of chromium from a Cr(III) solution on GC. Adapted by permission from John Wiley & Sons, Inc.: WILEY-VCH, ChemElectroChem, Potentiodynamic Chromium Deposition from Trivalent and Hexavalent Systems on Glassy Carbon Electrodes: Initial Stages and Mechanistic Insights by Sheasha et al. © 2017 Wiley-VCH Verlag GmbH & Co. KGaA, Weinheim................. 48

Figure 4.12 SEM images revealing different particle structures on GC after deposition times of (a) 1, (c) 3, (e) 4, and (g) 6 hours from Cr(III) solutions, while (b), (d), (f), (h) represent those changes for the same deposition durations from Cr(VI) solutions. Adapted by permission from John Wiley & Sons, Inc.: WILEY-VCH, ChemElectroChem, Potentiodynamic Chromium Deposition from Trivalent and Hexavalent Systems on Glassy Carbon Electrodes: Initial Stages and Mechanistic Insights by Sheasha et al. © 2017 Wiley-VCH Verlag GmbH & Co. KGaA, Weinheim.. 49

Figure 4.13 Illustrations of proposed mechanisms for chromium hydride deposition from (a) Cr(III) solutions and (b) Cr(VI) solutions. Adapted by permission from John Wiley & Sons, Inc.: WILEY-VCH, ChemElectroChem, Potentiodynamic Chromium Deposition from Trivalent and Hexavalent Systems on Glassy Carbon Electrodes: Initial Stages and Mechanistic Insights by Sheasha et al. © 2017 Wiley-VCH Verlag GmbH & Co. KGaA, Weinheim 50

Figure 4.14 (a) Current–potential curves for the potentiodynamic deposition of chromium on GC from a fresh solution (green) and an aged solution (blue) (b) and (c) represent SEM images of the deposits respectively... 52

Figure 4.15 (a) Current–time curves for the potentiostatic deposition of chromium on GC from a fresh solution (green) and an aged solution (blue) (b) and (c) represent SEM images of the deposits respectively... 53

Figure 4.16 SEM images of galvanostatically deposited chromium on GC from (a) a fresh Cr(III) solution, (b) an aged Cr(III) solution (c) a fresh Cr(III) solution complexed with malic acid 54

Figure 4.17 Schematic of process required to prepare the new solution 55

Figure 4.18 UV-VIS absorption spectra of basic chromium sulfate dissolved in water (black) and sulfuric acid (green) 56
Figure 4.19 (a) Time dependant UV-VIS absorption spectra of the first preparation step (b)change in peak positions during heating as a function of time 57
Figure 4.20 (a) Differences in UV-VIS absorption spectra before and after the first preparation step for sulfuric acid and perchloric acid as solvents (b) Peak shifts for both systems 58
Figure 4.21 UV-VIS absorption spectra for the remaining preparation steps in (a) sulfuric acid and (b) perchloric acid 59
Figure 4.22 Changes in UV-VIS absorption peaks for (a) sulfuric acid system and (b) perchloric acid system 61
Figure 4.23 SEM images of galvanostatically deposited chromium on GC from the new solution at $j = 2.5$ A dm^{-2} for (a) 30 minutes and (b) 1 hour 63
Figure 4.24 SEM images of chromium deposited by galvanic pulsing on GC from (a), (b) non-complexed chromium solution with pulse durations of 0.5 s and 0.05 s, respectively (c), (d) new chromium solution with pulse durations of 0.5 s and 0.05 s, respectively 63
Figure 4.25 SEM images of chromium deposited on G using galvanic pulsing using (a) $I_L = -5$ A dm^{-2} and (b) $I_L = -10$ A dm^{-2} 64
Figure 4.26 SEM images of Hull Cell sample highlighting the microstructure in different current density regions 65
Figure 4.27 (a), (b) SEM images and galvanic pulsing deposition diagram of chromium deposited on brass at $I_L = -10$ A dm^{-2} and $I_L = -10$ A dm^{-2}, respectively (c) SEM image of galvanostatically deposited chromium on brass at $j = -10$ A dm^{-2} for 10 minutes...... 65
Figure 4.28 Photographs of chromium films deposited on brass sheets with an area of (a), (b), (c)4 cm^2 and (d) 16 cm^2 66
Figure 4.29 SEM images and galvanic pulsing diagrams for chromium deposited on brass for a total pulsing duration of (a) 10 minutes (b) 20 minutes and (c) 30 minutes........... 67
Figure 4.30 Difference in optical appearance between identically deposited chromium films on (a) unpolished and (b) polished brass sheets 67
Figure 4.31 SEM images of galvanostatically deposited chromium films on brass for 5 minutes with $j = -10$ A dm^{-2} at temperatures of (a) 20 °C, (b) 30 °C, (c) 40 °C, and (d) 50 °C 68
Figure 4.32 SEM images highlighting microstructural differences between (a) galvanostatic deposition and (b) pulse plating of chromium on brass 69
Figure 4.33 (a) Effect of deposition temperature on thickness and (b) relationship between duration and thickness for galvanostatic deposition (red) and galvanic pulse plating (blue) 69

Figure 4.34 Illustration for proposed mechanism for chromium deposition from the new solution 72
Figure 4.35 Photograph of three consecutive deposition trials (left to right) from a solution complexed with formic acid instead of malic acid 73
Figure 4.36 SEM image of a chromium deposit from a formic acid complexed solution ... 73
Figure 4.37 Photograph of two consecutive deposition measurements from a solution complexed with oxalic acid instead of malic acid 73
Figure 4.38 (a), (b), (c) Photographs of galvanostatically deposited chromium films on brass from an oxalic acid complexed solution for 5 minutes with cathodic current densities of 4, 5, and 6 A dm^{-2} respectively. (d), (e), (f) show the corresponding SEM images of each sample 74
Figure 4.39 (a), (b) Photographs of galvanostatically deposited chromium films on brass from an oxalic acid complexed solution with $j = -4$ A dm^{-2} for 5 and 10 minutes, respectively. (c) and (d) show the corresponding SEM images for each sample 75

List of Tables

Table 3.1: Stepwise preparation of the glassy carbon surface 31
Table 3.2: Stepwise preparation technique of the newly developed Cr (III) plating solution 33
Table 3.3: Details of the chemicals used 33
Table 3.4: Details of the materials used.. 34
Table 4.1 Summary of preparation stages and details of each stage 61

Nomenclature

HER	Hydrogen Evolution Reaction
OER	Oxygen Evolution Reaction
SWP	Square Wave Potential
THH	Tetrahexahedral
GC	Glassy Carbon
UV-VIS	Ultraviolet-Visible Light
OPD	Over Potential Deposition
UPD	Under Potential Deposition
EASA	Electrochemical Active Surface Area
CV	Cyclic Voltammetry/Voltammogram
WE	Working Electrode
CE	Counter Electrode
RE	Reference Electrode
SCE	Standard Calomel Electrode
MMO	Mixed Metal Oxide
SEM	Scanning Electron Microscope
EDX	Energy Dispersive X-ray
UHV	Ultra-High Vacuum
XRF	X-ray Fluorescence
SD	Standard Deviation
bcc	Base Centered Cubic
hcp	Hexagonal Close Packed

Acknowledgements

First and foremost, I would like to express my gratitude to Allah (*Subhanahu wa Ta'ala*) for the countless blessings He has bestowed upon me, without which I would have not been able to succeed in any of my endeavors.

Next, I would like to thank Prof. Dr. Timo Jacob for giving me the opportunity to carry out my doctorate at the Institute of Electrochemistry. From the start of my stay here as a master's thesis student, he has placed a lot of trust in my abilities, especially since I had no prior experience in electrochemistry. For that, I will always be grateful. Moreover, a very special thanks goes to Dr. Ludwig Kibler who also dedicated a lot of time and effort to helping me every step of the way on technical, scientific and personal levels.

I would also like to thank Prof. Dr. Carsten Streb for being my second reviewer, with all the extra effort associated with this role.

To all the members of the Institute of Electrochemistry who are still here, and those who left, I would like to say thank you for the enjoyable atmosphere. I hope that we cross paths again and wish you good luck for your plans.

Thank you to Dr. Michael Zöllinger, Dr. Stefan Henne, Mr. Sebastian Holl, Ms. Miriam Knappe and Dr. Sebastian Heitmüller of Dr.-Ing Max Schlötter GmbH & Co KG for the fruitful and scientifically exciting cooperation.

Most importantly, I thank my parents for their continuous help and support ever since I was a child. Their constant guidance and motivation have made me what I am today. Without them, I would not have come this far. I would also like to thank my brothers for their support throughout my journey to obtain this degree. To Areej, my wife, best friend, and colleague, I thank you for enabling me to reach my goals by providing all kinds of help, support and assistance at work and outside.

As expats, the friends we make abroad are almost like family, and in some cases even more. Hence, I would like to thank all of the friends that I made here, who have made my stay abroad feel like home.

Last but not least, to those few friends from back home who have kept in touch all those years, regardless of the distance, thank you for making the journey easier.

Curriculum Vitae

Yasser Samir Abdelmoaty Mostafa Sheasha

Born on Monday, 30/04/1990 in Giza, Egypt

Academic Background

10/2014 – 11/2018 Dr. rer. nat in Chemistry from the Faculty of Natural Sciences, Ulm University

- PhD student at the Institute of Electrochemistry under the supervision of Prof. Dr. Timo Jacob
- Electrochemical metal deposition group leader as of 01/2018

08/2012 – 06/2014 MSc. in Materials Engineering from the Faculty of Engineering and Materials Science, The German University in Cairo (GUC)

- Master thesis: "Electrodeposition of Well Defined Iridium Nanostructures" at the Institute of Electrochemistry, Ulm University
- Teaching assistant from 08/2012 to 08/2013 at the GUC

10/2007 – 07/2012 BSc. in Engineering and Materials Science from the Faculty of Engineering and Materials Science, The German University in Cairo (GUC)

- Bachelor thesis: "Exchange Bias Effect between Ferromagnetic Nanoparticles and Anti-Ferromagnetic Thin Films" at the Institute of Micro and Nanomaterials, Ulm University
- Graduated with Honours

06/2005 – 06/2007 International General Certificate of Secondary Education (IGCSE) and A Levels at Manarat Alriyadh International School

- British high school certificates from Cambridge and London

09/1997 – 06/2004 Elementary and Middle School education at Manarat Alriyadh International School

List of Publications

Journal article:	Y. Sheasha, D. Yücel, L. A. Kibler, M. Knape, S. Holl, S. Henne, S. Heitmüller, T. Jacob, Potentiodynamic Chromium Deposition from Trivalent and Hexavalent Systems on Glassy Carbon Electrodes: Initial Stages and Mechanistic Insights, *ChemElectroChem* **2017**, *4*, 1390–1394.
Journal article:	Y. Sheasha, K. A. Soliman, SG. Sun, L. A. Kibler, T. Jacob, Electrochemical Fabrication of Well-Defined Spherical Iridium Nanoparticles and Electrocatalytic Activity towards Carbon Monoxide Adlayer Oxidation, *Electrocatalysis* **2015**, *6*, 365–372.
Conference Poster:	Y. Sheasha, K. A. Soliman, L. A. Kibler, T. Jacob, Electrodeposition of Iridium Nanospheres on Glassy Carbon, *1st Gerischer-Kolb Symposium*, October 15-17 **2014**, Berlin, Germany.